

Dartmouth College

Dartmouth Digital Commons

Dartmouth College Ph.D Dissertations

Theses and Dissertations

Spring 4-20-2023

New Physics in the Age of Precision Cosmology

Vivian I. Sabla

Dartmouth College, vivian.i.sabla.gr@dartmouth.edu

Follow this and additional works at: <https://digitalcommons.dartmouth.edu/dissertations>



Part of the [Cosmology, Relativity, and Gravity Commons](#), and the [Elementary Particles and Fields and String Theory Commons](#)

Recommended Citation

Sabla, Vivian I., "New Physics in the Age of Precision Cosmology" (2023). *Dartmouth College Ph.D Dissertations*. 206.

<https://digitalcommons.dartmouth.edu/dissertations/206>

This Thesis (Ph.D.) is brought to you for free and open access by the Theses and Dissertations at Dartmouth Digital Commons. It has been accepted for inclusion in Dartmouth College Ph.D Dissertations by an authorized administrator of Dartmouth Digital Commons. For more information, please contact dartmouthdigitalcommons@groups.dartmouth.edu.

NEW PHYSICS IN THE AGE OF PRECISION COSMOLOGY

A Thesis

Submitted to the Faculty

in partial fulfillment of the requirements for the

degree of

Doctor of Philosophy

in

Physics and Astronomy

by

Vivian I. Sabla

DARTMOUTH COLLEGE

Hanover, New Hampshire

April 20, 2023

Examining Committee:

Robert Caldwell, Chair

Marcelo Gleiser

Devin Walker

Tristan Smith

F. Jon Kull, Ph.D.

Dean of the Guarini School of Graduate and Advanced Studies

Abstract

The Λ -cold dark matter (Λ CDM) model has become the standard model of cosmology because of its ability to reproduce a vast array of cosmological observations, from the earliest moments of our Universe, to the current period of accelerated expansion, which it does with great accuracy. However, the success of this model only distracts from its inherent flaws and ambiguities. Λ CDM is purely phenomenological, providing no physical explanation for the nature of dark matter, responsible for the formation and evolution of large-scale structure, and giving an inconclusive explanation for dark energy, which drives the current period of accelerated expansion.

Furthermore, cracks in its observational grounding have begun to form. When Λ CDM is used to interpret recent high precision measurements, tensions appear between individual experiments: the inferred values of the current cosmic expansion rate H_0 and the amplitude of cosmic density fluctuations S_8 based on early universe measurements of the cosmic microwave background (CMB), are in disagreement with the values measured in the local universe, probed by supernovae, weak lensing, and galaxy surveys. These tensions, if not caused by unaccounted for systematics, suggest that the model we use to interpret early universe data may be incomplete.

This thesis collects works investigating alternative cosmologies and new analysis techniques which aim to explain these tensions and ambiguities in Λ CDM, and provide new probes of beyond the standard model physics. I present four main projects here: I developed an assisted quintessence model of early dark energy (EDE), linking the early

and late epochs of cosmic acceleration, which provides a solution to the H_0 tension and coincidence problem of dark energy; I investigated the role that microphysics plays on the EDE solution to the Hubble tension, and found that EDE with an anisotropic shear can solve both the Hubble and S_8 tensions simultaneously; I developed a method of using line-intensity mapping to constrain beyond the standard model physics, which I used to forecast constraints on non- Λ CDM models and non-Gaussianity; and I derived the cosmological perturbations and initial conditions for a dark energy model built from a three classical $U(1)$ gauge fields coupled to a scalar field, which I will use to investigate the compatibility of a such a scenario with cosmological observations.

Acknowledgments

The past six years have been some of the best and hardest of my life, and I owe many incredible people thanks for the encouragement and support that has brought me to the finish line.

First and foremost, I would like to thank all my committee members. Thank you to Marcelo Gleiser for first sparking my interest in Dartmouth cosmology, and always being incredibly encouraging and supportive. Thank you to Devin Walker for always having useful insights and for getting me through two monster courses: GR and QFT. Thank you to Tristan Smith for the many interesting conversations, comments, and useful tips over the years, and more generally for writing your papers on EDE, which got me interested in the topic in the first place! Last, but certainly not the least, I would like to thank my advisor Robert Caldwell for his extraordinary guidance and support throughout my time at Dartmouth. Robert has been a phenomenal advisor providing important insights and ideas when I was stuck on research projects and allowing me the freedom to explore curiosities and projects which I found interesting. His ability to cut through the details and re-establish the crux of any problem is something I hope to one day master, along with the amazing ability to hold paper titles and authors from 30 years ago at the tip of the tongue. Thank you for inserting sarcasm, endless fun, and jokes into tedious work along the way, and always stopping by the office to distract us with panda and hippo cams. And, thank you for telling me to go outside and see the sun when I obsessively redid calculations over and over

again. Your levelheadedness is unmatched, and something to strive for.

I want to send a huge shoutout to Terry Kovacs for his incredible help with all things computer oriented. Without his ingenious three-week-long installation of CosmoMC back in 2019, none of my research would have been possible. Cheers to being the first person in the department to get that dang code working smoothly! Thank you for continuously keeping bigbang running, despite my overuse.

Members of my cohort - Riley Chien, Vinny Flynn, Shujie Gu, Linta Joseph, Avery Tishue, Sara Vannah, Kelly Whalen, Ethan Williams, Jun Yang, and of course, Danny Sanchez. You have all made the transition to Dartmouth and the first few years of grad school so enjoyable, from baseball in the first year office to all the fun times outside. Special and ultimate thanks to my Office 305 homies, Avery, Kelly, and Riley (in the summer), the ducks, the palm trees, the salt lamp, the diffuser, the happy spoons, and the beads - may the hype forever be with us all.

To the Wilder community at large, especially the grad students, both old and new - thank you for making this department such a vibrant and supportive place to be in. Special thanks to our fantastic admins Judy Lowell, Meg Whitlock, and Tressy Manning for all they do behind the scenes.

Lastly, but very importantly, to my family who have seen me through it all, always guiding and aiding me when necessary, constantly inspiring me and encouraging me to pursue my own path, I owe you my deepest gratitude. In particular, thank you to my parents for all their guidance, sacrifices, and unconditional love - your belief in me has been a source of strength and motivation, and I cannot imagine having accomplished this without you. To my chosen family - Phil, Sam, Nicki, Kate, Savannah, Jackson, Corrie, Ben, Erszie, Sally, Lana, Mauli, and Caitlyn - thanks for all the fun times and emotional support to get me through this wild ride.

Contents

Abstract	ii
Acknowledgments	iv
1 Introduction	1
2 Assisted Quintessence as Early Dark Energy	6
2.1 Assisted Quintessence Cosmology	7
2.1.1 Background Dynamics	8
2.1.2 Resolving the Hubble Tension	11
2.1.3 Linear Perturbations	13
2.2 Data and Methodology	18
2.3 Observational Constraints	19
2.3.1 Fixed Model Parameters	19
2.3.2 Full Results	22
2.4 Discussion and Conclusions	24
Appendices	30
2.A Numerical Implementation	30
2.B Extended Results for Fixed Model Parameters	32
2.C Extended Results for Free Model Parameters	34

3	Microphysics of Early Dark Energy	39
3.1	Phenomenological Fluid Model (PFM)	41
3.1.1	Background dynamics	42
3.1.2	Perturbative microphysics	44
3.2	Data and Methodology	50
3.3	Results	52
3.3.1	Resolution to the Hubble tension	52
3.3.2	Varying the sound speed	56
3.3.3	Shear model I	63
3.3.4	Shear model II	66
3.3.5	Future constraints	77
3.4	Discussion	79
	Appendices	84
3.A	Shear Model Derivation	84
3.A.1	Shear model I	84
3.A.2	Shear model II	85
3.B	Extended Results	87
4	Joint LIM power spectrum and VID constraints on BSM cosmologies	98
4.1	LIM Observables	102
4.1.1	Power Spectrum	103
4.1.2	Voxel Intensity Distribution	104
4.1.3	Noise & Survey Specifications	105
4.1.4	Variance & Covariance	108
4.2	Line Emission Model	109

4.3	Cosmological Models	111
4.3.1	Phenomenological non-cold dark matter	111
4.3.2	Axionic Dark Matter	114
4.3.3	Non-Gaussianity	118
4.4	IM Forecasting	120
4.4.1	Experiment	121
4.4.2	Fisher Matrix Forecasts	121
4.4.3	Phenomenological non-CDM	122
4.4.4	Axion Dark Matter	124
4.4.5	Non-Gaussianity	126
4.5	Discussion	127
5	Cosmological Perturbation Theory with a Coupled Scalar-U(1) Model of Dark Energy	132
5.1	Background Model	132
5.2	Scalar Perturbations	138
5.2.1	Gauge Transformations	142
5.3	Initial Conditions	146
5.3.1	Initial Conditions in Pure Radiation Domination	151
5.3.2	Correcting for the Presence of Matter	153
5.4	Future Work	155
6	Summary and Future Directions	156
	References	160

Chapter 1

Introduction

The past 25 years have been a golden age for cosmology, with many experiments providing unprecedented insight into the building blocks of the Universe. The discovery of the accelerated expansion of the Universe [2, 3] drastically altered our view of the cosmic energy budget, and led to the establishment of a standard cosmological model. It is now understood that only 5% of the Universe is made of known particles, while 25% is composed of an unknown form of gravitationally interacting matter known as “dark matter”. The dominant remaining 70% is made of “dark energy,” the even more mysterious unknown piece responsible for the accelerated expansion.

The Λ -cold dark matter (Λ CDM) model, named for its dark sector components, parameterizes dark matter as a cold, or non-relativistic, and collisionless fluid, and dark energy as a cosmological constant Λ . Λ CDM has become the standard model of cosmology because of its ability to accurately reproduce a vast range of observations, from the cosmic microwave background (CMB) [4], to large-scale structure (LSS) [5, 6], to the expansion history of the Universe [7]. However, the success of this model only distracts from its inherent flaws. It offers no explanation of the physical nature of its dark sector components, making it a phenomenological model, not a comprehensive theory. Furthermore, when it is used to interpret recent high

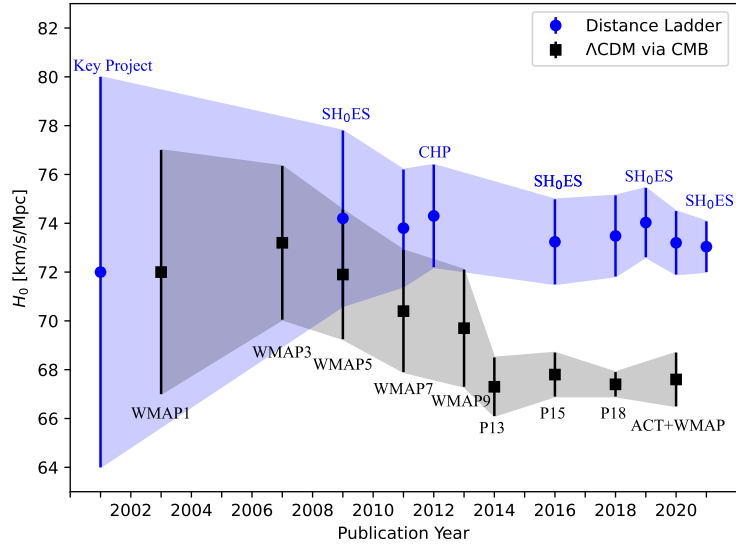


Figure 1.1: Evolution of the Hubble tension in the last 20 years using direct measurements from the distance ladder (in blue) and CMB-based measurements assuming Λ CDM (in black). Adapted from [1].

precision measurements, discrepancies appear between individual experiments: the inferred values of the current cosmic expansion rate H_0 , and the amplitude of cosmic density fluctuations S_8 , based on early universe measurements of the CMB, are in disagreement with the values measured in the local universe, probed by supernovae, weak lensing and galaxy surveys. These parameter mismatches have become known as the Hubble or H_0 tension, and the S_8 tension, respectively.

The Hubble constant tension is a disagreement that has been growing for years, increasing as both early- and late- universe measurements yield ever more precise results, as shown in Fig. 1.1. Today, this tension is seen mostly clearly between the SH0ES collaboration measurement of $H_0 = 73.04 \pm 1.04$ km/s/Mpc [8], and the Planck inference of $H_0 = 67.4 \pm 0.5$ km/s/Mpc [4], showing a greater than 5σ discrepancy. Similarly for S_8 , the inference from the *Planck* mission gives $S_8 = 0.832 \pm 0.013$, in 3σ tension with the most recent Dark Energy Survey measurement of $S_8 = 0.776 \pm 0.017$ [6]. However, it is yet to be understood whether the S_8

tension is real or due to systematic [9], or non-linear modelling [10] effects in late-time measurements. The key to understanding the root of these tensions comes with how these different measurements are taken. Late-universe measurements rely on the direct measurement of distance to astrophysical objects, and the distribution of galaxies and galaxy clusters to measure H_0 and S_8 , respectively. On the other hand, early-universe inferences of these parameters rely on fitting a cosmological model, usually chosen to be Λ CDM, to the power spectrum of fluctuations in the CMB radiation, making them model-dependent estimates. The tension between these two types of measurements seem to be unexplained by unknown systematics in any experiment [11–14], therefore suggesting that the model we use to interpret early-universe data is incomplete.

While the Hubble and S_8 tensions show cracks in standard model around the time of recombination, other inconsistencies and ambiguities exist in both the very early and late universe. Λ CDM itself offers no explanation for how the initial conditions of the Universe it requires came to be. An early period of inflationary expansion prior to the Hot Big Bang, is the most accepted paradigm for explaining the quantum fluctuations that seed the observed large-scale structure and CMB anisotropies, however the specific model which gives rise to such an epoch is weakly constrained by current cosmological data, leaving a large ambiguity in cosmological theory.

At the opposite end of cosmic history, the standard models predictions at small (sub-galactic) scales are in disagreement with observations [15], particularly, too much dark matter is predicted in the inner-most regions of galaxies, giving rise to what is known as the “cusp-core” problem [16]. One possible solution is to go beyond the standard CDM description and look at alternative DM scenarios which introduce a small-scale suppression of gravitational clustering. Furthermore, while we know dark energy is currently driving a period of accelerated cosmic expansion, the entire

catalog of cosmological data cannot yet distinguish the underlying physics responsible for dark energy.

The many attempts to resolve the Hubble tension fall in two broad categories: late-universe solutions which alter local-universe determinations of H_0 , and early-universe solutions which change pre-recombination physics to alter the CMB inference of H_0 (see [17, 18] and references therein). Early dark energy (EDE) models have emerged as one of the most promising classes of early universe solutions to the H_0 tension, and generally consist of adding a scalar field that temporarily adds dark energy, equal to about 10% of the total cosmological energy density, in between matter-radiation equality and recombination (for a review see Ref. [19]). This briefly boosts the expansion rate in the early universe, raising the CMB determination of the Hubble constant. By introducing this new component at this time in cosmic evolution, you can add a relatively low-density component and still have enough of an impact to fix the Hubble tension, without spoiling the exquisite fit to CMB data that comes in Λ CDM. Scalar fields arise naturally in high-energy physics as the driving force behind inflation, and possibly the current period of accelerated expansion. If the timeline of our Universe begins and ends with scalar field driven acceleration, you must appreciate the possibility of it existing in the intermediate epochs.

However, it is an open question if the simple scenarios of early dark energy that have been considered thus far serve as suitable cosmological models. The dynamics of the canonical scalar fields used in these models appear to preclude a fully satisfactory solution. *Planck* data does not favor EDE as a cosmological model on its own. It is only through the inclusion of a late-universe prior on H_0 that preference for EDE is found in non-negligible amounts. This is avoided in analyses which use alternative CMB datasets, yet more work needs to be done to see if these differing constraints are due to experimental systematics [20–22]. More importantly, while EDE models offer

a good solution to the Hubble tension within CMB data, the CMB-preferred value of S_8 is increased in these models, exacerbating the S_8 tension. As such, when standard EDE models are confronted with current LSS data, they are strongly disfavored, potentially precluding EDE as a viable cosmological model [23–28].

This thesis collects works investigating alternative cosmologies that aim to explain these tensions and ambiguities in the standard Λ CDM model and its so-far proposed extensions, as well as novel techniques which can probe beyond the standard model (BSM) physics in a new way. In Chapter 2, I test an assisted quintessence (AQ) model of early dark energy (EDE) as a potential solution to both the Hubble tension, and coincidence problems of both early and late dark energy. Chapter 3 explores what types of perturbative evolution is necessary to strengthen and improve on current solutions to the Hubble tension. In Chapter 4, I forecast the ability of future line-intensity mapping experiments to constrain non-cold dark matter models and local-type non-Gaussianity. And finally in Chapter 5, I derive the cosmological linear perturbations and initial conditions which describe the full evolution of a dark energy model built from a trio of classical U(1) gauge fields, which I plan to use to investigate the compatibility of this scenario with cosmological observations.

Chapter 2

Assisted Quintessence as Early Dark Energy

*With minor changes, this chapter is adapted from Sabla, V.I. & Caldwell, R.R. “No H_0 assistance from assisted quintessence.” *Phys. Rev. D* **103**, 103506. *arXiv*: 2103.04999 (2021).*

Early Dark Energy (EDE), while one of the most promising possible solutions to the Hubble tension, appears fine tuned. Why should dark energy, or a related dark-sector field, emerge near matter-radiation equality at a trace amplitude – just enough to shift the length scales imprinted into the CMB – before falling dormant? Not only that, dark energy itself appears fine tuned – why should it come to dominate so late in the history of the Universe? Surprisingly, both of these issues are addressed in an assisted quintessence scenario [29].

In assisted quintessence (AQ), multiple scaling fields are present. None of the fields alone is sufficient to drive cosmic acceleration. But as time progresses, more and more such fields thaw from the Hubble friction and activate, becoming dynamical. Due to the scaling behavior, the fields evolve as a tiny but constant fraction of the

background energy density. Eventually, the cumulative effect of the scaling fields is enough to catalyze cosmic acceleration. In this context, given a spectrum of scaling fields, early dark energy and dark energy are inevitable: EDE is just the thaw and activation of a scaling field; dark energy is the cumulative effect of a series of EDE fields.

In this work we assume the true value of H_0 is the one implied by the SH0ES measurement of $H_0 = 74.03 \pm 1.42$ km/s/Mpc [30], and we explore the ability of an individual AQ field to bring the CMB-derived value into concordance. We show that, at the background level, this new component of the energy density seems to be the balm needed to relieve the tension. However, the scaling behavior of the AQ field leaves a significant imprint on the inhomogeneities, ultimately spoiling the concordance and, in fact, exacerbating the tension.

This chapter is organized as follows. In Sec. 2.1 we introduce the AQ-EDE model as a potential solution to the Hubble tension. We describe the background solution as well as the behavior of linear perturbations. We present the cosmological data used in the MCMC analysis of the model in Sec. 2.2. Results of our parameter estimation, in particular H_0 , are given in Sec. 2.3. We conclude our discussion in Sec. 2.4 with our main findings. Appendices provide details of the numerical implementation of the model, and extended data analysis results.

Section 2.1

Assisted Quintessence Cosmology

The proposed scenario consists of the standard cosmological model, with dark energy in the form of assisted quintessence. The action is

$$S = \int d^4x \sqrt{g} \left(\frac{1}{2} M_P^2 R + \mathcal{L}_M - \sum_i \left[\frac{1}{2} (\partial \phi_i)^2 + V_i(\phi_i) \right] \right), \quad (2.1)$$

where \mathcal{L}_M represents the Standard Model plus cold dark matter, and the index i sums over the contributions of the AQ scaling fields. In the following, we describe the background dynamics, the proposed solution to the Hubble tension, and the behavior of linear perturbations used to evaluate the imprint of the AQ-EDE model on the CMB and the inferred Hubble constant.

2.1.1. Background Dynamics

Tracking fields, proposed as a way to circumvent the cosmic coincidence problem [31], have an attractor-like solution leading to a common evolutionary track. For dark-energy tracking solutions, the equation of state w_ϕ is a constant, less than or equal to the equation of state of the background fluid w_B . Scaling is a special case of tracking where the scaling fields have the same equation of state as the background, $w_\phi = w_B$. For an individual field with potential $V(\phi)$, the capacity for scaling or tracking behavior depends on the quantity [31]

$$\Gamma = \frac{V_{,\phi\phi}V}{(V_{,\phi})^2} \quad (2.2)$$

where $V_{,\phi} = \partial V / \partial \phi$. For convergence to a tracking solution, Γ must be nearly constant, in which case the equation of state is

$$w_\phi \approx \frac{w_B - 2(\Gamma - 1)}{1 + 2(\Gamma - 1)}. \quad (2.3)$$

Scaling requires $\Gamma \approx 1$, which implicates an exponential potential.

Exponential potentials arise naturally in higher-dimensional particle physics theories including Kaluza-Klein and string theories, and a variety of super-gravity models. In cosmology, they have mainly been studied within the context of inflation and for a possible role in late-time cosmology. See Refs. [32–40] and references therein.

We consider a sequence of exponential potentials of the form

$$V_i(\phi_i) = \mu_i^4 e^{-\beta_i \phi_i}. \quad (2.4)$$

For a single AQ field with this potential, the resulting field evolution,

$$\ddot{\phi} + 3H\dot{\phi} + V_{,\phi} = 0, \quad (2.5)$$

has a well-known exact solution in a background with equation of state w_B [32],

$$\beta\phi(t) = \ln \left(\frac{1}{2} \frac{1 + w_B}{1 - w_B} \beta^2 \mu^4 t^2 \right). \quad (2.6)$$

This scaling solution yields an energy density that is a constant fraction of the dominant background

$$\Omega_\phi(t) = 3(1 + w_B)/\beta^2. \quad (2.7)$$

The parameter β controls the energy density and is analogous to f_{EDE} of Ref. [41]. For self-consistency of solution, $\beta^2 > 1/3(1 + w_B)$ is required. When β is too low, the potential is sufficiently flat that the scalar field will inflate rather than scale.

The evolution of a single field in the exponential potential proceeds as follows. We consider the field to be initially frozen by the Hubble friction at $\dot{\phi} = 0$, in which case the equation of state is $w_\phi \approx -1$. The field begins to thaw and activate at a time determined by the parameter μ which is analogous to the z_c of Ref. [41]. The larger the value of μ , the earlier it thaws. As the field evolves toward the attractor solution, the equation of state scales according to the dominant background component. In Fig. 2.1 we plot the evolution of w_ϕ as a function of scale factor for a field that becomes dynamical right around matter-radiation equality. As the field thaws, the equation of state jumps upwards to match the dominant component, initially overshooting its

2.1 ASSISTED QUINTESSENCE COSMOLOGY

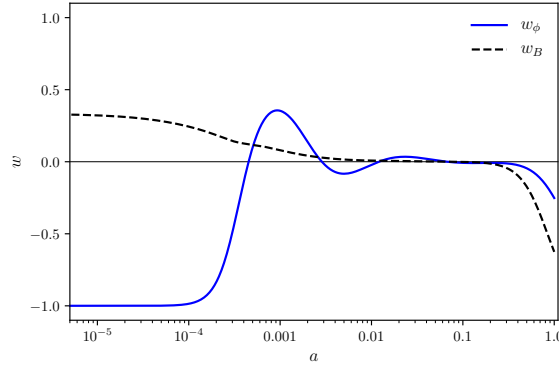


Figure 2.1: The evolution of the equation of state of the AQ field, w_ϕ (blue, solid), as a function of scale factor for a model with $\beta = 12$ and $\mu = 3.5 \text{ Mpc}^{-1/2}$. There is a downturn near $a \sim 0.4$ due to the onset of dark energy domination. For comparison, the background equation of state is shown (black, dashed).

mark, before it settles to the matter-dominant evolutionary track.

The addition of multiple scaling fields in the AQ scenario changes the system dynamics [29]. A succession of fields thaw and activate, each at a time determined by μ_i . All active fields contribute to the energy density, each satisfying $\beta_i^2 \gg 1/3(1+w_B)$. However, the ensemble is characterized by an effective β ,

$$\frac{1}{\beta_{\text{eff}}^2} = \sum_i \frac{1}{\beta_i^2}. \quad (2.8)$$

As fields are successively thawed, β_{eff} is lowered, thereby raising the collective energy density. This continues until the bound on β_{eff}^2 is saturated, when the fields “flatten the potential” and inflate. At late times, the equation of state asymptotes to

$$w_\phi = -1 + \frac{1}{3}\beta_{\text{eff}}^2, \quad (2.9)$$

approaching this limit from below [29].

Without the scaling behavior, the energy densities of the individual fields would be too small to ever dominate and acceleration would never arise. In this way, AQ

provides an ideal framework for EDE and dark energy. The necessary succession of thawing and scaling fields makes an early component plausible, and eventual cosmic acceleration inevitable.

There are many different ways to configure early and late dark energy components using N fields, each introducing two parameters. In order to address the Hubble tension, we will consider a single early component that activates near matter-radiation equality. For simplicity, we will consider the remaining AQ fields to sufficiently resemble a component with $w_\phi \approx -1$ so that we may safely replace them with a cosmological constant.

2.1.2. Resolving the Hubble Tension

Early universe solutions to the Hubble tension are grounded in the theoretical description of the CMB. One of the best constrained features of the CMB anisotropy pattern is the angular size of the first acoustic peak, modeled as $\theta_s = r_s(z_*)/D_A(z_*)$. Here, $r_s(z_*)$ is the comoving sound horizon at decoupling, and $D_A(z_*)$ is the comoving angular diameter distance to the surface of last scattering,

$$r_s(z_*) = \int_{z_*}^{\infty} \frac{c_s dz'}{H(z')}, \quad (2.10)$$

$$D_A(z) = \int_0^{z_*} \frac{dz'}{H(z')}, \quad (2.11)$$

where c_s is the sound speed. The sound horizon is dependent on pre-recombination energy densities and roughly scales with the Hubble parameter as $H_0^{-1/2}$, whereas $D_A(z_*)$ depends on densities after decoupling and scales as H_0^{-1} . This implies that if we decrease the sound horizon by adding new components to the energy density, and assuming the sound speed is unchanged, then we can increase the Hubble constant deduced from the CMB acoustic scale. As suggested in Ref. [42], we focus on the brief window between matter-radiation equality and recombination as this is when

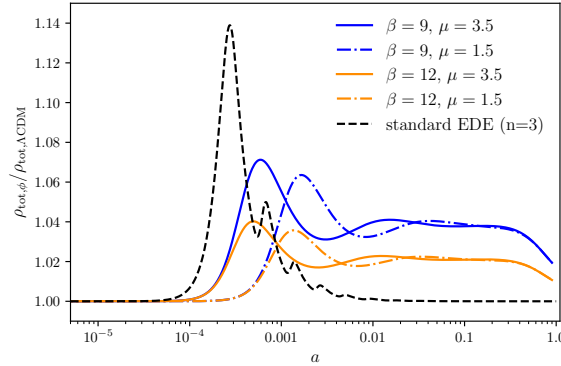


Figure 2.2: The evolution of the fraction of the total energy density in the AQ model to the Λ CDM model as a function of scale factor. For higher β and higher μ , the contribution of the AQ field to the energy budget decreases and peaks earlier, respectively. Note that μ has units of $\text{Mpc}^{-1/2}$. The black-dashed line shows the best-fit $n=3$ oscillating scalar field model of EDE from Ref. [43] for comparison.

the majority of the sound horizon accrues. By adding a small amount of EDE, it is possible to adequately lower the sound horizon, thereby increasing the Hubble constant inferred from the CMB.

An AQ field that activates during the epoch between equality and recombination, like the ones illustrated by the solid curves in Fig. 2.2, can produce enough of a spike in the total energy density to lower the sound horizon and raise the CMB inference of H_0 into agreement with local universe measurements. For example, based on Eqs. (2.10-2.11), a model with $\beta = 12$ and $\mu = 3.5 \text{ Mpc}^{-1/2}$ and otherwise standard parameters should result in $H_0 \simeq 73 \text{ km/s/Mpc}$. The use of a tracker potential has the added benefit of not demanding strict initial conditions, requiring only a two parameter extension to Λ CDM as opposed to the three parameter extensions required of other EDE models [41, 43–48]. The overshoot in the equation of state helps sharpen the spike in energy, and afterwards the AQ field remains present at a trace level due to the matter-era scaling solution.

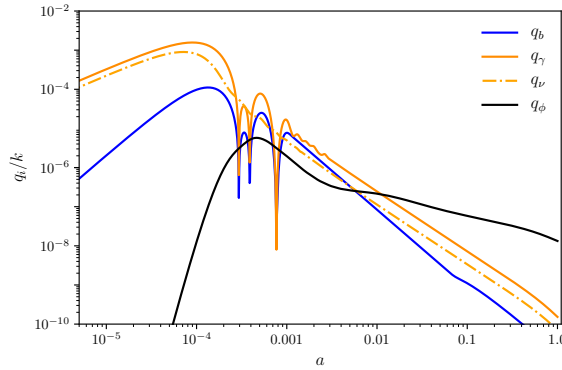


Figure 2.3: The evolution of the heat flux of all relevant components as a function of scale factor for the $k = 0.1 \text{ Mpc}^{-1}$ wave mode. These curves are generated by a model with the best-fit parameter values taken from the “semi-background” AQ model run with θ_ϕ allowed to evolve. The scaling behavior of the AQ field leads to the dominant contribution over the standard components, at $z \lesssim 100$ in the case shown.

2.1.3. Linear Perturbations

We have shown that at the background level an AQ field can resolve the Hubble tension. However, the viability of this scenario hinges on the behavior of the linear perturbations. For a single AQ field, the linear field perturbation $\delta\phi$ evolves according to the equation of motion

$$\delta\phi'' + 2\mathcal{H}\delta\phi' + (k^2 + a^2 V_{,\phi\phi})\delta\phi = -\frac{h'}{2}\phi', \quad (2.12)$$

where $\mathcal{H} = a'/a$, the primes indicate the derivative with respect to conformal time $\iota = \partial/\partial\tau$, h is the synchronous gauge metric potential (see [49]), and we work in Fourier space. The system is equivalent to a damped, driven, harmonic oscillator. The homogeneous solution is negligible: any initial conditions set by inflation or other early universe processes have long been lost or erased as a consequence of the frozen field with $w_\phi \approx -1$ [50, 51]. Once the field begins to thaw, the inhomogeneous solution begins to take form, with an effective frequency of oscillation $\omega_{\text{eff}} = \sqrt{k^2 + a^2 V_{,\phi\phi}}$.

To analyze the driving term, we focus on a field that thaws from the Hubble

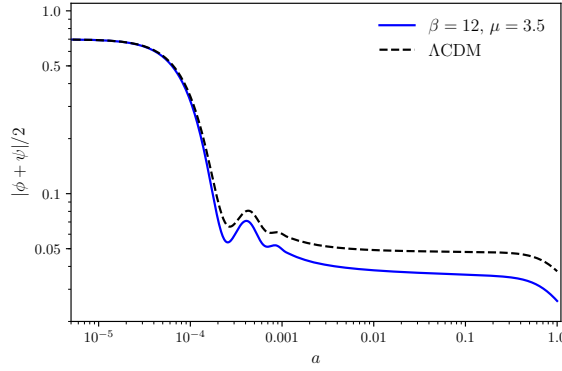


Figure 2.4: Evolution of the Weyl gravitational potential as a function of scale factor for the $k = 0.1 \text{ Mpc}^{-1}$ wave mode. The solid blue curve shows the gravitational potential for a model with the best-fit parameters taken from the “semi-background” AQ model run with θ_ϕ allowed to evolve. The best-fit ΛCDM model is shown by the black-dashed line. Due to the large heat flux of the scalar field, the gravitational potentials are shallower than in the ΛCDM model.

friction at or around matter-radiation equality so that the relevant evolution occurs in a matter-dominated background with $a \propto \tau^2$. We start from the well-known result that the CDM density contrast evolves in proportion to the scale factor, $\delta_c \propto a$, and that $h' = -2\delta'_c$ [49]. From this, we infer that $h' \propto a' \propto \tau$. Next, according to the scaling solution in Eq. (2.6), $\phi' = a\dot{\phi} \propto \tau^2/t$. Since conformal and cosmic time are related via $t \propto \tau^3$, we obtain $\phi' \propto \tau^{-1}$. Hence, the product $h'\phi'$ is independent of time. The driving term in Eq. (2.12) is constant as a result of the scaling solution for ϕ .

There are two regimes of response to the constant driving term: for $\omega_{\text{eff}} \lesssim \mathcal{H}$, $\delta\phi$ grows in proportion to the scale factor; for $\omega_{\text{eff}} \gtrsim \mathcal{H}$, the perturbation solution is simply

$$\delta\phi = -\frac{h'\phi'}{2(k^2 + a^2 V_{,\phi\phi})}. \quad (2.13)$$

This solution divides into two cases. For the brief interval when $\omega_{\text{eff}} \gtrsim \mathcal{H}$ and $k^2 \ll a^2 V_{,\phi\phi}$, the scaling solution again dictates that $\delta\phi \propto a$, whereas at smaller scales, for $k^2 \gg a^2 V_{,\phi\phi}$, $\delta\phi$ is a constant. Hence, we have a simple story for the evolution of the

AQ field perturbation: after an initial transient, $\delta\phi$ grows in proportion to the scale factor until the comoving mass scale drops below the wave number, $k^2 \gg a^2 V_{,\phi\phi}$, after which $\delta\phi$ is a constant. We note that if the AQ field decayed more rapidly than the background, then $\delta\phi$ would also decay.

We can use the results of this simple analysis to forecast the behavior of the AQ field perturbations in terms of fluid variables. The most significant role is played by the heat flux $q_\phi = 8\pi G a^2 (\rho_\phi + p_\phi) \theta_\phi$, where θ_ϕ is the velocity divergence of the AQ field. The heat flux obeys the equation

$$q'_\phi + 2\mathcal{H}q_\phi = 8\pi G a^2 k^2 \delta p_\phi, \quad (2.14)$$

where δp_ϕ is the pressure perturbation. The heat flux is related to our AQ field via θ_ϕ through

$$(\rho_\phi + p_\phi) \theta_\phi = \frac{k^2}{a^2} \phi' \delta\phi. \quad (2.15)$$

Again, we can use the scaling solution $\phi' \propto a^{-1/2}$ and $\delta\phi \propto a$, in which case the heat flux grows $\propto a^{1/2}$, until the comoving mass scale drops below the wave number. Thereafter q_ϕ decays $\propto a^{-1/2}$. This is significant, because all other contributions due to CDM, baryons, photons, neutrinos are zero (CDM) or decay more rapidly, and will eventually grow subdominant to the scalar field contribution. An example based on our numerical calculations is shown in Fig. 2.3. Despite contributing to the energy budget at a percent level, the AQ field has an outsize effect.

On the same scales, the AQ density perturbation $\delta\rho_\phi$ loses energy, decaying at the same rate as the background so that $\delta_\phi = \delta\rho_\phi/\rho_\phi$ is constant. Moreover, the pressure perturbation is $\delta p_\phi \approx -\delta\rho_\phi$, like a tension. Hence, the fluctuation response of the scalar field inhibits clustering.

The AQ contribution to the heat flux sources the trace-free scalar metric pertur-

bation, η [49]. In more physical terms, it causes the post-recombination gravitational potentials to decay, resulting in an additional integrated Sachs-Wolfe effect, an example of which is shown in Fig. 2.4. Due to the timing of this behavior, it primarily affects modes that determine the shape of the CMB anisotropy pattern at degree scales and larger. But there are more facets to the ultimate impact on the predicted CMB temperature and polarization anisotropy pattern, which we turn to next.

Parameter	Λ CDM	$\beta = 12, \mu = 3.5$	$\beta = 12, \mu = 3.5, \theta_\phi = 0$
$100\omega_b$	$2.235 (2.237) \pm 0.015$	$2.182 (2.186) \pm 0.014$	$2.068 (2.070) \pm 0.016$
ω_c	$0.1202 (0.1199) \pm 0.0013$	$0.1297 (0.1294) \pm 0.0013$	$0.1052 (0.1055) \pm 0.0014$
$100\theta_s$	$1.04089 (1.04105) \pm 0.00032$	$1.04017 (1.04011) \pm 0.00031$	$1.04220 (1.04212) \pm 0.00033$
τ	$0.0553 (0.0551) \pm 0.0076$	$0.0594 (0.0596)^{+0.0071}_{-0.0084}$	$0.113 (0.106)^{+0.015}_{-0.022}$
$\ln(10^{10}A_s)$	$3.046 (3.045) \pm 0.015$	$3.069 (3.070)^{+0.014}_{-0.016}$	$3.121 (3.106)^{+0.029}_{-0.040}$
n_s	$0.9645 (0.9644) \pm 0.0043$	$0.9574 (0.9581) \pm 0.0041$	$1.0010 (0.9994) \pm 0.0053$
β	-	12 (fixed)	12 (fixed)
$\mu [\text{Mpc}^{-1/2}]$	-	3.5 (fixed)	3.5 (fixed)
$H_0 [\text{km/s/Mpc}]$	$67.27 (67.45) \pm 0.56$	$64.20 (64.29) \pm 0.55$	$73.12 (72.98) \pm 0.77$
S_8	$0.834 (0.829) \pm 0.013$	$0.858 (0.856) \pm 0.013$	$0.726 (0.723) \pm 0.013$
Total χ^2_{\min}	1014.09	1048.38	1307.81

Table 2.1: The mean (best-fit) $\pm 1\sigma$ error of the cosmological parameters for Λ CDM, the AQ model with $\beta = 12, \mu = 3.5 \text{ Mpc}^{-1/2}$ and the “semi-background” model with $\theta_\phi = 0$. Constraints are based on the full *Planck* 2018 dataset.

Section 2.2

Data and Methodology

We run a complete Markov Chain Monte Carlo (MCMC) using the public code `CosmoMC`¹ [52] interfaced with a modified version of `CAMB` to directly solve the linearized scalar field equations [53]. Details are provided in Appendix 2.A. We model the neutrinos as two massless and one massive species with $m_\nu = 0.06$ eV and $N_{\text{eff}} = 3.046$. We use a dataset consisting of *Planck* 2018 measurements of the CMB via the `TTTEEE Plik lite` high- ℓ , `TT` and `EE` low- ℓ , and lensing likelihoods [54]. The `Plik lite` likelihood is a foreground and nuisance marginalized version of the `Plik` likelihood [54]. We have found that the two datasets return nearly identical posterior distributions for a typical AQ model. Based on this, we infer that the AQ model has negligible effect on the *Planck* nuisance parameters, allowing us to use the `lite` likelihood in place of the full likelihood, and speeding up our MCMC analysis. We restrict ourselves to only CMB data to determine whether a scaling field can independently raise the CMB-derived value of the Hubble constant, without the influence of late universe measurements, although we give results for extended datasets in Appendix 2.B.

We perform an analysis with a Metropolis-Hastings algorithm with flat priors on the six standard cosmological parameters $\{\omega_b, \omega_c, \theta_s, \tau, \ln(10^{10} A_s), n_s\}$ as well as the model parameters β and μ . Our results are obtained by running eight chains and monitoring convergence via the Gelman-Rubin criterion, with $R - 1 < 0.05$, for all parameters, being considered complete convergence [55]. Throughout this paper we absorb a factor of $(8\pi G)^{1/2}$ into the parameter β , allowing us to report it as a unitless scale parameter, matching its implementation within `CAMB`. Similarly, we report μ in

¹Publically available at: <https://cosmologist.info/cosmomc/>

units of $\text{Mpc}^{-1/2}$ where we absorb a factor of $(8\pi G)^{1/4}$.

Section 2.3

Observational Constraints

In this section we explore the implications of adding an AQ field for CMB-derived cosmological parameters. For fixed β and μ we show that the homogeneous AQ field can provide a resolution to the Hubble tension. However, the scaling behavior leads to strong perturbations that spoil the concordance. We then explore the model parameter space and show that the data ultimately prefers AQ models that resemble ΛCDM .

2.3.1. Fixed Model Parameters

We fix the model parameters to $\beta = 12$ and $\mu = 3.5 \text{ Mpc}^{-1/2}$ such that the AQ field provides an approximately 4% spike in the background energy density in the epoch between matter-radiation equality and recombination, as shown in Fig. 2.2. An early contribution of this size should be enough to raise the value of the Hubble constant inferred by CMB measurements [41, 42].

We consider two alternative models for comparison. The first is ΛCDM , as a control. The second is also an AQ model with $\beta = 12$ and $\mu = 3.5 \text{ Mpc}^{-1/2}$, but for which the AQ velocity divergence is artificially set to zero, $\theta_\phi = 0$. We refer to this model as “semi-background”. Without the inclusion of the velocity divergence, this model is self-inconsistent. However, we find the model to be helpful to illustrate the influence of the velocity divergence on cosmological parameters in this scenario. Note that the inclusion of the density perturbation of the field has little effect on the temperature and polarization anisotropies since the total energy density perturbation is dominated by CDM.

The results of the MCMC analysis, consisting of constraints to the cosmological parameters for the AQ cosmology, the “semi-background” AQ cosmology, and Λ CDM, are presented in Table 2.1. We show the posterior distributions for the relevant parameters in these models in Fig. 2.5.

These constraints paint an interesting picture. The AQ “semi-background” model yields a best-fit value of $H_0 = 72.98$ km/s/Mpc, in excellent agreement with the SH0ES determination of H_0 . Hence, our initial rationale for selecting this model is justified. However, the quality of the fit to the data is poor compared to Λ CDM, as seen in the increased χ^2_{\min} . This is nearly entirely due to the self-inconsistency of the model. Without the complete evolution of field perturbations, terms that normally cancel the strong, late-time ISW effect in the CMB are absent leading to a huge increase in power in the large scale CMB anisotropy pattern [56]. Restoring the velocity divergence, the AQ cosmology with $\beta = 12$ and $\mu = 3.5$ Mpc $^{-1/2}$ yields a surprise. The model not only fails to solve the Hubble tension but exacerbates it even further, giving a best-fit value of $H_0 = 64.29$ km/s/Mpc as shown in Table 2.1. What these results suggest is that at the homogeneous level, the spike in the energy density given by the AQ field would indeed raise the CMB inferred value of the Hubble constant. But the dominant role of the AQ contribution to the heat flux spoils the concordance.

We can now take a sharper look at the role of the AQ perturbations, with the benefit of hindsight of the parameter analysis. We use the best-fit parameter values determined for the “semi-background” model, and apply them to the full AQ model. This enables us to see the effect of the heat flux on the metric perturbations and the full CMB anisotropy.

During the matter era, the density contrast of the AQ field is constant, meaning the density perturbation $\delta\rho_\phi$ must be losing energy. This is matched by the growth

of the heat flux $q_\phi = 8\pi G a^2(\rho_\phi + p_\phi)\theta_\phi$, shown in Fig. 2.3. This behavior has the same effect as the free-streaming of photons and neutrinos out of potential wells, bringing energy with them as they go. This outflow of energy causes rarefaction of the gravitational potential wells when compared to Λ CDM, as shown in Fig. 2.4.

The change in the potential wells has widespread consequences. Most importantly for the Hubble tension, there is now an additional integrated Sachs-Wolfe (ISW) effect driven by the AQ heat flux. For the parameters of these models, this new ISW raises the power of the CMB spectrum across the first acoustic peak. To compensate for this change, there is a series of parameter changes when compared to Λ CDM, as shown in Table 2.1. Most notably, the CDM density is increased, which introduces a phase shift in the acoustic oscillations toward larger angular scales for all multipoles. To maintain the correct angular scale of the acoustic peaks, H_0 is lowered.

The residual between the best-fit Λ CDM model and our AQ model, shown in Fig. 2.6, makes these parameter changes clearer. In the solid red line we show the residual for the best-fit AQ model using the full *Planck* dataset and in orange we show the residual for the AQ model using standard model parameters specified by the best-fit Λ CDM model. Setting the standard model parameters to their Λ CDM values and adding in an AQ field allows us to illustrate the full influence of the AQ field on the CMB spectrum. In the AQ model with Λ CDM parameters, the oscillation in the residual seen at high- ℓ in both temperature and polarization shows a phase-shift toward high- ℓ , which can be remedied by a higher value of H_0 . However, the additional ISW effect caused by the domination of the heat flux of the AQ field, seen most clearly between $10 < \ell < 400$, is too strong to overcome. When we shift the parameter values to match the best-fit AQ model, the higher CDM density and lower value of H_0 deepen the gravitational potentials, and restore the angular scale of acoustic oscillations, resulting in a closer match to the data, although one that is still

not on par with Λ CDM. This poor fit is consistent among the individual likelihoods in the *Planck* 2018 dataset (to remind, these are: high- ℓ TT,TE,EE; low- ℓ TT; low- ℓ EE; lensing). The biggest deviation comes from the high- ℓ TT,TE,EE likelihood with $\Delta\chi^2_{min} \approx 25$, supported by the offset of the best-fit AQ model residuals from the *Planck* 2018 data points in Fig. 2.6.

The overall change in level of the gravitational potentials also leaves imprints on the matter power spectrum, which can be summarized through the parameter $S_8 = \sigma_8(\Omega_m/0.3)^{1/2}$. Weak lensing surveys like KiDS-450 measure $S_8 = 0.745 \pm 0.039$ [57]. This is in a $\sim 2\sigma$ tension with the high value of $S_8 = 0.832 \pm 0.013$ estimated by *Planck* using Λ CDM [58]. We can see from Table 2.1 that the “semi-background” model lowers the value of S_8 estimated by *Planck* data into agreement with the local universe measurement from KiDS-450. However, similarly to H_0 , when the velocity divergence is restored to the AQ model, this concordance is lost, and the tension is exacerbated.

With a lower preferred value of H_0 and a worse fit to the full *Planck* 2018 dataset, it seems that the scaling behavior present in this model, which provides a natural link between early and late dark energy as well as a framework to solve the “why now” problem, is the very mechanism that spoils this model as a solution to the Hubble tension.

2.3.2. Full Results

We now promote β and μ to free parameters and allow them to vary alongside the six standard model parameters with flat priors, $5 < \beta < 30$ and $0.0001 < \mu < 20$ $\text{Mpc}^{-1/2}$. We leave out $\mu = 0$ for numerical stability within **CAMB**. The parameter constraints derived from the *Planck* 2018 dataset are presented in Table 2.2, with posterior distributions for the relevant parameters shown in Fig. 2.7. We include the posteriors for the best-fit Λ CDM model for comparison.

It is clear from Fig. 2.7 that the data prefers high values of β and low values of μ . For the best-fit value of $\beta = 23.1$, the AQ field constitutes $< 1\%$ of the total energy density once it settles to its scaling solution. For such a low density component, the time that the AQ field thaws from the Hubble friction is inconsequential, resulting in a wide spread in the posterior distribution of μ . However, the best-fit value of $\mu = 0.005 \text{ Mpc}^{-1/2}$ and the preference for $\mu < 7.07 \text{ Mpc}^{-1/2}$ gives us some insight into these results.

As previously discussed, low values of μ correspond to later activation of the AQ field, meaning the field behaves like a cosmological constant with a negligible energy density for most of its evolution. For the best-fit values of $\beta = 23.1$ and $\mu = 0.005 \text{ Mpc}^{-1/2}$, the AQ field thaws from the Hubble friction during dark energy domination at which time its scaling behavior forces it to behave as an additional, subdominant cosmological constant. In this case, the field forgoes the post-recombination decay of gravitational potentials caused by the domination of the heat flux of the AQ field during the matter-era, allowing for the best-fit matter densities to remain unchanged from their values in the Λ CDM model. However, Fig. 2.7 shows us that even an AQ field present with a small abundance shifts the peak of the posterior distribution of H_0 toward smaller values, furthering the evidence that this model cannot resolve the Hubble tension.

The best-fit AQ cosmology, introducing a new component that makes up $< 1\%$ of the total energy density, is statistically indistinguishable from Λ CDM with $\Delta\chi^2_{\text{min}} = -0.53$. These results tell us there is little to no evidence for the presence of an AQ scaling field within the full *Planck* 2018 dataset.

We note that the changes to the gravitational potentials discussed in Sec. 2.3.1 also affect the imprint of gravitational lensing on the CMB power spectrum. As CMB photons travel along the line-of-sight, they are gravitationally deflected by the large-

Parameter	β, μ free
$100\omega_b$	$2.232 (2.237) \pm 0.015$
ω_c	$0.1220 (0.1199)^{+0.0014}_{-0.0015}$
$100\theta_s$	$1.04061 (1.04078) \pm 0.00033$
τ	$0.0565 (0.0543) \pm 0.0076$
$\ln(10^{10} A_s)$	$3.052 (3.049) \pm 0.015$
n_s	$0.9630 (0.9647) \pm 0.0042$
β	$> 25.6 (23.1)$
$\mu [\text{Mpc}^{-1/2}]$	$< 7.07 (0.005)$
$H_0 [\text{km/s/Mpc}]$	$66.52 (67.22) \pm 0.58$
S_8	$0.839 (0.833) \pm 0.013$
Total χ^2_{\min}	1013.56

Table 2.2: The mean (best-fit) $\pm 1\sigma$ error of the cosmological parameters in the full AQ model analyzed using the *Planck* 2018 dataset.

scale distribution of matter in the Universe. This lensing effect blurs the anisotropy pattern and smooths the acoustic peaks. When we artificially turn off the effects of CMB lensing and use only *Planck* high- ℓ TT, TE, EE, and low- ℓ TT and EE data, we find that the AQ model provides a statistically better fit to the data than Λ CDM. Results for this analysis in the AQ model with free β and μ are shown in Appendix 2.C. However, due to the scaling of the AQ field, the gravitational potentials are shallower, implying less blurring and smoothing. Turning lensing back on results in a poorer relative fit to data than Λ CDM. When considering the S_8 tension between *Planck* and local universe weak lensing surveys, and the A_L anomaly present in *Planck* data [59], these results become more interesting and may warrant further investigation.

Section 2.4

Discussion and Conclusions

The Hubble tension has motivated a variety of extensions to the standard Λ CDM cosmological model, most of which focus on injecting energy at or around the time of matter-radiation equality. In this paper we considered the possibility that a scal-

ing field which activates just prior to recombination provides this energy injection. Specifically, we evaluated the impact on the CMB of a scalar field with an exponential tracking potential of the form $V(\phi) = \mu^4 e^{-\beta\phi}$ in the context of an AQ scenario for EDE and DE. This model constitutes a two parameter extension to the standard Λ CDM model specified by the steepness of the potential β , and the effective mass of the field μ . In this scenario, early dark energy is simply a sign of the build up of dark energy.

The Hubble tension would appear ameliorated at the background level by a scenario with $\beta = 12$ and $\mu = 3.5 \text{ Mpc}^{-1/2}$. Solving for the dynamics of the linearized perturbations of the field, however, we find a different story. The scaling behavior of the AQ field results in the domination of the heat flux of the AQ field over that of the standard model components. The impact on the CMB power spectrum actually worsens the Hubble tension to an almost 7σ difference with local universe measurements. Ultimately, we find that *Planck* 2018 temperature and polarization data, plus *Planck* estimates of the lensing potential, constrain the AQ model parameters to resemble a Λ CDM-like cosmology; the best-fit AQ model is statistically indistinguishable from Λ CDM.

The failure of this model offers insight into the ability of new physics to resolve the Hubble tension. In this case, the pressure fluctuation drives the growth of the heat flux on subhorizon scales as shown in Eq. 2.14. This sets off a cascade of effects, softening the gravitational potentials, shifting the acoustic peaks in the CMB, and ultimately exacerbating the Hubble tension. A few ways around this result are suggested. For example, if we abandon the scaling solution and use a model that spikes just prior to recombination and then decays faster than the background, then the pressure source decays, too. This is the method employed in Refs. [41, 43, 48, 60]. The price of which is an additional parameter, which may require the fine tuning of the initial

conditions. Another solution would be to introduce an additional term on the right hand side of Eq. 2.14 to damp or diminish the pressure. This might be accomplished by coupling to another field [61]. Yet neither of these fixes do more than soften the Hubble tension.

One would expect that a compelling solution would raise the CMB-inferred value of H_0 into complete agreement with local universe measurements while also addressing (or at the very least, not exacerbating) other cosmological tensions. This may require dropping the scalar field as a possible solution. If EDE does play a role in resolving the various tensions between Λ CDM and cosmological observations, it will necessarily have more structure than the most basic scenarios that have been considered. Currently, no model has succeeded at independently and adequately solving the Hubble tension. Improved measurements of the CMB, $H(z)$, and BAO at various redshifts will give us better insight into possible physics beyond the standard model.

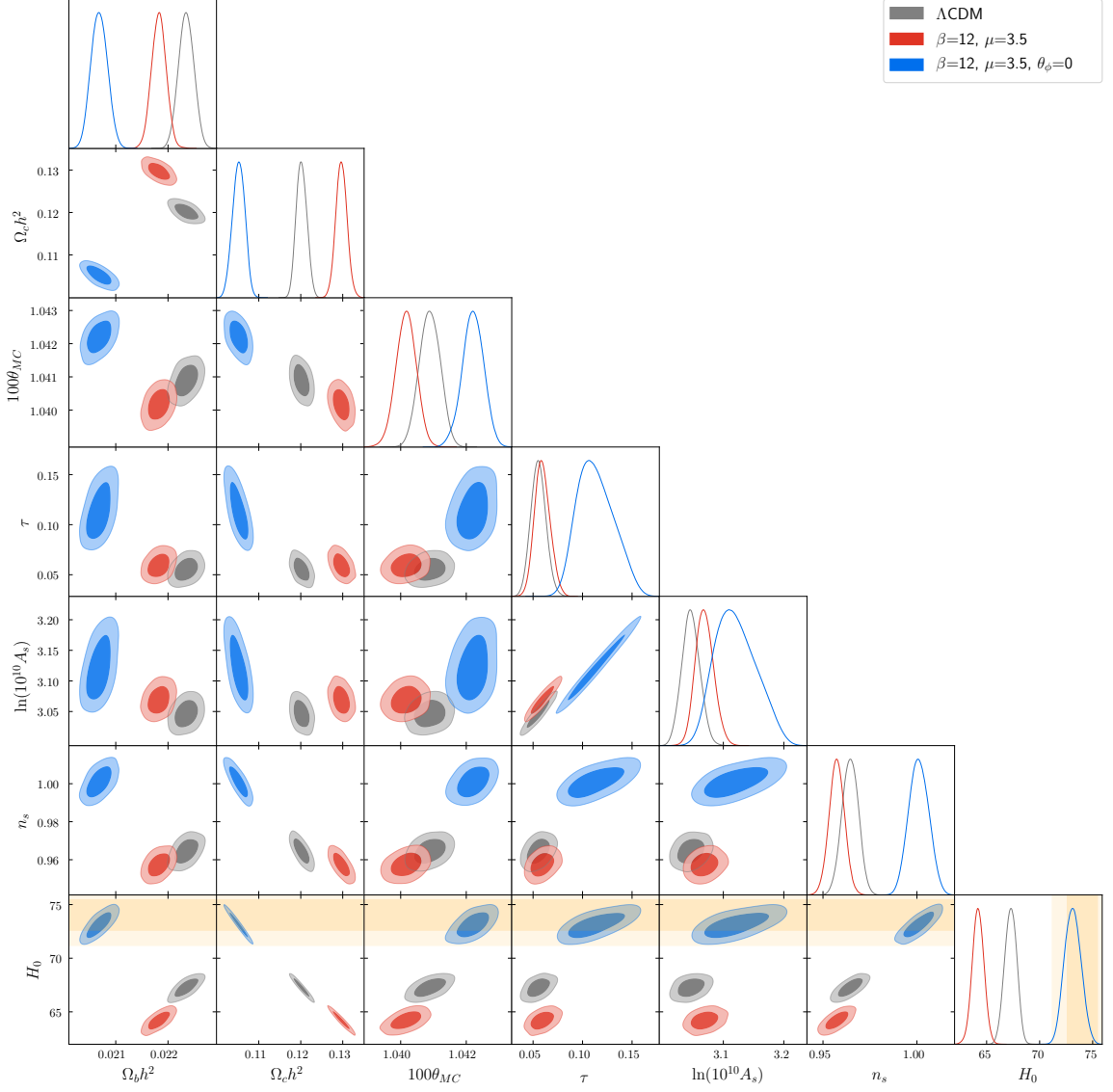


Figure 2.5: Posterior distributions of the AQ model with $\beta = 12$, $\mu = 3.5 \text{ Mpc}^{-1/2}$ and θ_ϕ turned on (red) and off (blue), and the Λ CDM model (gray) for the *Planck* 2018 dataset. The darker inner (lighter outer) regions correspond to 1σ (2σ) confidence intervals. The SH0ES determination of H_0 is shown in the orange bands.

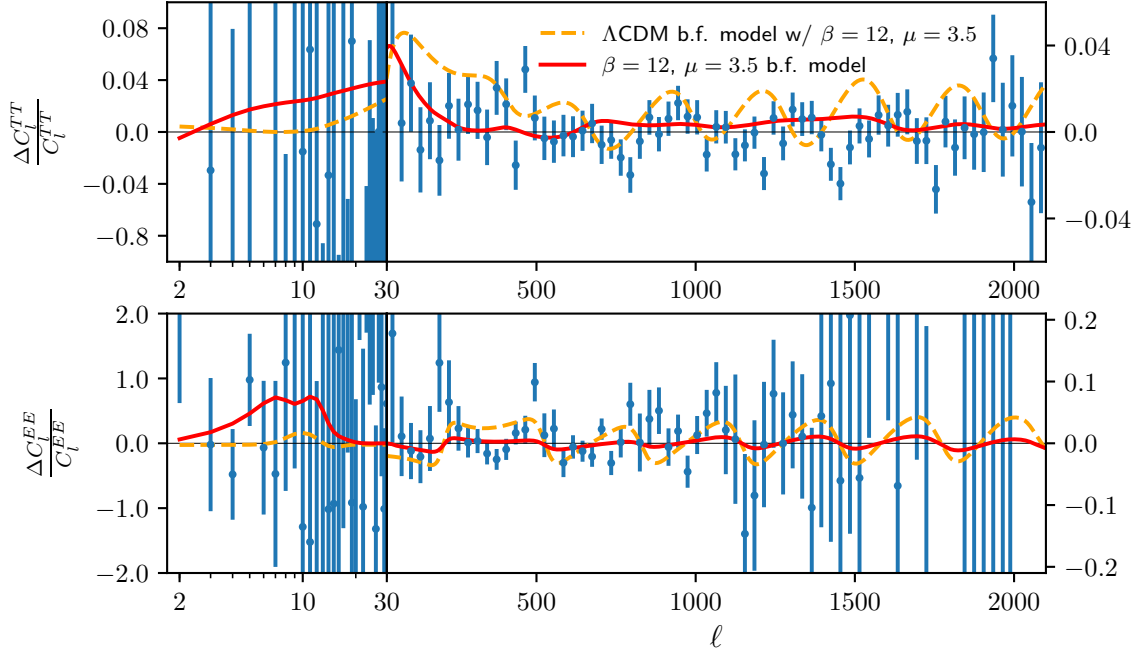


Figure 2.6: Temperature and polarization power spectrum residuals between the best-fit Λ CDM model and the best-fit AQ cosmology (solid red), as well as an AQ cosmology with the six standard model parameters unchanged from their best-fit Λ CDM values (dashed orange). We show the residuals from *Planck* 2018 data in blue. Left (right) vertical axis scaling is for multipoles less (greater) than 30.

2.4 DISCUSSION AND CONCLUSIONS

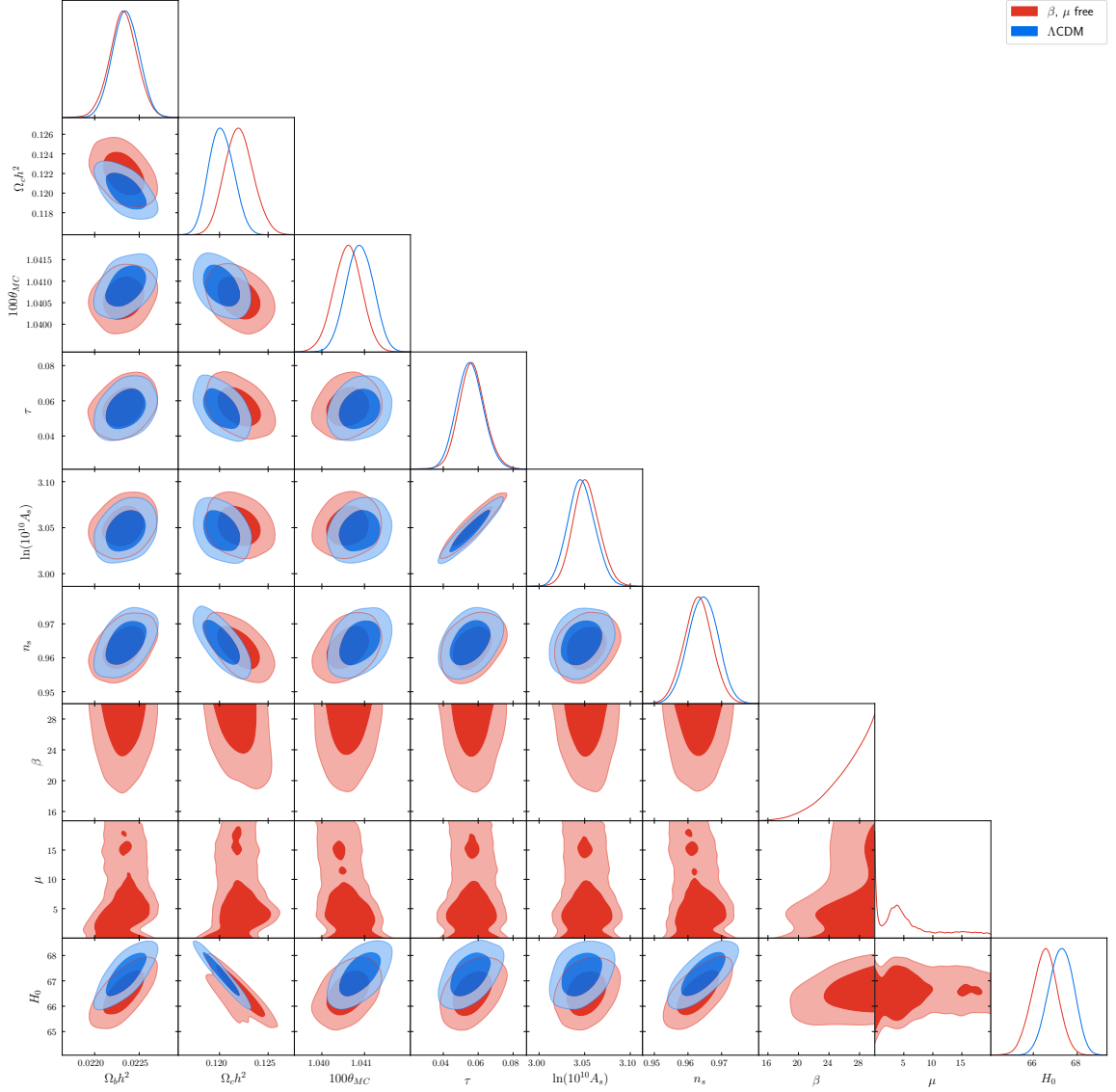


Figure 2.7: Posterior distributions of the AQ model with β , and μ as free parameters (red) and the Λ CDM model (blue) for the *Planck* 2018 dataset. The darker inner (lighter outer) regions correspond to 1 σ (2 σ) confidence intervals.

Appendix

Section 2.A

Numerical Implementation

In CAMB, the evolution of the perturbation equations and the construction of the angular power spectra require the background densities of all components to be specified throughout cosmic history. The standard model background densities all follow simple scaling relations for which only the present day density is needed to completely specify their evolution. The background evolution of the AQ field is non-trivial and must be numerically solved prior to the evolution of the perturbations in order to obtain accurate results. The background evolution of the field is specified by the homogeneous Klein-Gordon equation, which requires initial conditions on ϕ and ϕ' in order to be evolved. For the exponential potential we can absorb the initial value of ϕ into the parameter μ , allowing us to set $\phi_i = 0$. The use of a tracker potential means that for a wide range of initial values of ϕ' , the field will settle to its attractor solution, hence we can arbitrarily set $\phi' = 0$, following slow-roll conditions. With initial conditions set, we numerically solve Eq. (2.5) to create arrays of values for ϕ and ϕ' over cosmic time which we interpolate whenever background values for the field are needed during the evolution of the cosmological perturbations.

The evolution of the AQ field fluctuations are solved numerically alongside the

standard model perturbations. To properly interface the scalar field with the standard model components, we need to translate the field perturbations into fluid variables. Linearly perturbing the scalar field stress-energy tensor yields:

$$\delta\rho_\phi = a^{-2}\phi'\delta\phi' + V_{,\phi}\delta\phi, \quad (2.16)$$

$$\delta p_\phi = a^{-2}\phi'\delta\phi' - V_{,\phi}\delta\phi, \quad (2.17)$$

$$(\rho_\phi + p_\phi)\theta_\phi = \frac{k^2}{a^2}\phi'\delta\phi, \quad (2.18)$$

$$(\rho_\phi + p_\phi)\sigma_\phi = 0, \quad (2.19)$$

where $\theta_\phi = ik^j v_j$ represents the velocity divergence, and σ_ϕ is the anisotropic stress, which is zero for a scalar field. Using these, we can show that the conservation of the scalar field stress-energy follows that of a single uncoupled fluid [49]:

$$\delta'_\phi = -(1 + w_\phi) \left(\theta_\phi + \frac{h'}{2} \right) - 3\mathcal{H} \left(\frac{\delta p_\phi}{\delta \rho_\phi} - w_\phi \right) \delta_\phi, \quad (2.20)$$

$$\theta'_\phi = -\mathcal{H}(1 - 3w_\phi)\theta_\phi - \frac{w'_\phi}{1 + w_\phi}\theta_\phi + \frac{\delta p_\phi/\delta \rho_\phi}{1 + w_\phi}k^2\delta_\phi, \quad (2.21)$$

where $\delta_\phi = \delta\rho_\phi/\rho_\phi$ and $\delta p_\phi/\delta\rho_\phi = c_\phi^2$ gives the adiabatic sound speed squared. While these fluid equations of motion are mathematically equivalent to the linearized KG equation, they are numerically unstable in practice since $w_\phi = -1$ prior to the slow roll of the field. In our numerical implementation we instead directly evolve the linearized KG equation, Eqs. (2.12), and construct the necessary fluid variables using Eq. 2.16-2.19.

In CAMB, distance and time are measured in Mpc. For numerical simplicity, we absorb a factor of $(8\pi G)^{1/2}$ into β and a factor of $(8\pi G)^{1/4}$ into μ so that

$$\frac{1}{2} \left(\frac{\phi'}{a^2} \right)^2 + V(\phi) = 8\pi G\rho \quad (2.22)$$

2.B EXTENDED RESULTS FOR FIXED MODEL PARAMETERS

CMB+BAO	Λ CDM	$\beta = 12, \mu = 3.5$
$100\omega_b$	$2.240 (2.240) \pm 0.013$	$2.217 (2.220) \pm 0.014$
ω_c	$0.11947 (0.11954) \pm 0.00097$	$0.1247 (0.1246) \pm 0.0011$
$100\theta_s$	$1.04098 (1.04103) \pm 0.00030$	$1.04075 (1.04086) \pm 0.00028$
τ	$0.0573 (0.0570) \pm 0.0074$	$0.0739 (0.0736) \pm 0.0093$
$\ln(10^{10} A_s)$	$3.049 (3.048) \pm 0.014$	$3.089 (3.090) \pm 0.018$
n_s	$0.9663 (0.9659) \pm 0.0038$	$0.9685 (0.9688) \pm 0.0038$
β	-	12 (fixed)
$\mu [\text{Mpc}^{-1/2}]$	-	3.5 (fixed)
$H_0 [\text{km/s/Mpc}]$	$67.59 (67.58) \pm 0.44$	$66.33 (66.43) \pm 0.46$
S_8	$0.828 (0.828) \pm 0.011$	$0.815 (0.814) \pm 0.011$
Total χ^2_{min}	1020.02	1082.89

Table 2.A.1: The mean (best-fit) $\pm 1\sigma$ error of the cosmological parameters for Λ CDM and the AQ model with $\beta = 12, \mu = 3.5 \text{ Mpc}^{-1/2}$. Constraints are based on the CMB and BAO datasets.

has units of Mpc^{-2} . To convert to standard particle physics units, remember that $1 \text{ Mpc} = 1.5637 \times 10^{38} \text{ GeV}^{-1}$. Converting the model parameters presented in Sec. 2.3.1 from CAMB units to particle physics units gives $\beta = 5 \times 10^{-18} / \text{GeV}$, and $\mu = 0.43 \text{ eV}$.

Section 2.B

Extended Results for Fixed Model Parameters

In this Appendix we present an extended MCMC analysis on the AQ model with fixed model parameters. To fully analyze the cosmological impact of the AQ model we use a wider range of cosmological datasets for parameter estimation:

- **Cosmic Microwave Background (CMB):** We use the Planck 2018 measurements of the CMB (via TTTEEE Plik lite high- ℓ , TT and EE low- ℓ , and lensing likelihoods [54],
- **Baryon acoustic oscillation (BAO) data:** We use data from the BOSS survey (data release 12) at $z = 0.38, 0.51$, and 0.61 [62], low redshift measurements from the 6dF survey at $z = 0.106$ [63], and the BOSS main galaxy sample at

2.B EXTENDED RESULTS FOR FIXED MODEL PARAMETERS

CMB+BAO+R19	Λ CDM	$\beta = 12, \mu = 3.5$
$100\omega_b$	$2.252 (2.250) \pm 0.013$	$2.231 (2.230) \pm 0.014$
ω_c	$0.11837 (0.11819) \pm 0.00095$	$0.12317 (0.12313) \pm 0.00098$
$100\theta_s$	$1.04113 (1.04117) \pm 0.00029$	$1.04092 (1.04105) \pm 0.00028$
τ	$0.0608 (0.0589) {}^{+0.0071}_{-0.0080}$	$0.081 (0.079) \pm 0.010$
$\ln(10^{10} A_s)$	$3.054 (3.051) {}^{+0.014}_{-0.016}$	$3.100 (3.095) \pm 0.019$
n_s	$0.9689 (0.9702) \pm 0.0037$	$0.9721 (0.9728) \pm 0.0039$
β	-	12 (fixed)
$\mu [\text{Mpc}^{-1/2}]$	-	3.5 (fixed)
$H_0 [\text{km/s/Mpc}]$	$68.13 (68.18) {}^{+0.39}_{-0.43}$	$67.05 (67.09) \pm 0.43$
S_8	$0.817 (0.814) \pm 0.011$	$0.803 (0.801) \pm 0.011$
Total χ^2_{\min}	1039.15	1109.79

Table 2.A.2: The mean (best-fit) $\pm 1\sigma$ error of the cosmological parameters for Λ CDM and the AQ model with $\beta = 12, \mu = 3.5 \text{ Mpc}^{-1/2}$. Constraints are based on the CMB, BAO, and R19 datasets.

$$z = 0.15 [64],$$

- **Local Hubble constant measurement (R19):** The measurement of the local Hubble constant giving $H_0 = 74.03 \pm 1.42 \text{ km/s/Mpc}$ the SH0ES collaboration [30].

In a series of tables we show the constraints on cosmological parameters in Λ CDM and the AQ model with fixed model parameters utilizing the CMB and BAO datasets (Table 2.A.1), and the CMB, BAO, and R19 datasets (Table 2.A.2). We show the best-fit χ^2 for individual experiments in these models in Table 2.B.1. The posterior distributions for the relevant parameters are shown in Fig. 2.C.1 for the CMB and BAO datasets, and in Fig. 2.C.2 for the CMB, BAO and R19 datasets.

The inclusion of more cosmological data does not change the conclusions made in Sec. 2.3.1. The parameter changes we saw for *Planck* 2018 data alone shown in Table 2.1 are still present with the inclusion of more datasets. The difference between the best-fit value of H_0 in Λ CDM and the AQ model is narrowed when the BAO and R19 datasets are considered. However, the worse overall fits to the data in the AQ model

with fixed model parameters, tell us that this comes at a price. In particular, the AQ model provides a worse fit to the SH0ES likelihood than Λ CDM, as shown in Table 2.B.1, providing further proof that the effect of the scaling behavior on perturbations in this model are too great to overcome to resolve the H_0 tension.

Section 2.C

Extended Results for Free Model Parameters

In this Appendix we present the results of our MCMC analysis on Λ CDM and the AQ model with free model parameters utilizing the TTTEEE `Planck` `lite` high- ℓ , and TT and EE low- ℓ likelihoods. We give the constraints on cosmological parameters in Table 2.C.1 and the posterior distributions for all parameters in Fig. 2.C.3.

These constraints show that with the effect of CMB lensing turned off, an AQ scaling field which becomes dynamical after recombination provides a statistically better fit to the *Planck* temperature and polarization data than Λ CDM with $\Delta\chi^2_{\min} = -14.87$ as seen in Table 2.C.1. This is likely because the AQ field lowers the depth of gravitational potentials, smoothing the CMB spectrum which mimics the effect of gravitational lensing. Since the introduction of lensing results in a much better fit to *Planck* measurements in the Λ CDM model, the AQ field brings the AQ model into better agreement with *Planck* measurements by mimicking this effect. However the resulting best-fit value of the Hubble constant is $H_0 = 60.57$ km/s/Mpc. This result, combined with the “S8-tension” and the A_L anomaly present in *Planck* 2018 data, suggest the need for a more general analysis of cosmological data, with relaxed assumptions of dark energy, lensing, and expansion history.

Dataset	Λ CDM	$\beta = 12, \mu = 3.5$
<i>Planck</i> high- ℓ TT, TE, EE	588.29	619.76
<i>Planck</i> low- ℓ TT	22.50	23.08
<i>Planck</i> low- ℓ EE	396.99	408.21
<i>Planck</i> lensing	9.19	21.66
BAO low- z	1.75	0.67
BAO high- z	3.47	12.55
SH0ES	16.96	23.86
Total χ^2_{\min}	1039.15	1109.79

Table 2.B.1: The best-fit χ^2 per experiment for the standard Λ CDM model and the AQ model with $\beta=12$ and $\mu = 3.5 \text{ Mpc}^{-1/2}$. The BAO low- z and high- z datasets correspond to $0.1 < z < 0.15$ and $0.38 < z < 0.61$ respectively. Constraints are based on the CMB, BAO, and R19 datasets.

Parameter	Λ CDM	β, μ free
$100\omega_b$	$2.140 (2.142) \pm 0.015$	$2.097 (2.079) \pm 0.020$
ω_c	$0.1235 (0.1236) \pm 0.0015$	$0.1252 (0.1256)^{+0.0018}_{-0.0021}$
$100\theta_s$	$1.04031 (1.04031) \pm 0.00030$	$1.04024 (1.04032) \pm 0.00032$
τ	$0.0459 (0.0473)^{+0.0083}_{-0.0065}$	$0.0448 (0.0444)^{+0.0086}_{-0.0073}$
$\ln(10^{10} A_s)$	$3.026 (3.030)^{+0.017}_{-0.014}$	$3.018 (3.015)^{+0.019}_{-0.016}$
n_s	$0.9510 (0.9514) \pm 0.0045$	$0.9486 (0.9491) \pm 0.0052$
β	-	$13.3 (10.0)^{+1.6}_{-3.5}$
$\mu [\text{Mpc}^{-1/2}]$	-	$1.52 (1.35)^{+0.23}_{-0.51}$
$H_0 [\text{km/s/Mpc}]$	$65.17 (65.12) \pm 0.064$	$62.5 (60.57)^{+1.5}_{-1.1}$
S_8	$0.870 (0.873) \pm 0.019$	$0.836 (0.8216) \pm 0.026$
Total χ^2_{\min}	1575.67	1560.80

Table 2.C.1: The mean (best-fit) $\pm 1\sigma$ error of the cosmological parameters in the AQ model with free β and μ from our run using only *Planck* high- ℓ TT,TE,EE, and low- ℓ TT and EE data (i.e. no lensing).

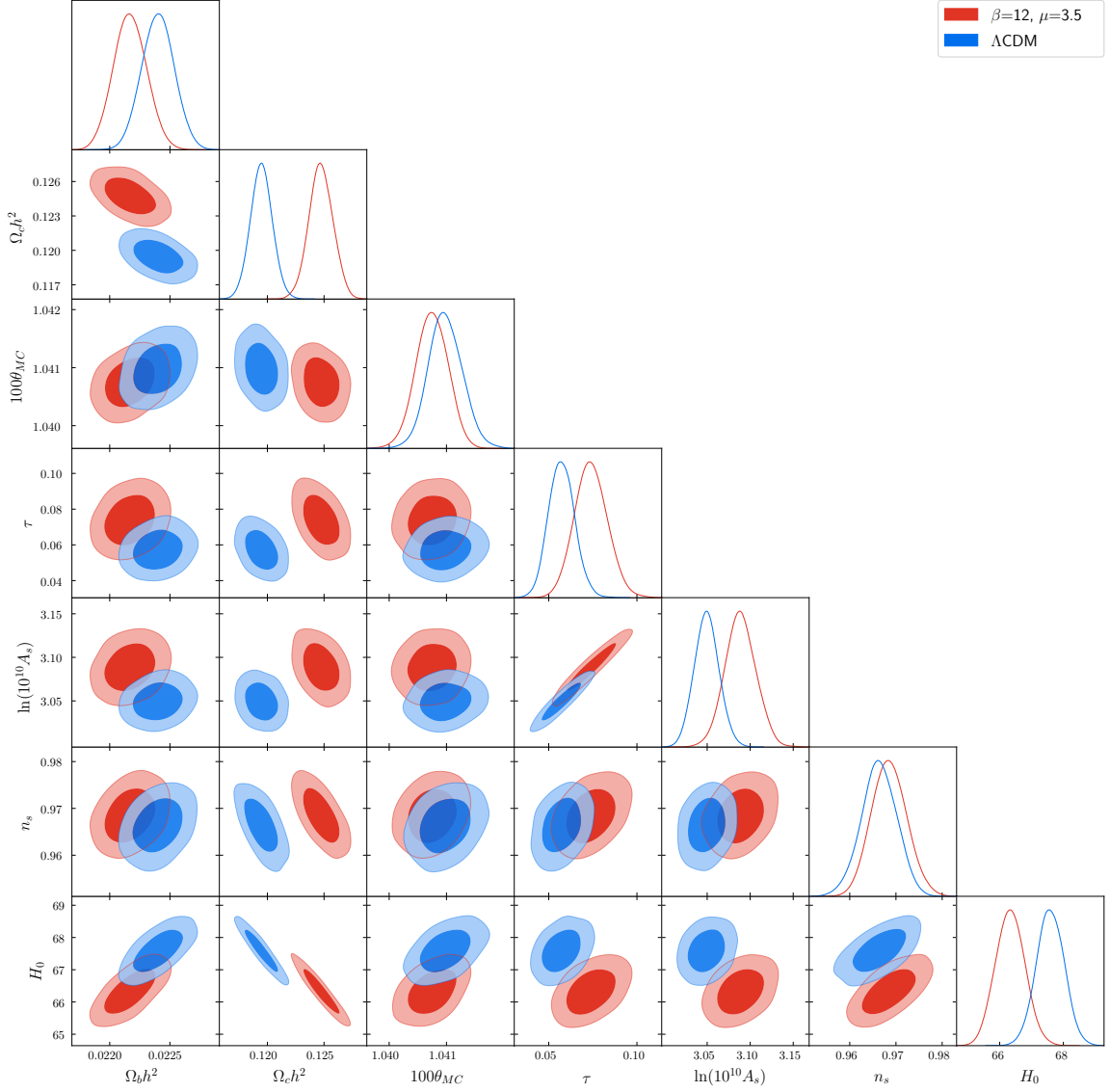


Figure 2.C.1: Posterior distributions of the AQ model with $\beta = 12$, and $\mu = 3.5$ $\text{Mpc}^{-1/2}$ (red) and the Λ CDM model (blue) based on CMB and BAO datasets. The darker inner (lighter outer) regions correspond to 1σ (2σ) confidence intervals.

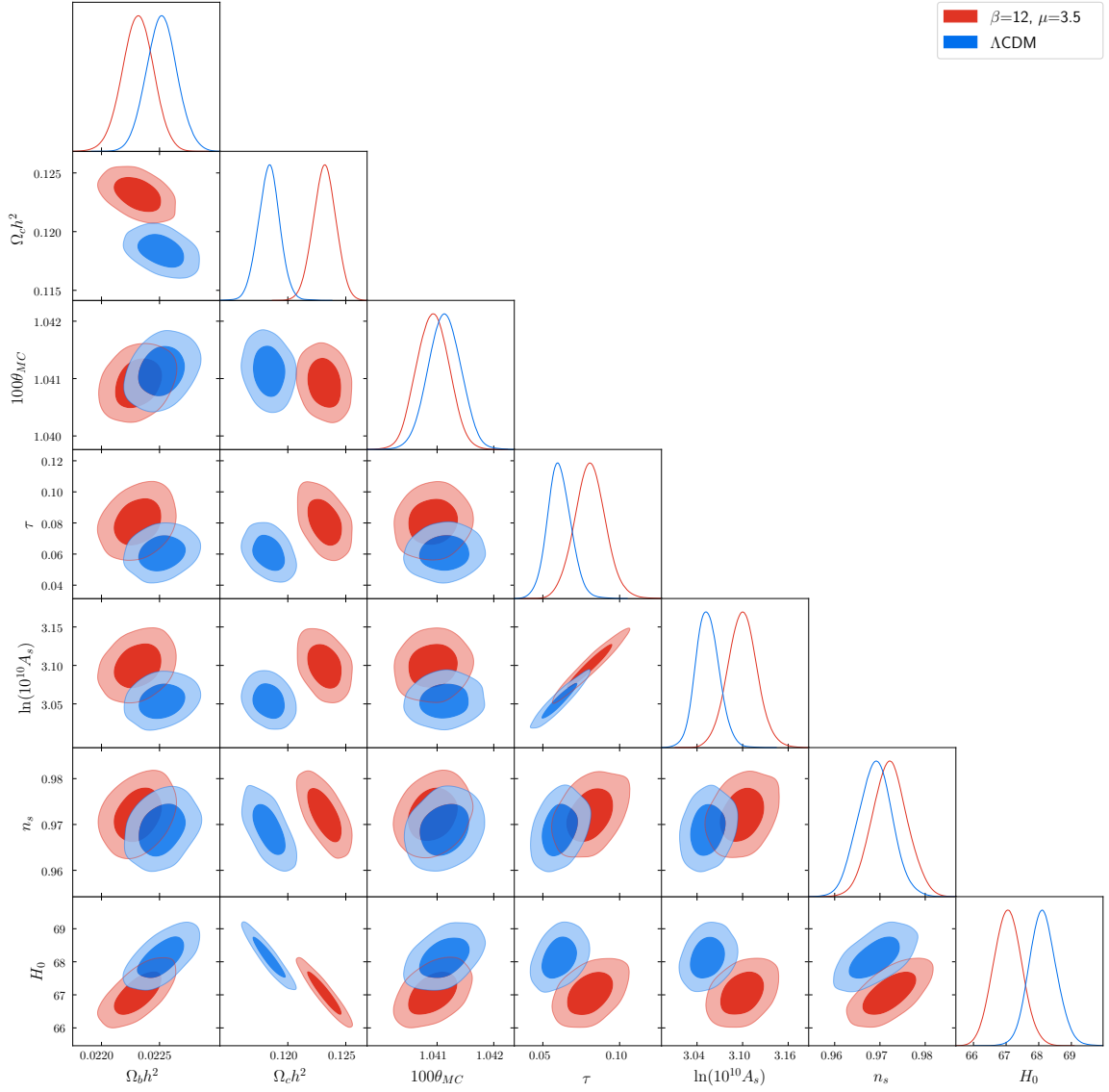


Figure 2.C.2: Posterior distributions of the AQ model with $\beta = 12$, and $\mu = 3.5$ $\text{Mpc}^{-1/2}$ (red) and the Λ CDM model (blue) based on CMB, BAO, and R19 datasets. The darker inner (lighter outer) regions correspond to 1σ (2σ) confidence intervals.

2.C EXTENDED RESULTS FOR FREE MODEL PARAMETERS

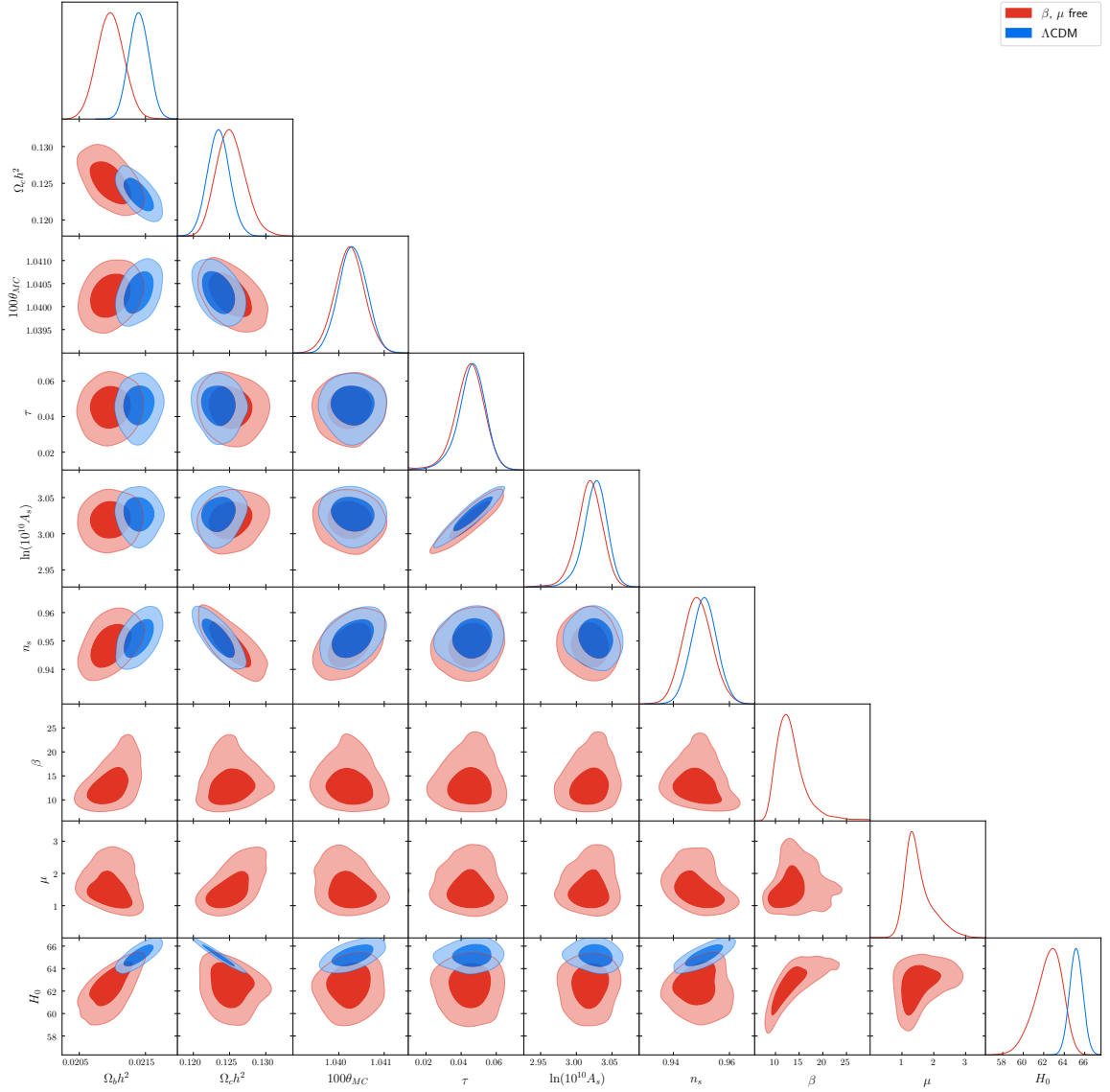


Figure 2.C.3: Posterior distributions for the AQ model with free β and μ (red) and the Λ CDM model (blue) for the *Planck* high- ℓ TT,TT,EE, and low- ℓ TT and EE data. The darker inner (lighter outer) regions correspond to 1σ (2σ) confidence intervals.

Chapter 3

Microphysics of Early Dark Energy

*With minor changes, this chapter is adapted from Sabla, V.I. & Caldwell, R.R. “Microphysics of early dark energy.” *Phys. Rev. D* **106**, 063526. *arXiv: 2202.08291* (2022).*

Early dark energy (EDE) has proven to be one of the most promising classes of early-universe solutions, with many models significantly reducing the H_0 tension, while yielding a comparable fit to the observational data compared to Λ CDM [20, 21, 65–79]. A leading example is standard EDE, consisting of a scalar field that briefly bumps up the expansion rate between equality and recombination.

However, the perturbative dynamics of the canonical scalar field used in these models appear to preclude a fully satisfactory solution. *Planck* data alone does not favor EDE as a cosmological model. It is only with the inclusion of a late-universe prior on H_0 that EDE is favored in non-negligible amounts. This is avoided in analyses with alternative CMB datasets, yet more work needs to be done to determine if these differing constraints are physical, or due to experimental systematics [20–22]. More importantly, EDE models tend to exacerbate the discrepancy between early- and late-universe measurements of the structure growth parameter, known as the “ S_8 tension”.

A possible interpretation of this continuing tension is that new physics is required, but it may not be a canonical scalar field.

Previous studies have investigated the implications of varying the sound speed in EDE-like models from its canonical scalar field value with favorable results [69, 73]. In this chapter, we pursue a description of EDE as a phenomenological fluid component, whose background evolution is matched to a family of viable EDE models. The perturbative dynamics of this EDE fluid are specified by a gauge-invariant sound speed, relating pressure and density perturbations, and a gauge-invariant anisotropic stress, modeled either via an equation of state inspired by proposed dark sector stress models [80, 81], or via an equation of motion formalism inspired by generalized dark matter models [82]. We refer to the constitutive relations necessary to define this perturbative sector as the microphysics of EDE. We explore what types of perturbative evolution is necessary to strengthen and improve on current EDE solutions to the Hubble tension, without specifying a particular physical model.

For canonical EDE scalar fields, the microphysics is fixed: the evolution of the perturbations follow that of a single, uncoupled fluid with no anisotropic shear, and a relationship between the density and pressure giving a gauge-invariant sound speed of $c_\phi^2 = 1$. By exploring deviations from this framework, specifically with the addition of anisotropic shear, we implicitly explore the viability of non-scalar field EDE. Examples of theoretical models that yield anisotropic stress include free-streaming neutrinos [83] as well as more exotic cases such as topological defects, cosmic lattice models such as elastic dark energy, and coherent vector fields [81, 84–90]. However, these models are not specifically known to predict the full range of properties (equation of state history, parallel and perpendicular sound speeds) that are investigated in this paper. Instead, we have constructed phenomenological models with generalized properties beyond the specific examples. This approach is similar in spirit to

generalized dark matter [82] and elastic dark energy [80, 81] constructions.

We find that EDE with an added anisotropic stress can simultaneously soften both the H_0 and S_8 tensions when compared to a scalar field EDE model, implying that EDE need not be the result of a scalar field. Current data cannot definitively discriminate among these possibilities, but future measurements may be more decisive.

This chapter is organized as follows. In Sec. 3.1 we outline our phenomenological fluid parametrization of EDE. We describe the background solution to the Hubble tension as well as the different microphysics variations that we analyze. In Sec. 3.2, we present the cosmological data used to test the viability of the different microphysics scenarios. Results are given in Sec. 3.3, and we conclude our discussion in Sec. 3.4 with our main findings. Additional details about the models considered and extended results can be found in the Appendixes.

Section 3.1

Phenomenological Fluid Model (PFM)

We work in a scenario consisting of the standard cosmological model with cold dark matter (CDM), and dark energy in the form of a cosmological constant. We introduce an EDE component in the form of a phenomenological fluid with perturbative dynamics that differ from a canonical scalar field. In this section we describe the background fluid dynamics and introduce the constitutive relations necessary to consistently describe the microphysics.

3.1 PHENOMENOLOGICAL FLUID MODEL (PFM)

3.1.1. Background dynamics

Our proposed scenario mimics the background evolution of standard EDE by specifying a time-varying equation of state

$$w_\phi(a) = -1 + \frac{2}{1 + (a_t/a)^n}, \quad (3.1)$$

which evolves from $w_\phi = -1$ to $w_\phi = 1$ at a time given by the transition scale factor a_t , as shown in Fig. 3.1.1. The sharpness of this transition is controlled by the parameter n with higher n corresponding to a faster and sharper transition in the equation of state. This transition in w_ϕ resembles the thaw of a scalar field from the Hubble friction, causing the energy density in our phenomenological fluid to spike in a similar fashion, as shown in Fig. 3.1.2. We control the amount of energy added by this fluid component by setting the energy density of EDE in the present day $\rho_{\phi,0}$. In turn, the evolution of the energy density in the phenomenological fluid is given by

$$\rho_\phi(a) = \rho_{\phi,0} a^{-6} \left(\frac{1 + a_t^n}{1 + (a_t/a)^n} \right)^{6/n}. \quad (3.2)$$

Equations (3.1) and (3.2) give us a background model for EDE as a phenomenological fluid, constituting a 3-parameter extension to Λ CDM.

Our EDE fluid model differs from the effective fluid approximation of EDE presented in Ref. [72] mainly through the definition of the equation of state. Reference [72] defines

$$w_\phi(a) = \frac{1 + w_n}{1 + (a_c/a)^{3(1+w_n)}} - 1, \quad (3.3)$$

where $w_n = (n_{\text{std}} - 1)/(n_{\text{std}} + 1)$. Here the “std” subscript indicates Ref. [72] variables as distinct from our parameters. In Ref. [72], the equation of state transitions from a value of $w_\phi = -1$ to w_n at a time specified by a transition scale factor a_c . Hence,

3.1 PHENOMENOLOGICAL FLUID MODEL (PFM)

the parameter n_{std} effectively controls the rate at which the energy density in the field dilutes after becoming dynamical. In contrast, the final equation of state in our phenomenological EDE fluid is fixed to $w_\phi = 1$, with the energy density diluting as a^{-6} , and our parameter n controls the sharpness of the transition from the starting value of w_ϕ . For constraints on the final equation of state see Refs. [69, 72]. We choose the parametrization given in Eq. (3.1) to more generally model a component whose energy density “gets out of the way” fast enough to not have adverse effects at the background level, allowing us to focus on the perturbative changes discussed in Sec. 3.1.2. However, these two parametrizations are equivalent for the cases of $n_{\text{std}} = \infty$ and $n = 6$. At the background level, with $n = 6$, $a_t = 3.1 \times 10^{-4}$, and $\log(10^{10}\Omega_0) = -3.95$, where $\Omega_0 = \rho_{\phi,0}/\rho_{\text{crit},0}$, this model faithfully reproduces the standard EDE best-fit $n_{\text{std}} = \infty$ model of Ref. [72].

EDE as a solution to the Hubble tension is grounded in the theoretical description of the CMB angular power spectrum. The CMB is sensitive to H_0 via the angular size of the first acoustic peak, which can be modeled as $\theta_s = r_s(z_*)/D_A(z_*)$, where $r_s(z_*)$ is the comoving sound horizon at decoupling, and $D_A(z_*)$ is the comoving angular diameter distance to the surface of last scattering. The sound horizon, which depends on pre-recombination background energy densities, scales as $H_0^{-1/2}$, whereas $D_A(z_*)$, which is dependent on post-recombination energy densities, scales as H_0^{-1} . We may decrease the size of the sound horizon by adding new components to the energy density, and thereby expect an increase in the value of H_0 inferred from the CMB.

The above-described procedure is based solely on the background cosmological model. However, linear perturbations of all components of the cosmic fluid play a significant role in the creation of the CMB angular power spectrum.

3.1 PHENOMENOLOGICAL FLUID MODEL (PFM)

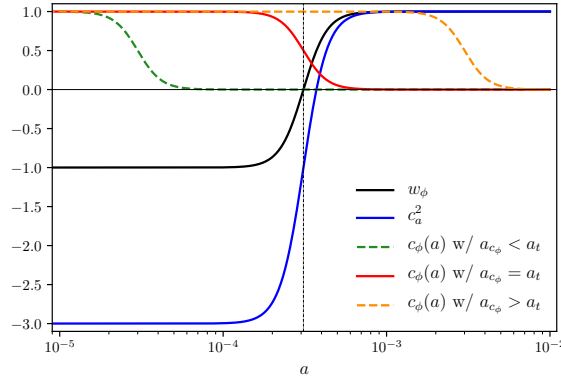


Figure 3.1.1: The evolution of the equation of state w_ϕ , the adiabatic sound speed c_a^2 , and the dynamical sound speed $c_\phi(a)$ for different values of a_{c_ϕ} as a function of scale factor for a model with $n = 6$ and $a_t = a_{c_\phi} = 3.1 \times 10^{-4}$. The vertical black dotted line delineates the transition scale factor a_t .

3.1.2. Perturbative microphysics

Standard, scalar field EDE is relativistic and does not cluster, which is manifest in the behavior of the density and velocity perturbations. As a result, EDE perturbations lead to an enhancement in power of the first acoustic peak of the CMB when compared to *Planck* data, which is compensated for by an increase in the dark matter density ω_{cdm} , and a subsequent increase in the spectral index n_s . These changes lead to a larger S_8 , increasing the S_8 tension, and restricting the amount of EDE allowed by the data. In fact, standard EDE never fully resolves the H_0 tension. In this work, we frame our EDE model as a phenomenological fluid and examine how changes to the microphysics affect the clustering response, and ultimately the proposed solution to the H_0 tension.

For a generalized fluid component, the standard description of linearized perturbations requires the specification of four variables: energy density, pressure, momentum density, and anisotropic stress. Traditionally, the pressure perturbation δp_ϕ is set via $c_s^2 = \delta p_\phi / \delta \rho_\phi$, where c_s^2 is the effective sound speed, normally set equal to unity, and $\delta \rho_\phi$ is the density perturbation. However, this formulation is gauge dependent

3.1 PHENOMENOLOGICAL FLUID MODEL (PFM)

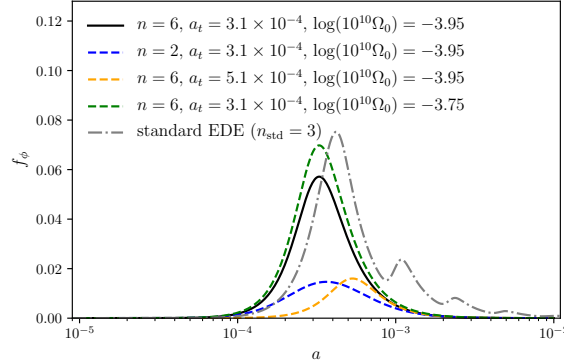


Figure 3.1.2: The evolution of $f_\phi = \rho_{\text{tot},\phi}/\rho_{\text{tot},\Lambda\text{CDM}} - 1$ as a function of scale factor. The black solid line shows our baseline model with $n = 6$, $\log(10^{10}\Omega_0) = -3.95$, and $a_t = 3.1 \times 10^{-4}$. The blue dashed line shows the baseline model with $n = 2$. The orange dashed line shows the baseline model with $a_t = 5.1 \times 10^{-4}$. The dotted green line shows the baseline with $\log(10^{10}\Omega_0) = -3.75$. The gray dot-dashed line shows the best-fit $n_{\text{std}} = 3$ oscillating scalar field model of EDE from Ref. [73] for comparison.

and lacks generality, so to be as exhaustive as possible we consider a gauge-invariant formulation of the pressure perturbation

$$\delta p_\phi = c_\phi^2 \delta \rho_\phi + 3\mathcal{H}(c_\phi^2 - c_a^2)(\rho_\phi + p_\phi)\theta_\phi/k^2, \quad (3.4)$$

where we work in Fourier space, θ_ϕ is the velocity divergence, and c_ϕ^2 is now the effective sound speed of our fluid, which is a free parameter in this generalized fluid formulation. The adiabatic sound speed c_a^2 takes on a simple form in our phenomenological model

$$c_a^2 \equiv \frac{p'_\phi}{\rho'_\phi} = w_\phi - \frac{w'_\phi}{3\mathcal{H}(1+w_\phi)} = w_\phi - \frac{n}{6}(1-w_\phi), \quad (3.5)$$

where primes denotes derivatives with respect to conformal time $' = \partial/\partial\tau$. In our scenarios, w_ϕ starts near -1 at early times. Consequently, the adiabatic sound speed starts out negative before evolving towards $c_a^2 = 1$ on the same time scale as the transition in the equation of state, as shown in Fig. 3.1.1 for a case with $n = 6$. The higher the value of n , the more negative the starting value of c_a^2 .

3.1 PHENOMENOLOGICAL FLUID MODEL (PFM)

Case	c_ϕ^2	A_σ	Description
1	0	0	pressure-less fluid
2	$c_\phi(a)$	0	dynamic c_ϕ with $a_{c_\phi} = a_t$
3	$c_\phi(a)$	0	dynamic c_ϕ with $a_{c_\phi} < a_t$
4	$c_\phi(a)$	0	dynamic c_ϕ with $a_{c_\phi} > a_t$

Table 3.1.1: Outline of various sound speed cases considered for the shear-less PFM model. In case 1 the sound speed is constant and set to $c_\phi^2 = 0$. Cases 2-4 consider the dynamical sound speed presented in Eq. (3.8) with different transition scale factors.

The conservation of the stress-energy tensor yields two equations of motion for the density contrast of the fluid $\delta_\phi = \delta\rho_\phi/\rho_\phi$ and the velocity divergence,

$$\delta'_\phi = -3\mathcal{H}(c_\phi^2 - w_\phi)\delta_\phi - (1 + w_\phi)\frac{h'}{2} - [k^2 + 9\mathcal{H}^2(c_\phi^2 - c_a^2)](1 + w_\phi)\theta_\phi/k^2 \quad (3.6)$$

$$\theta'_\phi = -\mathcal{H}(1 - 3c_\phi^2)\theta_\phi + \frac{c_\phi^2}{1 + w_\phi}k^2\delta_\phi - k^2\sigma_\phi \quad (3.7)$$

where $\mathcal{H} = a'/a$ is the conformal Hubble parameter, σ_ϕ is the anisotropic stress, h is the synchronous gauge metric potential (see [91]), and we have explicitly used our definition of the gauge-invariant pressure perturbation. From Eq. (3.6) and (3.7) we can see there are two free parameters that define the evolution of linear perturbations: the effective sound speed of the fluid, c_ϕ^2 , and the anisotropic shear σ_ϕ . It is through variation of these parameters that we test noncanonical EDE microphysics.

Varied sound speed. Our first test of microphysics comes with shear-less models where the only perturbative parameter we have to define is the sound speed c_ϕ^2 . The role of the gauge-invariant sound speed is dependent upon the time rate of change of the background equation of state. For a slowly varying equation of state, c_ϕ^2 determines the fluctuation response on subhorizon scales. Here, slow means $w'_\phi/w_\phi \lesssim a'/a$. Whereas for a rapidly varying equation of state, $w'_\phi/w_\phi \gtrsim a'/a$, a new scale is introduced into the system. Roughly speaking, for subhorizon perturbations in the

3.1 PHENOMENOLOGICAL FLUID MODEL (PFM)

range $a'/a \lesssim k \lesssim w'_\phi/w_\phi$, the effective sound speed may differ dramatically. Consider $c_{\text{eff}}^2 = \langle \delta p \rangle / \langle \delta \rho \rangle$, where the angle brackets indicate an appropriate time averaging. Only on smaller scales, $k \gtrsim w'_\phi/w_\phi$, does the gauge-invariant sound speed c_ϕ^2 play an important role. It is in this way that a rapidly oscillating scalar field can achieve a nonrelativistic sound speed, despite $c_\phi^2 = 1$. (See, for example, Refs. [92, 93].)

For the phenomenological fluid model described in Sec. 3.1.1, the equation of state changes slowly, allowing $c_\phi^2 = 1$ to represent a canonical scalar field. It would certainly be possible to introduce rapid variations in w_ϕ that affect the microphysics. However, designing such a $w_\phi(t)$ time history seems baroque in the absence of a particular underlying model to serve as a guide. Hence, for the purposes of this work, a fluid with $c_\phi^2 = 1$ will be used to delineate a scalar field-like model, with deviations from this value probing alternative microphysics scenarios.

We consider two distinct scenarios with varied sound speeds: (i) a constant sound speed $c_\phi^2 = 0$, giving a pressureless fluid, and (ii) a dynamical formulation of the sound speed such that

$$c_\phi^2(a) = 1 - \frac{1}{1 + (a_{c_\phi}/a)^n}. \quad (3.8)$$

In this dynamical model, the sound speed will transition from $c_\phi^2 = 1$, to $c_\phi^2 = 0$ at a time specified by a critical scale factor a_{c_ϕ} , as shown in Fig. 3.1.1. Similarly to the transition in the background equation of state, the sharpness of this transition is set by n . This transition in the sound speed can either occur simultaneously with the transition in the equation of state such that $a_{c_\phi} = a_t$, or a_{c_ϕ} can be altered to happen before or after the background transition as shown in Fig. 3.1.1. In this way we have four distinct cases of non-canonical sound speeds which we outline in Table 3.1.1. Case 1 gives our pressureless fluid with a constant sound speed $c_\phi^2 = 0$. Cases 2-4 consider the dynamical sound speed model with different values of sound speed transition scale factor a_{c_ϕ} .

3.1 PHENOMENOLOGICAL FLUID MODEL (PFM)

The acoustic dark energy (ADE) model of Ref. [69] explores the phenomenology of noncanonical constant sound speed in a similar EDE fluid model. They find that joint variations to the final equation of state and sound speed of the fluid can improve on the fit to cosmological data given in a canonical case. Our variations to the sound speed differ in that the final equation of state is held fixed at $w_\phi = 1$, and the sound speed is allowed to vary independently from the background evolution of the fluid. In this way, we explicitly probe changes to the perturbative sector, decoupled from the background fluid dynamics.

The background dynamics of our fluid give w_ϕ , and c_ϕ^2 is a free parameter that can vary as described above, leaving the anisotropic shear as the only variable left to define. Standard EDE has no shear, so we must look to other components for realistic models. We consider two different shear models, described below.

Shear models. For our first shear model, we follow the approach suggested in Ref. [81] to model dark sector stress in terms of a gauge invariant equation of state and define

$$(1 + w_\phi)\sigma_\phi = A_\sigma [\delta_\phi + 3\mathcal{H}(1 + w_\phi)\theta_\phi/k^2], \quad (3.9)$$

where A_σ is a free scaling parameter. Depending on the sign of A_σ this shear is built to damp or enhance the growth of the velocity perturbation at late times, resulting in changes to the evolution of the EDE density perturbation at the same scales. We will henceforth refer to this equation-of-state shear model, Eq. (3.9), as shear model I.

The second shear model we consider is derived from the density and velocity perturbations of our generalized fluid component and defines an equation of motion for the shear

$$\sigma'_\phi + 3\mathcal{H}(c_\phi^2 - c_a^2)\sigma_\phi + A_\sigma(\theta_\phi + \alpha k^2) = 0, \quad (3.10)$$

3.1 PHENOMENOLOGICAL FLUID MODEL (PFM)

where $\alpha = (h' + 6\eta')/2k^2$, and A_σ is again a free scaling parameter, just like in our previous shear model. Similarly to the generalized dark matter (GDM) stress presented in Ref. [82], we choose the shear to be sourced by the velocity perturbation θ_ϕ , with the metric perturbation term included for gauge invariance. In the limit that $c_\phi^2 = 1$ and $w_\phi = 0$, this equation exactly matches the GDM stress of Ref. [82]. By setting $c_\phi^2 = w_\phi = 1/3$, we recover the equation of motion for the stress given by a Boltzmann hierarchy for radiation truncated at the quadrupole [91]. This equation of motion formalism of the shear, Eq. (3.10), will henceforth be referred to as shear model II. Details on the specific form of both shear models considered can be found in Appendix 3.A.

Generalized shear behavior. To better understand the physical meaning of our microphysics parameters c_ϕ^2 and A_σ , it is instructive to think about the anisotropic shear within the context of the stress energy of our fluid. By perturbing the stress-energy tensor it is simple to show that shear is only nonzero when the pressure response to some scalar perturbation is anisotropic, with $\delta p = (\delta p_x + \delta p_y + \delta p_z)/3$ and $(\rho + p)\sigma = -(\hat{k}_i \hat{k}_j - \frac{1}{3}\delta_{ij})\delta T_j^i$. Let us now consider a mode travelling in the \hat{z} direction, and rotate our system such that $\delta p_x = \delta p_y = \delta p_\perp$ making $\delta p_z = \delta p_\parallel$. Combining this framework with our two shear models we find that we can write c_ϕ^2 and A_σ in terms of the perpendicular and parallel sound speeds of the fluid, such that

$$c_\phi^2 = \frac{1}{3} \left(2 \frac{\delta p_\perp}{\delta \rho} + \frac{\delta p_\parallel}{\delta \rho} \right) = \frac{1}{3} (2c_\perp^2 + c_\parallel^2), \quad (3.11)$$

and

$$A_\sigma = \frac{2}{3} \left(\frac{\delta p_\perp}{\delta \rho} - \frac{\delta p_\parallel}{\delta \rho} \right) = \frac{2}{3} (c_\perp^2 - c_\parallel^2), \quad (3.12)$$

in both shear models we consider. As expected, c_ϕ^2 is just the spatially averaged sound speed of our fluid. The amount of shear in our fluid, parametrized by A_σ , is controlled

by the difference in the directional sound speeds. For an isotropic pressure perturbation, $A_\sigma = 0$, and there is no shear contribution. When the pressure perturbation becomes anisotropic, $A_\sigma \neq 0$ and we have a nonzero shear contribution. This framework also gives us physical bounds on our model parameters c_ϕ^2 and A_σ . For stability and causality, $0 \leq c_\perp^2, c_\parallel^2 \leq 1$, which restricts $0 \leq c_\phi^2 \leq 1$ and $-2/3 \leq A_\sigma \leq 2/3$.

The equations of motion given in Eq. (3.6) and Eq. (3.7), coupled with either stress model constitute a full description of the perturbative sector dynamics. Besides the three background parameters n , Ω_0 , and a_t , there are now two additional free parameters describing the microphysics of our phenomenological EDE fluid, c_ϕ^2 and A_σ .

Section 3.2

Data and Methodology

We derive cosmological parameter constraints by running a complete Markov Chain Monte Carlo (MCMC) using the public code `CosmoMC` (see <https://cosmologist.info/cosmomc/>) [94] with modified versions of the Boltzmann solver `CAMB` to solve the different linearized perturbations in each of our microphysics scenarios [95]. We model neutrinos as two massless and one massive species with $m_\nu = 0.06$ eV and $N_{\text{eff}} = 3.046$. Our dataset includes different combinations of early and late time data described below:

- **P18:** *Planck* 2018 CMB measurements via the TTTEEE `plik lite` high- ℓ , TT and EE low- ℓ , and lensing likelihoods [96].
- **BAO:** We use data from the BOSS survey (data release 12) at $z = 0.38, 0.51$, and 0.61 [5], low redshift measurements from the 6dF survey at $z = 0.106$ [97], and the BOSS main galaxy sample at $z = 0.15$ [98].

- **R19:** Local Hubble constant measurement by the SH0ES collaboration giving $H_0 = 74.03 \pm 1.42$ km/s/Mpc [7].
- **SN:** Pantheon supernovae dataset consisting of the luminosity distances of 1048 SNe Ia in the redshift range of $0.01 < z < 2.3$ [99].

Note that the `plik lite` likelihood is a foreground and nuisance marginalized version of the full `plik` likelihood [96]. We have found that the two likelihoods return nearly identical posterior distributions with statistically equivalent $\Delta\chi^2$ values for cases of standard EDE as a phenomenological fluid, as well as cases with altered sound speed and nonzero anisotropic stress. Therefore, we use the `plik lite` likelihood in place of the full likelihood for speed in analysis.

We start our analysis of the full phenomenological fluid model by setting our microphysics to match a canonical scalar field model with $c_\phi^2 = 1$ and $A_\sigma = 0$ and obtain constraints on our background model parameters, as well as the six standard Λ CDM parameters $\{\omega_b, \omega_c, \theta_s, \tau, \ln(10^{10} A_s), n_s\}$. This serves as a proof of concept that this phenomenological EDE fluid model can resolve the Hubble tension in an equivalent manner to scalar field EDE models. We then fix the background model parameters, and vary the standard model parameters along with only our added microphysics parameters to directly test the impact of the altered microphysics scenarios. We first set $A_\sigma = 0$ and consider four variations to the gauge-invariant sound speed c_ϕ^2 , outlined in Table 3.1.1. We then incorporate the two shear models presented in Sec. 3.1.2 and parametrize our microphysics via Eqs. (3.11)-(3.12) to derive constraints on our microphysics parameters c_ϕ^2 and A_σ . When considering models with anisotropic shear, we assume the sound speed of the fluid is constant, but allowed to vary from the canonical value of $c_\phi^2 = 1$. The dynamical $c_\phi^2(a)$ model given by Eq. (3.8) is only used in models with no anisotropic shear (i.e. $A_\sigma = 0$). We perform our analysis with a Metropolis-Hasting algorithm with flat priors on all parameters. Our results were

obtained by running eight chains and monitoring convergence via the Gelman-Rubin criterion, with $R - 1 < 0.05$ for all parameters considered complete convergence [100].

Section 3.3

Results

In the following section we explore the implications of this phenomenological EDE fluid model on CMB-derived cosmological parameters. We start by holding the microphysics parameters fixed to their canonical values, and show that our fluid model gives a comparable resolution to the Hubble tension at the background level to standard EDE [72, 73]. Next, we vary only the effective sound speed of the fluid and show that altering c_ϕ^2 alone does not improve the standard EDE solution. We then evaluate our two shear models presented in Sec. 3.1.2 and find that shear model II with $c_\phi^2 \sim 0.55$ and $A_\sigma \sim -0.2$ not only improves the resolution to the Hubble tension provided by standard EDE, but also softens the S_8 tension in comparison to the standard EDE solution, all while providing as comparable a fit to *Planck* 2018 data as the Λ CDM model. Finally, we use Fisher forecasting to determine the power of CMB-S4 [101] to distinguish altered microphysics from the standard EDE case. Extended results can be found in Appendix 3.B.

3.3.1. Resolution to the Hubble tension

Parameter	P18 only		P18+BAO+R19+SN	
	Λ CDM	PFM	Λ CDM	PFM
$100\omega_b$	$2.235(2.237) \pm 0.015$	$2.241(2.248)^{+0.017}_{-0.022}$	$2.252(2.250) \pm 0.013$	$2.287(2.291) \pm 0.022$
ω_c	$0.1202(0.1199) \pm 0.0013$	$0.1227(0.1224)^{+0.0017}_{-0.0029}$	$0.11830(0.11843) \pm 0.00091$	$0.1269(0.1283)^{+0.0031}_{-0.0034}$
$100\theta_s$	$1.04089(1.04105) \pm 0.00032$	$1.04071(1.04081) \pm 0.00034$	$1.04115(1.04106) \pm 0.00028$	$1.04063(1.04061) \pm 0.00035$
τ	$0.0553(0.0551) \pm 0.0076$	$0.0541(0.0573)^{+0.0070}_{-0.0079}$	$0.0608(0.0584)^{+0.0072}_{-0.0081}$	$0.0575(0.0541) \pm 0.0074$
$\ln(10^{10}A_s)$	$3.046(3.045) \pm 0.015$	$3.049(3.056) \pm 0.015$	$3.055(3.051)^{+0.014}_{-0.016}$	$3.065(3.063) \pm 0.015$
n_s	$0.9645(0.9644) \pm 0.0043$	$0.9668(0.9714)^{+0.0046}_{-0.0061}$	$0.9693(0.9685) \pm 0.0038$	$0.9809(0.9844) \pm 0.0065$
$1/n$	-	$< 0.525(0.136)$	-	$< 0.249(0.159)$
r_ϕ	-	$< 0.0222(0.0242)$	-	$0.071(0.090)^{+0.027}_{-0.030}$
$a_t \times 10^4$	-	$4.02(2.78)^{+0.17}_{-1.50}$	-	$3.07(3.12)^{+0.22}_{-0.44}$
H_0 [km/s/Mpc]	$67.27(67.45) \pm 0.56$	$67.90(68.07)^{+0.63}_{-0.91}$	$68.16(68.07) \pm 0.41$	$70.32(70.82) \pm 0.89$
S_8	$0.834(0.829) \pm 0.013$	$0.840(0.841) \pm 0.014$	$0.816(0.817) \pm 0.010$	$0.840(0.841) \pm 0.013$
Total χ^2_{\min}	1014.09	1012.72	2073.37	2063.33
$\Delta\chi^2_{\min}$	-	-1.37	-	-10.04

Table 3.3.1: The mean (best-fit) $\pm 1\sigma$ error of the cosmological parameters for Λ CDM and the PFM with $c_\phi^2 = 1$ and $A_\sigma = 0$ for the P18 dataset and a combined P18+BAO+R19+SN dataset. For the PFM the microphysics parameters are held fixed and constraints are derived on the background model parameters only.

3.3 RESULTS

We begin our analysis by confirming that our phenomenological fluid model can resolve the Hubble tension in the same way as standard EDE. We set the microphysics of our fluid such that it behaves like a canonical scalar field with $c_\phi^2 = 1$ and $A_\sigma = 0$. In order to facilitate convergence of the MCMC chains, we reparametrize our background model and derive constraints on $r_\phi \equiv \rho_\phi(a_t)/\rho_{\Lambda\text{CDM}}(a_t)$, where $\rho_{\Lambda\text{CDM}}(a_t)$ represents the contribution to the energy density of the standard model components at the transition scale factor a_t . Furthermore, instead of varying the sharpness parameter n , we derive constraints on $1/n$ for computational ease. This background parametrization in terms of r_ϕ is distinct from, but analogous to, the effective-fluid approximation given in Ref. [72] where the fractional density is set via $f_{\text{ede}}(z_c) \equiv \Omega_\phi(z_c)/\Omega_{\text{tot}}(z_c)$ with z_c defining the time at which the fluid becomes dynamical. We assume flat priors on all parameters, with $0.1 < 1/n < 1$, $0 < r_\phi < 1$, and $2.49 < a_t \times 10^4 < 9.21$, to keep the transition before recombination. We show parameter constraints for the background model and standard model parameters in Table 3.3.1 for the PFM with a combination of different datasets. The best-fit ΛCDM model is shown for comparison. Posterior distributions for all relevant parameters are shown in Figs. 3.3.1 and 3.3.2.

As can be seen in Table 3.3.1, our phenomenological fluid provides a similar resolution to the Hubble tension as the standard EDE model of Refs. [72, 73], when considering the same datasets. For a combined analysis using the P18+BAO+R19+SN datasets outlined in Sec. 3.2, this fluid model of EDE yields a best-fit value of $H_0 = 70.82$ km/s/Mpc, reducing the Hubble tension with late-universe measurements to $\sim 2\sigma$, while fitting the full suite of data better than ΛCDM with $\Delta\chi_{\text{min}}^2 = -10.4$. We find a preference for a nonzero amount of this EDE fluid at 2σ with $r_\phi = 0.071_{-0.030}^{+0.027}$, peaking at $a_t = 3.07_{-0.44}^{+0.22} \times 10^{-4}$. As expected, the S_8 tension is exacerbated with $S_8 = 0.840 \pm 0.013$. Similarly to scalar field EDE, this appreciable increase in H_0 only occurs when a late-universe prior on the Hubble constant is used in analysis. Consid-

3.3 RESULTS

ering *Planck* 2018 data alone yields $H_0 = 68.07$ km/s/Mpc, in statistical agreement with the best-fit Λ CDM value. Putting this all together, this phenomenological fluid model proves to behave just like a standard EDE model at the background level.

Furthermore, these results show good agreement with the ADE model presented in Ref. [69]. While there is no direct parameter mapping between our two models, our phenomenological fluid EDE model is comparable to the canonical ADE model of Ref. [69], as we consider the same microphysics model with different parametrizations of a phenomenological standard EDE fluid. Our constraints on the full dataset shown in Table 3.3.1 are in good agreement with the cADE constraints given in Table I of Ref. [69]. The variations between our constraints can be explained by slight differences in our models and analysis. Our analysis of our phenomenological fluid EDE model considers an extra parameter, n , when compared to Ref. [69], however we still achieve similar results. Furthermore, we base our analysis on the updated *Planck* 2018 data [4] as opposed to the *Planck* 2015 data [103]. Despite these differences, our results are still statistically comparable to the cADE parametrization, suggesting consistency between our two models.

With these results we have shown that we can mimic the solution to the Hubble tension that scalar field EDE provides without specifying a particular physical model. In order to directly compare the impact of altering the microphysics in this model, we define a baseline case for which the background model parameters are fixed to $n = 6$, $\log(10^{10}\Omega_0) = -3.95$, and $a_t = 3.1 \times 10^{-4}$. For this baseline case, the microphysics parameters are also held fixed at their canonical values of $c_\phi^2 = 1$ and $A_\sigma = 0$. This baseline model gives a 5.7% spike in the energy density right around matter-radiation equality, matching the background evolution of the best-fit $n_{\text{std}} = \infty$ model of Ref. [72]. Parameter constraints for this baseline model are given in Table 3.3.2.

We can now use this phenomenological fluid model to assess the viability of non-

Parameter	PFM - baseline case
$100\omega_b$	$2.263(2.263) \pm 0.015$
ω_c	$0.1261(0.1259) \pm 0.0011$
$100\theta_s$	$1.04059(1.04065) \pm 0.00029$
τ	$0.0542(0.0564) \pm 0.0072$
$\ln(10^{10}A_s)$	$3.057(3.061) \pm 0.014$
n_s	$0.9747(0.9760) \pm 0.0042$
n	6 (fixed)
$\log(10^{10}\Omega_0)$	-3.95 (fixed)
a_t	0.00031 (fixed)
H_0 [km/s/Mpc]	$69.04(69.11) \pm 0.58$
S_8	$0.849(0.849) \pm 0.013$
Total χ^2_{\min}	1013.39
$\Delta\chi^2_{\min}$	-0.70

Table 3.3.2: The mean (best-fit) $\pm 1\sigma$ error of the cosmological parameters for baseline PFM with $c_\phi^2 = 1$ and $A_\sigma = 0$. Constraints are based on the P18 dataset.

scalar field EDE via altered microphysics. Specifically, the presence of anisotropic shear can be used as a diagnostic of any EDE models that arise from anisotropic media, like cosmic strings or cosmic lattice models [84, 87] or coherent vector fields [90], where isotropy is preserved at the background level, but broken in the evolution of linear perturbations. These deviations from the baseline case manifest as changes to the microphysics of our phenomenological fluid, which we discuss in the following sections.

3.3.2. Varying the sound speed

3.3 RESULTS

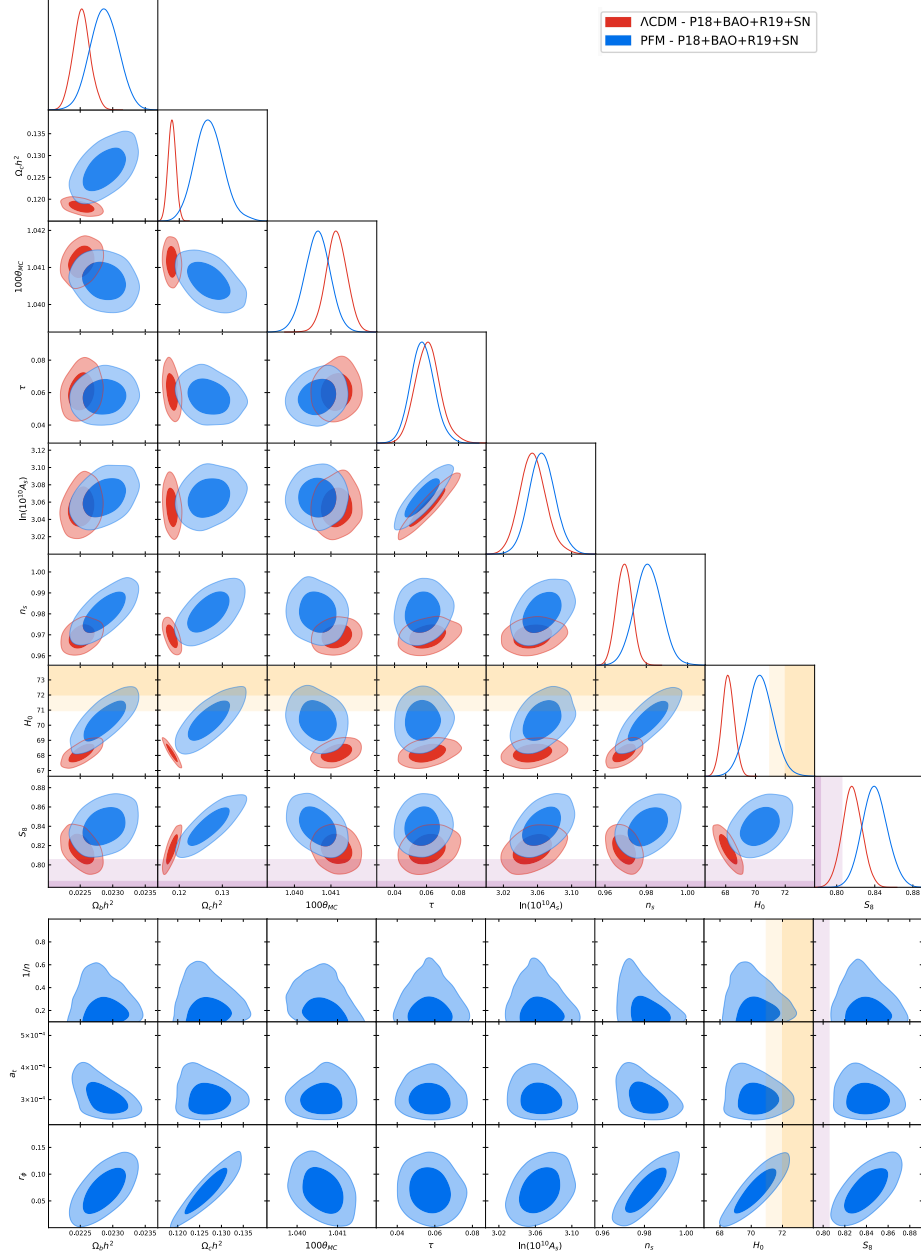


Figure 3.3.1: Top: Posterior distributions of the standard model parameters for the Λ CDM model (red) and the PFM with $c_\phi^2 = 1$ and $A_\sigma = 0$ (blue). Bottom: Posterior distributions of the standard model parameters vs. the background PFM parameters for the PFM with $c_\phi^2 = 1$ and $A_\sigma = 0$. The darker inner (lighter outer) regions correspond to $1\sigma(2\sigma)$ confidence intervals. The SH0ES collaboration measurement of $H_0 = 73.04 \pm 1.04$ km/s/Mpc and the KiDS-1000 weak lensing survey measurement of $S_8 = 0.759^{+0.024}_{-0.021}$ are shown in the orange and purple bands, respectively [8, 102]. Distributions are generated with the P18+BAO+R19+SN datasets.

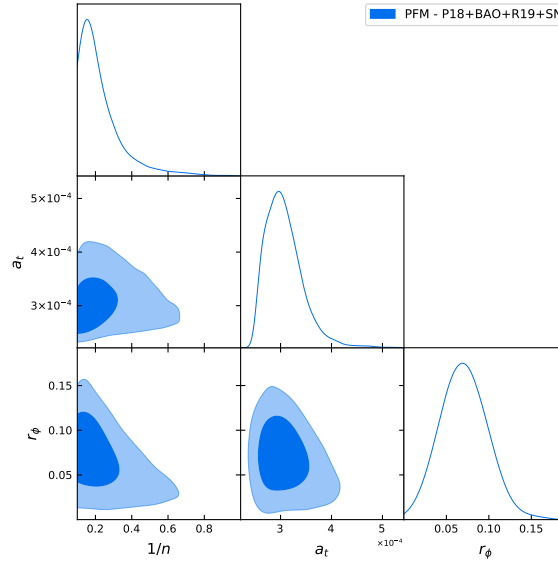


Figure 3.3.2: Posterior distributions of the background PFM parameters for the PFM with $c_\phi^2 = 1$ and $A_\sigma = 0$. The darker inner (lighter outer) regions correspond to $1\sigma(2\sigma)$ confidence intervals. Distributions are generated with the P18+BAO+R19+SN datasets.

Parameter	PFM - case 1	PFM - case 2	PFM - case 3	PFM - case 4
$100\omega_b$	$2.185(2.176) \pm 0.014$	$2.274(2.280) \pm 0.015$	$2.184(2.182) \pm 0.014$	$2.263(2.266) \pm 0.015$
ω_c	$0.1111(0.1117) \pm 0.0014$	$0.1163(0.1160) \pm 0.0013$	$0.1112(0.1114) \pm 0.0014$	$0.1261(0.1264) \pm 0.0012$
$100\theta_s$	$1.03974(1.03966) \pm 0.00030$	$1.04081(1.04082) \pm 0.00031$	$1.03975(1.03966) \pm 0.00030$	$1.04059(1.04063) \pm 0.00030$
τ	$0.0642(0.0622)^{+0.0072}_{-0.0093}$	$0.0641(0.0650)^{+0.0074}_{-0.0091}$	$0.0636(0.0619) \pm 0.0082$	$0.0541(0.0528) \pm 0.0077$
$\ln(10^{10}A_s)$	$3.053(3.049)^{+0.014}_{-0.018}$	$3.070(3.071)^{+0.014}_{-0.017}$	$3.051(3.047) \pm 0.016$	$3.057(3.056) \pm 0.015$
n_s	$0.9617(0.9602) \pm 0.0042$	$0.9707(0.9713) \pm 0.0044$	$0.9615(0.9613) \pm 0.0041$	$0.9746(0.9733) \pm 0.0043$
$a_{c_\phi} \times 10^4$	-	3.1 (fixed)	0.3 (fixed)	30 (fixed)
H_0 [km/s/Mpc]	$74.39(73.97) \pm 0.79$	$73.27(73.45) \pm 0.73$	$74.34(74.13) \pm 0.80$	$69.02(68.96) \pm 0.60$
S_8	$0.743(0.749) \pm 0.014$	$0.752(0.749) \pm 0.013$	$0.742(0.744) \pm 0.015$	$0.849(0.850) \pm 0.013$
Total χ^2_{\min}	1326.47	1087.30	1323.68	1013.28
$\Delta\chi^2_{\min}$	+312.38	+73.21	+309.59	-0.81

Table 3.3.3: The mean (best-fit) $\pm 1\sigma$ error of the cosmological parameters for cases 1-4 of our PFM model with varied sound speeds, outlined in Table 3.3.5. The background model is fixed for all cases to $n = 6$, $\log(10^{10}\Omega_0) = -3.95$, and $a_t = 3.1 \times 10^{-4}$ for direct comparison to the baseline case. All cases considered have no added anisotropic shear. Constraints are based on the P18 dataset.

We have shown that a phenomenological fluid model can solve the Hubble tension in the most minimal microphysics scenario with a canonical sound speed of $c_\phi^2 = 1$ and no anisotropic shear. Before including anisotropic shear in our microphysics scenario, we investigate how changing only the effective sound speed of the fluid alters cosmological parameter estimation, while holding $A_\sigma = 0$. The background model parameters are fixed to $n = 6$, $\log(10^{10}\Omega_0) = -3.95$, and $a_t = 3.1 \times 10^{-4}$ for ease in comparison to the baseline case. We then vary the sound speed from its baseline value of $c_\phi^2 = 1$, considering the four alternative cases, each with no added anisotropic shear, outlined in Table 3.1.1. We consider two cases for comparison. The first is Λ CDM, used as a control. The second is the baseline model, used for direct comparison of the altered microphysics.

The results of the MCMC analysis, consisting of constraints on cosmological parameters for cases 1-4 are presented in Table 3.3.3. We show the posterior distributions for the relevant parameters in these models in Fig. 3.3.3. We restrict our dataset to only include *Planck* 2018 data to focus on the CMB inference of H_0 within this phenomenological fluid. We present results for extended datasets in Appendix 3.B.

We can see from Table 3.3.3 that setting $c_\phi^2 = 0$ in case 1 gives values of H_0 and S_8 that are in better agreement with local measurements than the baseline model. For case 1, the Hubble tension is reduced even further from the baseline model to $< 1\sigma$, with a best-fit value of $H_0 = 73.97$ km/s/Mpc, compared with the SH0ES Collaboration measurement of $H_0 = 73.2 \pm 1.3$ km/s/Mpc, shown by the orange bands in Fig. 3.3.3 [7]. Case 1 also offers a complete resolution to the S_8 tension, with a best-fit value of $S_8 = 0.749$, compared to the measurement from the KiDS-1000 weak lensing survey of $S_8 = 0.759^{+0.024}_{-0.021}$, shown by the purple bands in Fig. 3.3.3 [102]. While the cosmological parameter estimation may be favorable in case 1, the fit to the data is significantly degraded, with a $\Delta\chi^2_{\min} = 312.38$ compared to the Λ CDM

model.

To better understand the effect of setting $c_\phi^2 = 0$ in case 1, we take a closer look at the fluid perturbations equations of motion. Whenever $c_\phi^2 = 0$, the pressure perturbation simplifies to

$$\delta p_\phi = -3\mathcal{H}(\rho_\phi + p_\phi) \left[w_\phi - \frac{w'_\phi}{3\mathcal{H}(1 + w_\phi)} \right] \theta_\phi / k^2. \quad (3.13)$$

Using this to simplify Eq. (3.7) we can see that

$$\theta'_\phi = -\mathcal{H}\theta_\phi, \quad (3.14)$$

meaning that with adiabatic initial conditions, where $\theta_{\text{init}} = 0$, the velocity divergence of our fluid is always zero. With $\theta_\phi = 0$, we can see from Eq. (3.13) that $\delta p_\phi = 0$, meaning that this fluid clusters. By the same logic, Eq. (3.6) simplifies to

$$\delta'_\phi = -(1 + w_\phi) \frac{h'}{2} + 3\mathcal{H}w_\phi\delta_\phi, \quad (3.15)$$

where we see that when $c_\phi^2 = 0$, there is nothing to damp the growth of density perturbations of our phenomenological fluid. This can be seen in Fig. 3.3.4, where we show the evolution of the density perturbations of all relevant components as a function of scale factor. Compared to the baseline model shown in gray, the density perturbation of the EDE fluid in case 1, shown in black, is non-negligible at late times, dominating over the radiation components at late times, and over the baryonic contribution for a brief period when the background fluid density first spikes.

This addition of a clustering fluid component deepens the gravitational potentials and decreases power over the first acoustic peak. The cold dark matter (CDM) and baryon densities in this model must be lowered to account for this additional

clustering component as seen in Fig. 3.3.3. The change in $\Omega_c h^2$ is also why we see a slightly higher H_0 in case 1 than in the baseline model; a lower CDM density shifts the acoustic peaks towards low ℓ , so to maintain the correct angular scales in the CMB anisotropy pattern, H_0 must be raised even more, as seen in Table 3.3.3. It is important to note that the decrease we see in the S_8 parameter in case 1 is mostly driven by the change in the matter density since $S_8 = \sigma_8 \sqrt{\Omega_m/0.3}$, where σ_8 gives the amplitude of matter fluctuations. With a lower matter density, the structure growth parameter S_8 is decreased while keeping the actual amplitude of fluctuations σ_8 effectively fixed. Case 1 gives $\sigma_8 = 0.8284^{+0.0062}_{-0.0072}$, in good agreement with the baseline constraint of $\sigma_8 = 0.8305 \pm 0.0060$.

This description of the $c_\phi^2 = 0$ model offers insight on the dynamical sound speed model as well. From the constraints presented in Table 3.3.3, we can see that the baseline case with $c_\phi^2 = 1$ and case 4 are virtually indistinguishable. In case 4, the sound speed does not begin the transition from $c_\phi^2 = 1$ to $c_\phi^2 = 0$ until after the equation of state has transitioned to $w_\phi = 1$. With virtually no change in the fit to the data from the baseline case, this suggests that once the background fluid density begins to redshift away, the sound speed has little impact. Alternatively, in case 3, $c_\phi^2 = 0$ well before the fluid becomes dynamical and relevant. As such, the parameter constraints and fit to the data are similar to those for case 1, where $c_\phi^2 = 0$ always. Case 2 lies in the middle with the transition in the sound speed and equation of state happening simultaneously. In this case, we see the fit to the data begins to degrade and the best-fit parameters shift towards their case 1 values. Looking at the evolution of the density perturbations in each of these cases makes these parameter constraints clear. In Fig. 3.3.4, we see that $\delta\rho_\phi$ in cases 2 and 3 both dominate over the contribution from baryons and radiation for a brief period, resulting in the same changes to the gravitational potentials that cause the poor fit to the data in case 1.

3.3 RESULTS

However, $\delta\rho_\phi$ in case 4 only begins to grow once the background density of the fluid is negligible so we do not see the same domination at late times.

These constraints tell a simple story: the earlier that $c_\phi^2 = 0$, the longer the fluid clusters and the growth of density perturbations are left unchecked, resulting in a worse fit to the data. After the fluid starts redshifting away, the low background density keeps the sound speed from leaving too strong an imprint. Hence, dynamical $c_\phi(a)$ models with $a_{c_\phi} > a_t$ are effectively the same as the baseline model, and models with $a_{c_\phi} < a_t$ are effectively the same as the $c_\phi^2 = 0$ model. As the sound speed can only take values of $0 \leq c_\phi^2 \leq 1$, setting $c_\phi^2 = 0$ represents the maximally different case of those we consider here.

Putting all of these constraints together, it seems that altering the sound speed of EDE from its canonical value of $c_\phi^2 = 1$ without jointly altering the background dynamics of the fluid, as suggested in Refs. [69, 72], is not preferred by *Planck* 2018 data, despite providing preferable constraints on the Hubble constant and structure growth parameter.

3.3.3. Shear model I

We have shown that only changing the sound speed of our phenomenological EDE fluid cannot improve the solution to the Hubble tension. We now move on to including anisotropic shear in our model, starting with shear model I, given by Eq. (3.9). We hold the background model fixed at $n = 6$, $\log(10^{10}\Omega_0) = -3.95$, and $a_t = 3.1 \times 10^{-4}$ to facilitate direct comparison to the baseline case, and vary c_\perp^2 and c_\parallel^2 alongside our six Λ CDM parameters to derive constraints on c_ϕ^2 and A_σ . Parameter constraints for this shear model are presented in Table 3.3.4. Posterior distributions for relevant parameters in this model, along with shear model II, are presented in Fig. 3.3.5–3.3.6, with Λ CDM and baseline posteriors included for comparison.

As we can see from Table 3.3.4, the best-fit microphysics parameters for this shear

Parameter	PFM w/ shear I
$100\omega_b$	$2.256(2.225) \pm 0.016$
ω_c	$0.1261(0.1262) \pm 0.0013$
$100\theta_s$	$1.04062(1.04043) \pm 0.00033$
τ	$0.0541(0.0531) \pm 0.0073$
$\ln(10^{10}A_s)$	$3.058(3.056) \pm 0.014$
n_s	$0.9737(0.9727) \pm 0.0044$
c_ϕ^2	$0.770(0.848)^{+0.150}_{-0.097}$
A_σ	$-0.068(-0.031)^{+0.063}_{-0.070}$
H_0 [km/s/Mpc]	$68.97(68.83) \pm 0.62$
S_8	$0.850(0.850) \pm 0.013$
Total χ^2_{\min}	1013.31
$\Delta\chi^2_{\min}$	-0.78

Table 3.3.4: The mean (best-fit) $\pm 1\sigma$ error of the cosmological parameters for phenomenological fluid model with shear model I. The background model parameters are held fixed at $n = 6$, $\log(10^{10}\Omega_0) = -3.95$, and $a_t = 3.1 \times 10^{-4}$. Constraints are derived from the P18 dataset and $\Delta\chi^2_{\min}$ is calculated with respect to the best-fit Λ CDM model presented in Table 3.3.1.

model make it virtually indistinguishable from the baseline case with $c_\phi^2 = 0.848$ and $A_\sigma = -0.031$. To get a clear picture as to why this model of anisotropic shear is so disfavored by data, it is useful to take a closer look at how the addition of this shear changes the CMB angular power spectrum via its interactions with the other perturbative quantities of the EDE fluid.

The magnitude and sign of the EDE shear is controlled via A_σ . The total shear in the cosmic fluid π_{tot} , is given by the sum of all nonzero shear components $\pi_{tot} = \Sigma_i(1 + w_i)\sigma_i$. Besides our EDE component, the only other shear contributions come from radiation for which $\sigma_\gamma, \sigma_\nu < 0$. This means that for a model with $A_\sigma = 0$, $\pi_{tot} < 0$. When $(1 + w_\phi)\sigma_\phi > 0$, due to a positive A_σ , the EDE shear adds destructively to the total shear in the system, lowering the magnitude of π_{tot} . Conversely, when $(1 + w_\phi)\sigma_\phi < 0$, due to a negative A_σ , the EDE shear enhances the total shear in the system, increasing the magnitude of π_{tot} . These changes to the total shear contribution compared to the baseline model have a significant impact on the Weyl

potential Φ , given by

$$\Phi = -\frac{8\pi G}{2k^2} a^2 \sum_i \rho_i \left[\delta_i + 3\mathcal{H}(1 + w_i)\theta_i/k^2 + \frac{3}{2}(1 + w_i)\sigma_i \right], \quad (3.16)$$

where i sums over all components of the total energy density. Hence, when we increase or decrease the magnitude of the total shear contribution, the gravitational potentials get deeper or shallower, respectively.

In addition to the inherent impact of adding a new component to the total shear, σ_ϕ influences the evolution of the velocity perturbation of the EDE via Eq. (3.7), which in turn alters the evolution of the density perturbation. At large scales, we can analytically solve for the scaling behavior of these perturbations which we parametrize via an effective equation of state such that $\delta_\phi \propto a^{-3(1+w_\delta)}$ and $\theta_\phi \propto a^{-3(1+w_\theta)}$. During matter domination we find that

$$w_\delta = -\frac{1}{4} \left(5 - 2A_\sigma + \sqrt{9 + 4A_\sigma(A_\sigma - 1) - 8c_\phi^2} \right), \quad (3.17)$$

$$w_\theta = -\frac{1}{12} \left(17 - 6A_\sigma + 3\sqrt{9 + 4A_\sigma(A_\sigma - 1) - 8c_\phi^2} \right), \quad (3.18)$$

which tell us that as you increase A_σ , both δ_ϕ and θ_ϕ decay more rapidly, regardless of the background equation of state of the fluid.

For very positive A_σ , the density and velocity perturbations decay quicker than the baseline $A_\sigma = 0$ case, causing the overall magnitude of the Weyl potential to be decreased, and vice versa for negative A_σ cases. The overall changes to the Weyl potential due to the inherent impact of σ_ϕ and the subsequent impact on δ_ϕ and θ_ϕ can be seen in Fig. 3.3.7 where we plot the evolution of the Weyl potential at low- k for different manifestations of shear model I. We can see that for very positive A_σ , shown in blue, the gravitational potentials are shallower than the baseline model, shown in black, for the brief period following the transition in the background equation of

state when the EDE fluid has a non-negligible background abundance. Due to the rapid scaling of the perturbations and the background behavior of the fluid density, this suppression of the Weyl potential is short lived, and the gravitational potentials return to their baseline trajectory at late times. When $A_\sigma < 0$, we see the opposite behavior. The Weyl potential is deepened, and because δ_ϕ and θ_ϕ do not decay as quickly as they do in the baseline model, their effect lasts longer. When $A_\sigma \lesssim -0.6$, the fluid perturbations dominate over the standard model components, causing the Weyl potential to diverge from its baseline trajectory as seen through the green curve in Fig. 3.3.7.

For fixed c_ϕ^2 and A_σ , this behavior at large scales leads to large changes at $\ell \lesssim 1000$ in the CMB angular power spectrum as seen in Fig. 3.3.8 where we plot the residuals between the best-fit Λ CDM model and shear model I, for choices of positive and negative A_σ . We can see that for $A_\sigma = -0.6$, shown in red, the divergence of the Weyl potential suppresses power over the first acoustic peak and enhances power at $\ell \lesssim 100$, when compared to the baseline model. These large changes to the power spectrum for non-negligible amounts of shear explain the best-fit parameters for shear model I presented in Table 3.3.4. *Planck* 2018 data constrains the amount of shear allowed in this model to be very close to zero with $A_\sigma = -0.068^{+0.063}_{-0.070}$, suggesting that the large-scale influence of this equation-of-state formulation of shear on gravitational potentials is too large an obstacle to overcome. Putting this all together, if EDE has some anisotropic shear component, the data suggests it should not be introduced in the form of Eq. (3.9) due to the large-scale influence of the shear on the evolution of gravitational potentials.

3.3.4. Shear model II

3.3 RESULTS

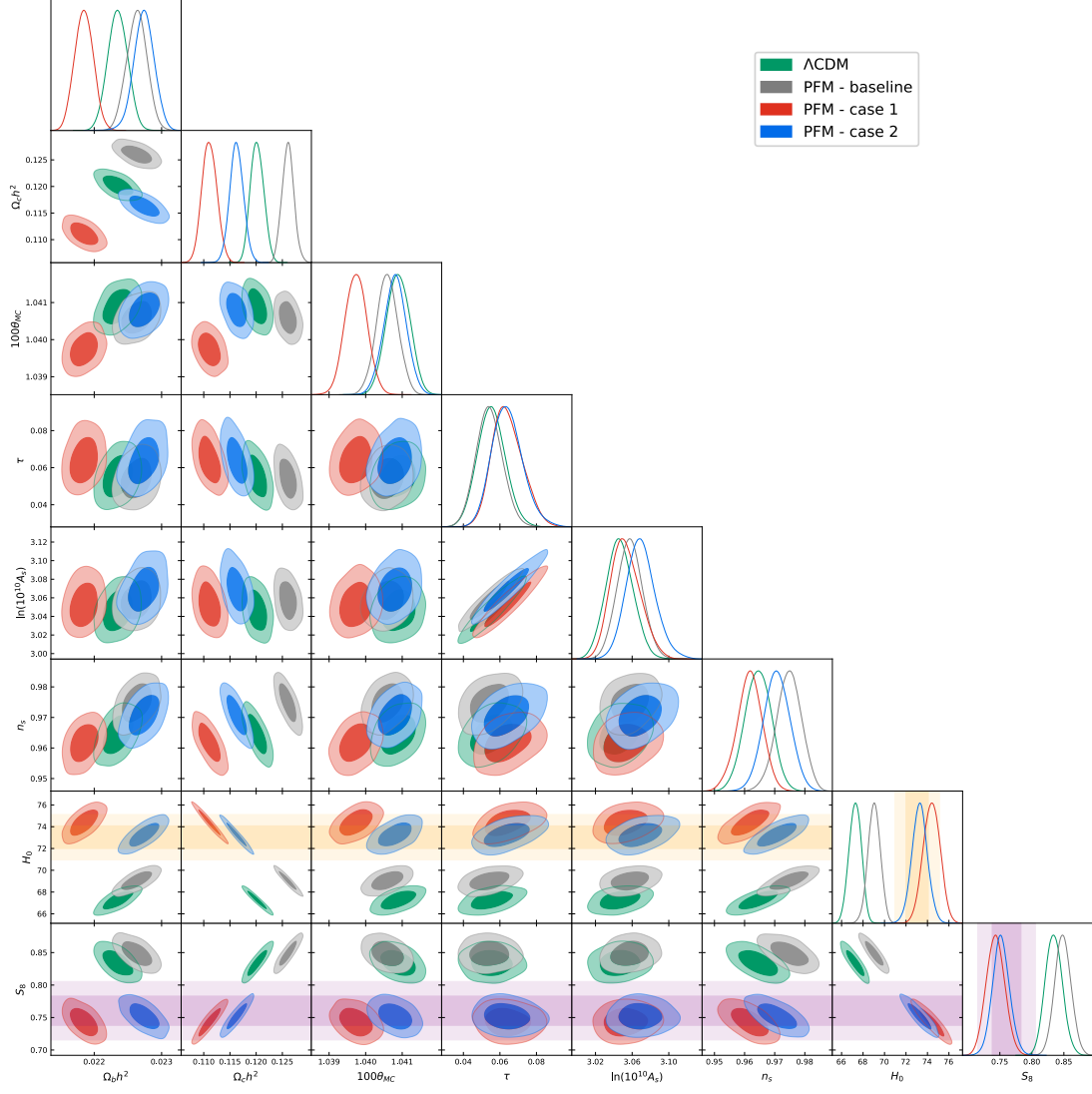


Figure 3.3.3: Posterior distributions for the standard model parameters in the PFM with noncanonical sound speeds. For all PFM cases, the background model parameters are set to $n = 6$, $\log(10^{10}\Omega_0) = -3.95$, and $a_t = 3.1 \times 10^{-4}$, and there is no anisotropic shear ($A_\sigma = 0$). In red we show case 1 for which there is a constant sound speed set to $c_\phi^2 = 0$. In blue we show case 2 for which the sound speed is dynamical, given by Eq. (3.8), and $a_{c_\phi} = a_t$. Posteriors for the Λ CDM and baseline PFM are shown in green and gray, respectively, for comparison. The darker inner (lighter outer) regions correspond to 1σ (2σ) confidence intervals. The SH0ES Collaboration measurement of $H_0 = 73.04 \pm 1.04$ km/s/Mpc and the KiDS-1000 weak lensing survey measurement of $S_8 = 0.759^{+0.024}_{-0.021}$ are shown in the orange and purple bands, respectively [8, 102]. Distributions are generated with the P18 dataset.

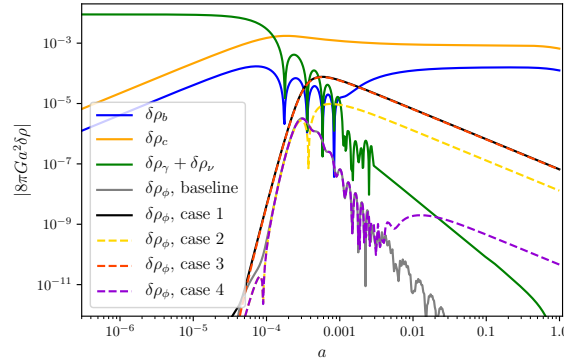


Figure 3.3.4: The evolution of the density perturbation of all relevant components as a function of scale factor for the $k = 0.1 \text{ Mpc}^{-1}$ wave mode. These curves are generated from a shear-less model with $n = 6$, $\log(10^{10}\Omega_0) = -3.95$, and $a_t = 3.1 \times 10^{-4}$ with the standard model parameters set to their Λ CDM best-fit values. The density perturbation of our phenomenological fluid $\delta\rho_\phi$ is shown in case 1 (black) and the baseline model (gray) for comparison. Setting $c_\phi^2 = 0$ results in the unhindered growth of density fluctuations at later times as seen by the black curve.

3.3 RESULTS

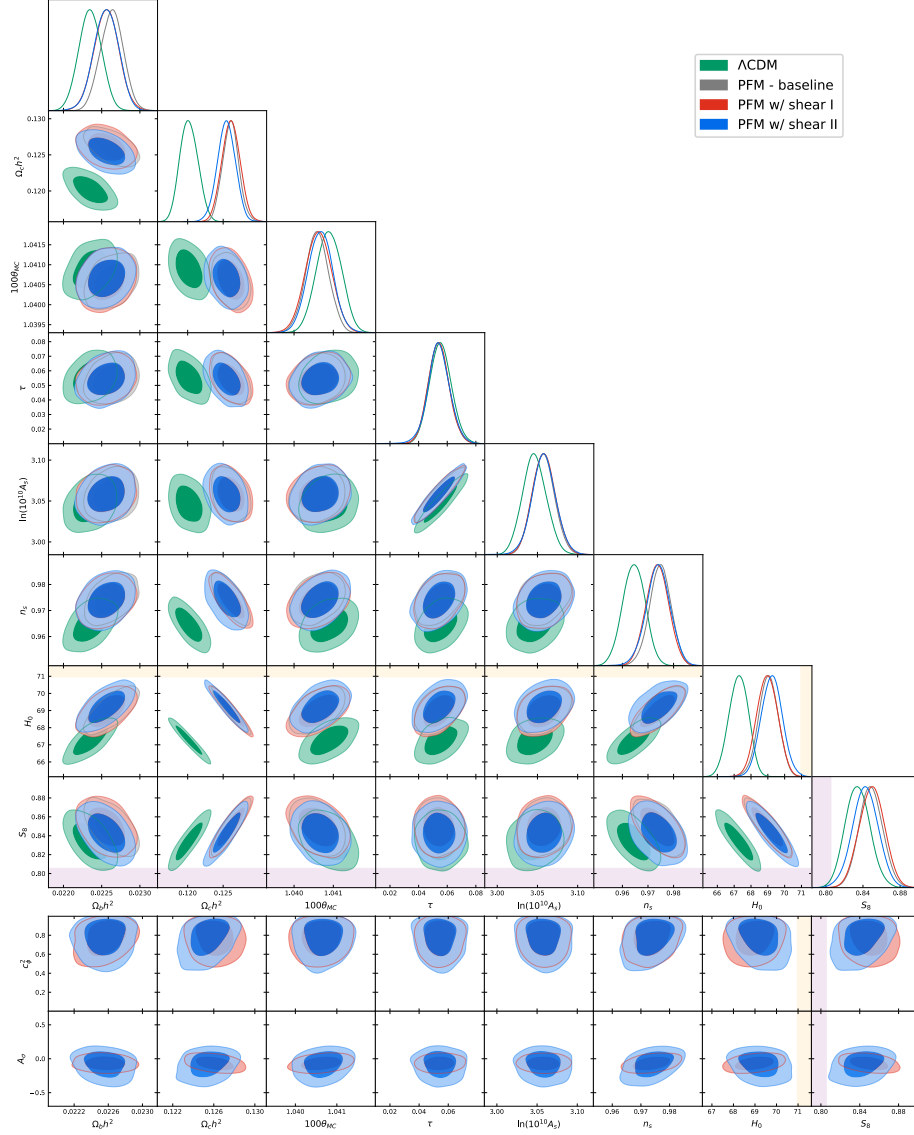


Figure 3.3.5: Top: Posterior distributions of the standard model parameters for the PFM with shear model I (red) and shear model II (blue) with $n = 6$, $\log(10^{10}\Omega_0) = -3.95$, and $a_t = 3.1 \times 10^{-4}$. Posteriors for the Λ CDM model (green) and the baseline PFM (gray) are shown for comparison. Bottom: Posterior distributions of the standard model parameters vs the microphysics parameters for the PFM with shear model I (red) and shear model II (blue) with $n = 6$, $\log(10^{10}\Omega_0) = -3.95$, and $a_t = 3.1 \times 10^{-4}$. The darker inner (lighter outer) regions correspond to $1\sigma(2\sigma)$ confidence intervals. The SH0ES Collaboration measurement of $H_0 = 73.04 \pm 1.04$ km/s/Mpc and the KiDS-1000 weak lensing survey measurement of $S_8 = 0.759^{+0.024}_{-0.021}$ are shown in the orange and purple bands, respectively [8, 102]. Distributions are generated with the P18 dataset. Both shear models converged to a negligible amount of added shear, with c_ϕ^2 very nearly equal to unity, making them virtually indistinguishable from the baseline model.

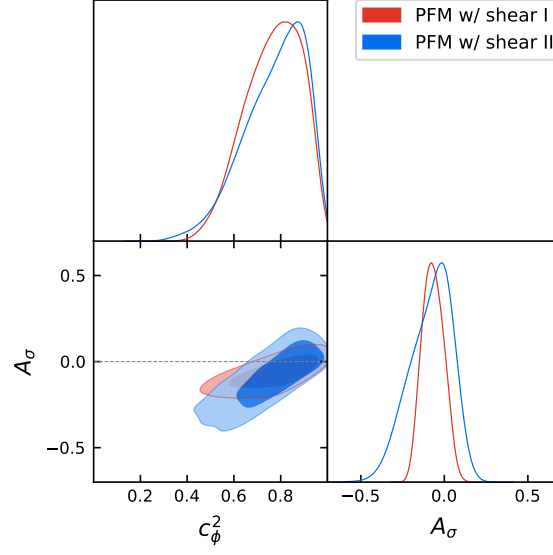


Figure 3.3.6: Posterior distributions for the microphysics parameters c_ϕ^2 and A_σ in the PFM model with shear model I (red) and shear model II (blue) with $n = 6$, $\log(10^{10}\Omega_0) = -3.95$, and $a_t = 3.1 \times 10^{-4}$. The darker inner (lighter outer) regions correspond to $1\sigma(2\sigma)$ confidence intervals. In both cases, the posterior distributions favor $A_\sigma = 0$, with a slight preference for negative A_σ , particularly in shear model II. Distributions are generated with the P18 dataset.

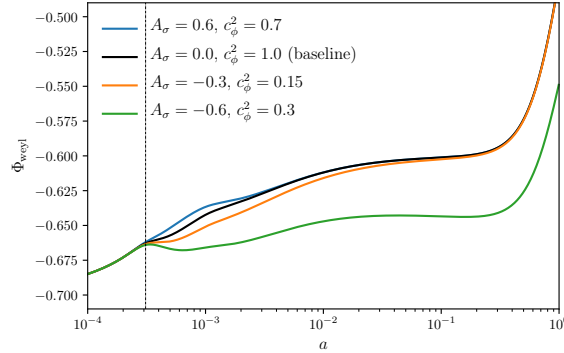


Figure 3.3.7: Evolution of the Weyl gravitational potential as a function of scale factor for the $k = 7 \times 10^{-6} \text{ Mpc}^{-1}$ wave mode in shear model I. The black curve shows the baseline model with no added shear. The blue (orange) curves show that a case with positive (negative) A_σ makes the potential wells shallower (deeper) for the brief period of time that the background density of the EDE fluid is relevant. The green curve shows that for a very anisotropic fluid ($A_\sigma < -0.6$), the Weyl potential diverges from its baseline evolution. The black-dashed line shows the transition scale factor a_t , at which the fluid becomes dynamical.

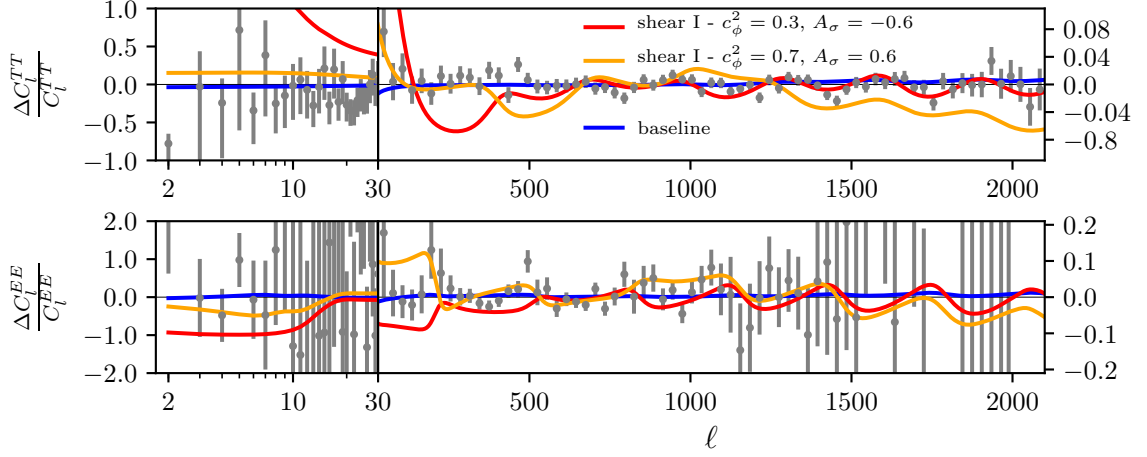


Figure 3.3.8: Temperature and polarization power spectrum residuals between the best-fit Λ CDM model and the best-fit fluid model with shear model I with positive (orange) and negative (red) A_{σ} . The best-fit baseline model is shown in blue for comparison. Residuals from *Planck* 2018 data are shown in gray. Left (right) vertical axis scaling is for multipoles less (greater) than $\ell = 30$.

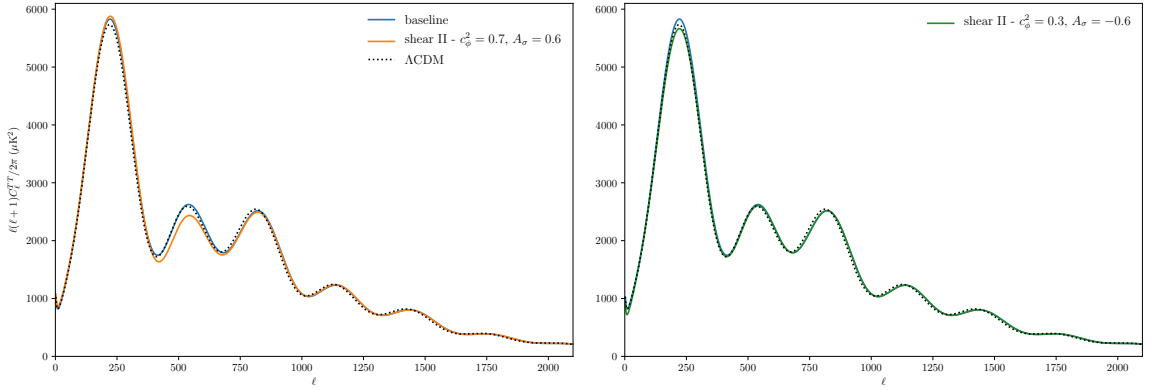


Figure 3.3.9: Temperature power spectrum for shear model II. All curves are generated with the standard model parameters set to their best-fit Λ CDM values from Table 3.3.1. For the PFM models we set $n = 6$, $a_t = 3.1 \times 10^{-4}$, and $\log(10^{10}\Omega_0) = -3.95$. The blue curves shows the baseline model with $c_{\phi}^2 = 1$, and $A_{\sigma} = 0$, the orange curve shows shear model II with a fixed positive A_{σ} , and the green curve shows shear model II with a fixed negative A_{σ} .

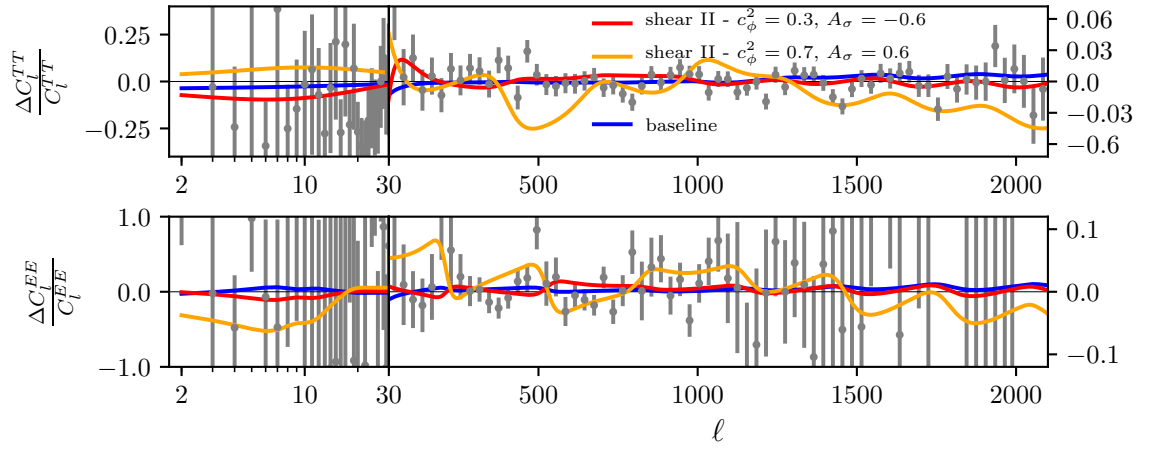


Figure 3.3.10: Temperature and polarization power spectrum residuals between the best-fit Λ CDM model and the best-fit fluid model with shear model II with positive (orange) and negative (red) A_σ . The best-fit baseline model is shown in blue for comparison. Residuals from *Planck* 2018 data are shown in gray. Left (right) vertical axis scaling is for multipoles less (greater) than $\ell = 30$.

Parameter	PFM w/ shear II	shear II - $A_\sigma = 0.6$	shear II - $A_\sigma = -0.6$	shear II - $A_\sigma = -0.2$
$100\omega_b$	$2.256(2.257) \pm 0.016$	$2.069(2.070) \pm 0.012$	$2.275(2.269) \pm 0.016$	$2.250(2.250) \pm 0.015$
ω_c	$0.1255(0.1257) \pm 0.0013$	$0.1260(0.1259) \pm 0.0011$	$0.1245(0.1247) \pm 0.0012$	$0.1245(0.1248) \pm 0.0012$
$100\theta_s$	$1.04067(1.04059) \pm 0.00031$	$1.04007(1.04009) \pm 0.00032$	$1.04026(1.04032) \pm 0.00030$	$1.04067(1.04065) \pm 0.00030$
τ	$0.0541(0.0569) \pm 0.0078$	$0.0391(0.0419)^{+0.0089}_{-0.0072}$	$0.0546(0.0528) \pm 0.0075$	$0.0550(0.0562) \pm 0.0074$
$\ln(10^{10}A_s)$	$3.058(3.060) \pm 0.015$	$3.035(3.039)^{+0.017}_{-0.014}$	$3.063(3.062) \pm 0.014$	$3.060(3.063) \pm 0.014$
n_s	$0.9740(0.9772) \pm 0.0047$	$0.9591(0.9603) \pm 0.0038$	$0.9618(0.9602) \pm 0.0041$	$0.9723(0.9715) \pm 0.0042$
c_ϕ^2	$0.778(0.951)^{+0.170}_{-0.087}$	0.7 (fixed)	0.3 (fixed)	0.55 (fixed)
A_σ	$-0.08(0.08)^{+0.15}_{-0.10}$	0.6 (fixed)	-0.6 (fixed)	-0.2 (fixed)
H_0 [km/s/Mpc]	$69.24(69.11) \pm 0.62$	$67.07(67.13) \pm 0.53$	$69.64(69.52) \pm 0.61$	$69.56(69.41) \pm 0.60$
S_8	$0.843(0.847) \pm 0.014$	$0.863(0.864) \pm 0.012$	$0.830(0.8311) \pm 0.013$	$0.833(0.838) \pm 0.013$
Total χ^2_{\min}	1013.48	1355.69	1031.73	1016.50
$\Delta\chi^2_{\min}$	-0.61	341.60	17.64	2.41

Table 3.3.5: The mean (best-fit) $\pm 1\sigma$ error of the cosmological parameters for phenomenological fluid model with shear model shear model II with $n = 6$, $\log(10^{10}\Omega_0) = -3.95$, $a_t = 3.1 \times 10^{-4}$, and different choices of c_ϕ^2 and A_σ . Constraints are derived from the P18 dataset and $\Delta\chi^2_{\min}$ is calculated with respect to the best-fit Λ CDM model presented in Table 3.3.1. The best-fit values for the $A_\sigma = 0.6$ and $A_\sigma = -0.6$ cases were used to generate the orange and red curves in Fig. 3.3.8, respectively.

Our second shear model is defined via a physically motivated [82], gauge-invariant equation of motion given by Eq. (3.10). Similarly to shear model I, the best-fit parameters for shear model II with free c_ϕ^2 and A_σ , given in Table 3.3.5, are statistically indistinguishable from the best-fit baseline model, given in Table 3.3.2. However, as can be seen by the blue curve in Fig. 3.3.6, the 1σ constraints on the microphysics parameters are much looser in shear model II than they are in shear model I. Specifically, a degeneracy between c_ϕ^2 and A_σ exists allowing a non-negligible amount of negative shear coupled with a lower effective sound speed.

These constraints are made clearer by looking at the effect of positive and negative A_σ values on the CMB angular power spectrum. Figure 3.3.9 shows the temperature power spectrum for cases with very positive $A_\sigma = 0.6$ (orange) and very negative $A_\sigma = -0.6$ (green), with the baseline case and the best-fit Λ CDM model shown in blue, and black, respectively, for comparison. We show parameter constraints for shear model II with the same positive and negative A_σ in Table 3.3.5.

In the baseline case, which mimics standard EDE, power is enhanced over the first acoustic peak and all peaks are shifted towards large scales. These changes to the power spectrum result in the parameter shifts seen in the best-fit baseline model shown in Table 3.3.2, most notably, increased ω_c and H_0 values. On top of the changes to the power spectrum we see in the baseline case, when A_σ is positive, we see an added suppression of power over the second acoustic peak. This suppression requires a higher value of ω_b as seen in Table 3.3.5, restoring the heights of the first and second acoustic peaks into agreement with *Planck* 2018 data, in conjunction with changes to the CDM density. The key difference between this model and the baseline case is that the requirement of a higher baryon density also shifts the acoustic peaks towards larger scales, relinquishing the need for a higher value of the Hubble constant, resulting in a best-fit value of $H_0 = 67.13$ km/s/Mpc, virtually unchanged from the

best-fit Λ CDM value. Overall, these parameter changes lead to a poor fit to the data seen through the residuals between this positive A_σ case and the best-fit Λ CDM model shown by the orange curve in Fig. 3.3.10.

Turning to a negative shear case, we get a different story. From Fig. 3.3.6 we know that *Planck* 2018 data allows for a non-negligible, but not large, amount of negative shear. For explanatory purposes we focus on an extremal case with $A_\sigma = -0.6$ and $c_\phi^2 = 0.3$ to show the full effect of a negative shear in this model. From Fig. 3.3.9, we can see that when we add in this negative shear, leaving all Λ CDM parameters unchanged from their best-fit values, the enhancement over the first acoustic peak that comes in the baseline model is avoided, giving a temperature power spectrum whose main difference from the Λ CDM model is a shift in all acoustic peaks towards small scales. As can be seen in Table 3.3.5, this leads to an even higher Hubble constant than the baseline case with $H_0 = 69.64 \pm 0.61$ km/s/Mpc. Similarly to the baseline case, the CDM density must be increased from its Λ CDM value, but in this model the added shear counteracts the deepening of the gravitational potentials caused by the increase in the matter density, leaving the S_8 value in statistical agreement with Λ CDM giving $S_8 = 0.830 \pm 0.013$. So, in addition to strengthening the solution to the H_0 tension, this model does not exacerbate the S_8 tension like standard EDE models. As can be seen in Fig. 3.3.10, the best-fit model with $A_\sigma = -0.6$ results in a slightly poorer fit to *Planck* 2018 data than the baseline case with a $\Delta\chi_{\min}^2 = 17.64$, as is to be expected for this extremal case.

For a more reasonable choice of $c_\phi^2 = 0.55$ and $A_\sigma = -0.2$, which lies within the 2σ contours in Fig. 3.3.6, we see the same shifts in H_0 and S_8 as we do in the extremal case, shown in Fig. 3.4.1, but with a comparable fit to the data as Λ CDM. From these results we see that the addition of a negative shear that evolves according to the equation of motion given in Eq. (3.10) strengthens EDE as a solution to the

Hubble tension. In this case, the S_8 tension is not exacerbated by the inclusion of our new component while preserving the solution to the Hubble tension.

This can be seen more clearly in comparison with local measurements of S_8 and H_0 . Comparing our S_8 constraints to the combined DES-Y3 constraint of $S_8 = 0.776 \pm 0.017$ [6], we find that our baseline EDE model with a best-fit $S_8 = 0.849$ gives a $\chi^2_{\text{DES}} = 18.44$, whereas shear model II with $A_\sigma = -0.2$ gives $\chi^2_{\text{DES}} = 13.30$ with its best-fit value of $S_8 = 0.838$. Compared with the Λ CDM model best-fit value of $S_8 = 0.829$ and $\chi^2_{\text{DES}} = 9.72$, our negative shear model offers a significant improvement over standard EDE.

Similarly, as a resolution to the Hubble tension, we see a slightly better fit with our negative shear model to the SH0ES Collaboration measurement of $H_0 = 73.04 \pm 1.04$ km/s/Mpc [8] which for Λ CDM leads to a $\chi^2_{\text{SH0ES}} = 28.89$. The baseline EDE model softens this tension with a best-fit $H_0 = 69.11$ km/s/Mpc leading to a $\chi^2_{\text{SH0ES}} = 14.28$. Shear model II with $A_\sigma = -0.2$ improves on this slightly with $H_0 = 69.41$ km/s/Mpc giving $\chi^2_{\text{SH0ES}} = 12.18$, a slight, but statistically irrelevant, improvement to the resolution given by the baseline EDE model.

We have also considered the case where the background parameters, r_ϕ , a_t , and n , are allowed to vary. We fix the microphysics parameters to $c_\phi^2 = 0.55$ and $A_\sigma = -0.2$ to explore the broader impact of this negative shear model. This method has the advantage of providing constraints that consider the full range of background evolution possible with this microphysics scenario. However, as with the standard EDE fluid model discussed in Sec. 3.3.1, one must use the full dataset, in particular a late-universe prior on H_0 , in order to find preference for a nonzero density of EDE. While the constraints on S_8 and H_0 in this extended case are similar to the case with a fixed background evolution run on only *Planck* data, the Λ CDM constraint on S_8 from the full dataset, shown in Table 3.3.1, is lower than the Λ CDM constraint from

Parameter	Fiducial	CMB-S4
$100\omega_b$	2.250	± 0.006
ω_c	0.1248	± 0.0025
H_0	69.41	± 0.93
$10^9 A_s$	2.140	± 0.014
n_s	0.9715	± 0.0039
τ	0.0562	± 0.0027
n	6	± 0.09
$a_t \times 10^4$	3.1	± 0.6
$\log(10^{10}\Omega_0)$	-3.95	± 1.08
c_ϕ^2	0.55	± 0.104
A_σ	-0.2	± 0.103

Table 3.3.6: Forecasted 1σ parameter constraints for the PFM model with shear model II assuming a CMB-S4 experiment.

Planck data alone. This results in a weaker softening of the S_8 tension when the background parameters are sampled over, but one that is still statistically relevant. For a more extended discussion of this scenario see Appendix 3.B. Any solution to the cosmological tensions will preferably exist in *Planck* data alone. For this reason, we fix the background evolution in our main analysis. With a fixed background evolution we focus on the effects of EDE microphysics on cosmological parameter constraints from *Planck* data specifically.

This anisotropic microphysics scenario may be a sign of nonscalar field EDE. However, this region of parameter space is indistinguishable from standard scalar field EDE when considering *Planck* data alone, so we must look to future experiments to provide meaningful constraints on the microphysics of EDE.

3.3.5. Future constraints

We forecast constraints on this model using a Fisher information matrix formalism assuming a CMB-S4 experiment that covers 40% of the sky, following the prescription

3.3 RESULTS

laid out in Ref. [101]. We model our Gaussian noise according to

$$N_\ell^{\alpha\alpha} = \Delta^2 \exp\left(\ell(\ell+1)\frac{\theta_{\text{FWHM}}^2}{8 \ln 2}\right) \quad (3.19)$$

where $\alpha \in \{T, E\}$, Δ is the white noise level in $\mu\text{K-arcmin}$, and θ_{FWHM} is the beam width. We consider a telescope beam with $\theta_{\text{FWHM}} = 1'$ and a white noise level of $\Delta_T = 1 \mu\text{K}$ for temperature and $\Delta_E = \sqrt{2}\Delta_T$ for polarization. We compute the covariance matrix as

$$\mathbb{C}_\ell(C_\ell^{\alpha\beta}, C_\ell^{\gamma\delta}) = \frac{1}{(2\ell+1)f_{\text{sky}}} [(C_\ell^{\alpha\gamma} + N_\ell^{\alpha\gamma})(C_\ell^{\beta\delta} + N_\ell^{\beta\delta}) + (C_\ell^{\alpha\delta} + N_\ell^{\alpha\delta})(C_\ell^{\beta\gamma} + N_\ell^{\beta\gamma})], \quad (3.20)$$

where $\alpha, \beta, \gamma, \delta \in \{T, E\}$, and f_{sky} is the fractional sky coverage of the CMB-S4 experiment considered. Finally the Fisher matrix is calculated using

$$F_{ij} = \sum_\ell \frac{\partial C_\ell^\top}{\partial \theta_i} \mathbb{C}_\ell^{-1} \frac{\partial C_\ell}{\partial \theta_j}, \quad (3.21)$$

where θ_i runs over the six ΛCDM parameters, as well as our five model parameters n , a_t , $\log(10^{10}\Omega_0)$, c_\perp^2 , and c_\parallel^2 , making F_{ij} an 11x11 matrix. Table 3.3.6 gives the fiducial model used in our Fisher analysis, as well as the forecasted 1σ constraints on all parameters. Figure 3.4.2, shows the forecasted posterior distributions for c_ϕ^2 and A_σ assuming the fiducial model. From Fig. 3.4.2 we can see that CMB-S4 should be able to distinguish the case with $c_\phi^2 = 0.55$ and $A_\sigma = -0.2$ from the standard EDE model where $c_\phi^2 = 1$ and $A_\sigma = 0$. It is important to note that a Fisher matrix formalism assumes Gaussian errors for all parameters. As suggested by the constraints on c_ϕ^2 and A_σ presented in Fig. 3.3.6 and Fig. 3.4.2, the underlying probability distribution for individual parameters in our model may not be Gaussian. Hence the 1σ error predictions from our Fisher forecast given in Table 3.3.6 should not be thought of as

restrictive constraints. Nevertheless, they serve as useful references on the ability of CMB-S4 to constrain new physics. Assuming the fiducial model and errors presented in Table 3.3.6, CMB-S4 may be able to distinguish the underlying microphysics at the 4σ level. If future constraints do favor $A_\sigma \neq 0$, this would be evidence of a richer microphysics sector than that implied by scalar field EDE.

In short, EDE with an anisotropic shear in the form of Eq. (3.10), with $c_\phi^2 \sim 0.55$ and $A_\sigma \sim -0.2$, can reduce the Hubble tension to $< 3\sigma$, while not exacerbating the S_8 tension like standard EDE models. The region of microphysics parameter space that accomplishes this solution is indistinguishable from a shear-less case with current data, but the CMB-S4 experiment will increase precision, allowing us to concretely assess the viability of altering the microphysics of EDE.

Section 3.4

Discussion

Early dark energy has emerged as one of the most promising classes of solutions to the Hubble tension, however the microphysics of the canonical scalar fields used in these models preclude fully satisfactory solutions mainly by exacerbating the S_8 tension even further. In this paper we investigate the ability of noncanonical microphysics to strengthen EDE as a solution to the Hubble tension. We describe EDE as a phenomenological fluid component whose background evolution mimics standard EDE, and alter the perturbative dynamics of the fluid by allowing the effective sound speed of the fluid to differ from its canonical value of $c_\phi^2 = 1$, and by introducing an anisotropic shear perturbation via an equation of state formalism (shear model I) or an equation of motion (shear model II). In total this phenomenological model constitutes a five parameter extension to Λ CDM, with three parameters to describe the background evolution n , a_t , and $\log(10^{10}\Omega_0)$, and two parameters to describe the

microphysics c_ϕ^2 , and A_σ .

We find that for models with no added anisotropic shear, the H_0 and S_8 tensions can be jointly ameliorated by making the phenomenological fluid cluster through setting $c_\phi^2 = 0$ before the transition in the background equation of state. However, only altering the sound speed leads to a significantly worse fit to *Planck* 2018 data, making this an unfavorable solution to the tensions. This poor fit comes in response to the deepening of gravitational potentials caused by the addition of a new clustering component. Models that transition from a nonclustering to clustering fluid, thereby limiting the time that the clustering can effect the gravitational potentials, suffer the same problem, unless the transition in the sound speed happens well after the fluid density begins to redshift away with $w_\phi = 1$.

Furthermore, we find that the inclusion of anisotropic shear can help or hinder EDE as a solution to the Hubble tension, depending on the way it is introduced. For shear model I, defined by the gauge-invariant equation of state given in Eq. (3.9), the addition of a new shear component to the total stress energy of the system leads to significant changes to the evolution of the density and velocity perturbations of the fluid, and of the evolution of the Weyl potential at large scales. These large-scale changes to the perturbative evolution lead to significant alterations to the CMB angular power spectrum at $\ell < 1000$, which in turn constrain the amount of shear allowed in this model to be negligible.

Alternatively, when anisotropic shear is introduced via the equation of motion given in Eq. (3.10), we find significantly different results. For a non-negligible region of parameter space, the inclusion of this shear in a generic EDE model not only slightly improves upon the resolution to the Hubble tension provided by EDE, but simultaneously softens the S_8 tension with $H_0 = 69.56 \pm 0.60$ km/s/Mpc and $S_8 = 0.833 \pm 0.013$, when compared to the standard EDE case which gives $H_0 = 69.11 \pm 0.58$

km/s/Mpc and $S_8 = 0.849 \pm 0.013$. This favorable region of parameter space loosely given by $c_\phi^2 > 0.6$ and $A_\sigma < -0.2$, is indistinguishable from the standard EDE model using *Planck* 2018 data alone. Using a Fisher information matrix analysis, we found that future observations from CMB-S4 will be able to distinguish between these different microphysical scenarios.

A clear preference for a non-negligible amount of EDE shear would imply that if EDE is at play, it need not be the result of a canonical scalar field. Rather, strongly anisotropic microphysics may be indicative of a novel component that is isotropic at the background level, but breaks isotropy perturbatively. Examples range from free-streaming neutrinos to more speculative models such as a cosmic lattice or coherent vector fields. Our approach has been to study the impact of the equation of state, sound speed, and anisotropic shear more generally.

While our focus has been on the scalar sector, it is reasonable to expect that any microphysical model that gives rise to scalar anisotropic stress will also contribute vector and tensor stress. The latter is of great interest, for the potential to affect a B-mode polarization signal of primordial gravitational waves. A wide range of behavior may be expected, considering free-streaming neutrinos [83], topological defects [104], and coherent vector fields [90]. We leave this subject for later investigation.

Future probes of LSS and the CMB will be essential to verifying if anisotropic EDE was present in the early universe, and will offer further clues into the microphysics of EDE.

3.4 DISCUSSION

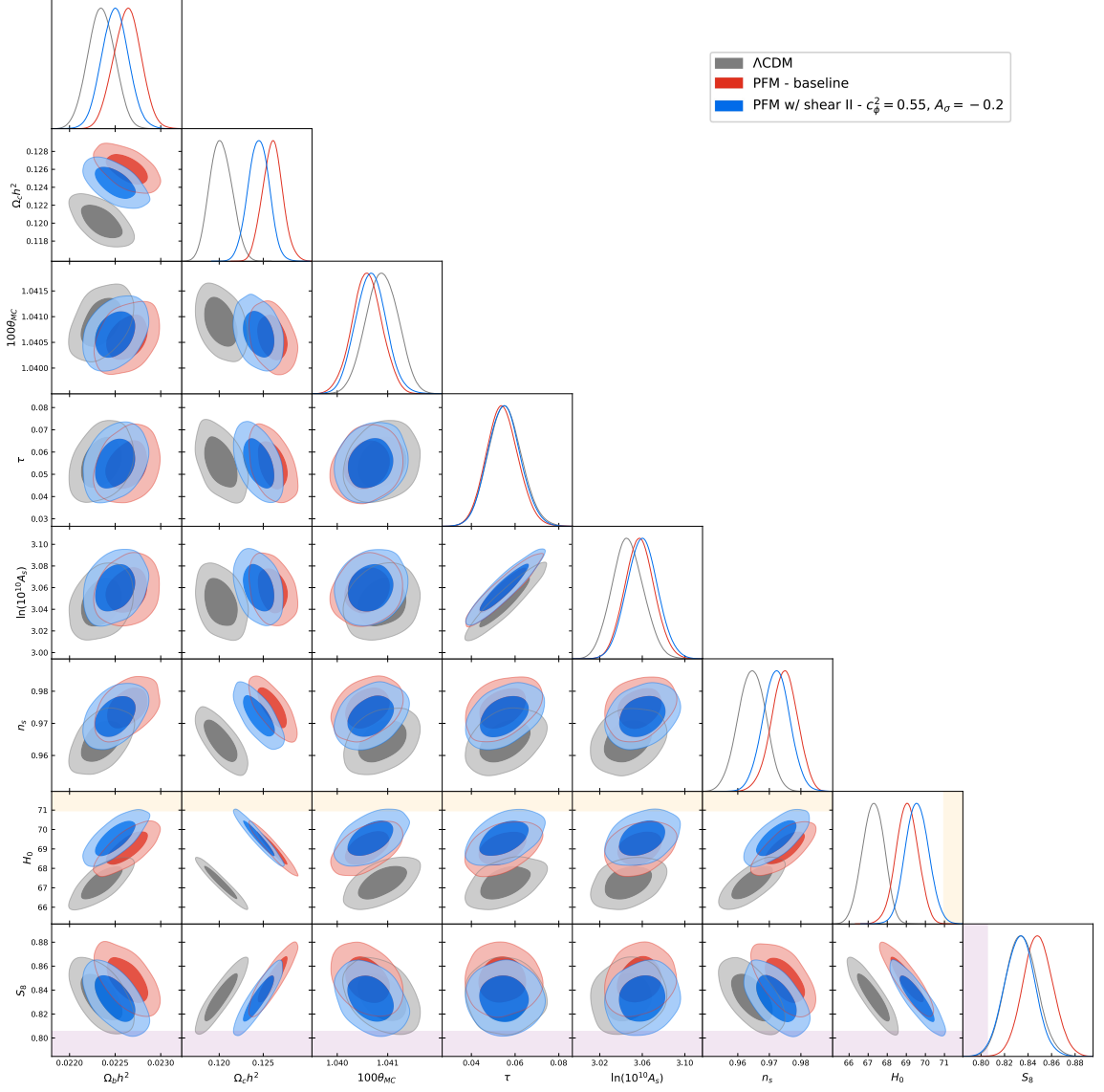


Figure 3.4.1: Posterior distributions for the PFM model with shear model II (blue) with $n = 6$, $\log(10^{10}\Omega_0) = -3.95$, $a_t = 3.1 \times 10^{-4}$, $c_\phi^2 = 0.55$, and $A_\sigma = -0.2$. The Λ CDM (gray) and baseline models (red) are shown for comparison. The darker inner (lighter outer) regions correspond to 1σ (2σ) confidence intervals. The SH0ES collaboration measurement of $H_0 = 73.04 \pm 1.04$ km/s/Mpc and the KiDS-1000 weak lensing survey measurement of $S_8 = 0.759^{+0.024}_{-0.021}$ are shown in the orange and purple bands, respectively [8, 102]. Distributions are generated with the P18 dataset. A small, but non-negligible amount of negative shear added to a generic EDE model can simultaneously soften the H_0 and S_8 tensions in comparison to standard EDE [73].

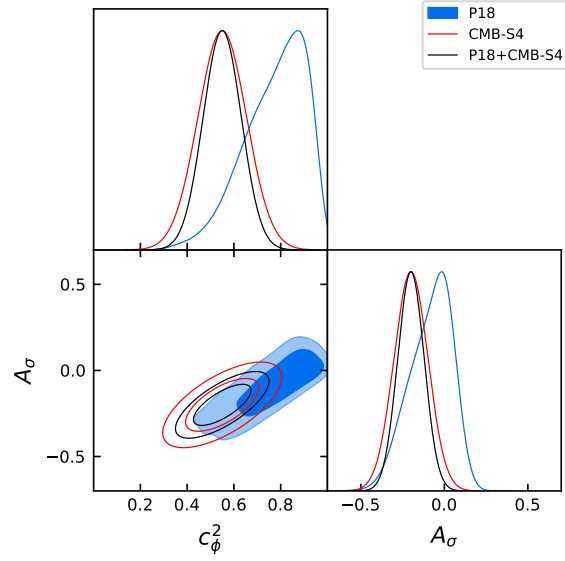


Figure 3.4.2: Forecasts for c_ϕ^2 and A_σ for the CMB-S4 experiment (red) and its combination with *Planck* (black). The blue contour shows current constraints using *Planck* 2018 data alone (same as Fig. 3.3.6). With or without the inclusion of the P18 dataset, CMB-S4 will be able to distinguish a case with a small, but non-negligible amount of shear from the baseline, shear-less case.

Appendix

Section 3.A

Shear Model Derivation

In this Appendix we give extended derivations of the shear models presented in Sec. 3.1.2.

3.A.1. Shear model I

Following [91], the velocity divergence of a single uncoupled fluid, like our phenomenological EDE fluid, can be written most generally as

$$\theta' = -\mathcal{H}(1 - 3w)\theta - \frac{w'}{1 + w}\theta + \frac{k^2}{1 + w} \frac{\delta p}{\rho} - k^2\sigma, \quad (3.22)$$

where the pressure is given by Eq. (3.4). From this equation we can see that the pressure perturbation δp and anisotropic shear σ act as positive and negative source terms respectively. We specifically design our shear equation of state in shear model I to counteract the growth of the pressure source term in Eq. (3.22). We define the shear to be

$$(\rho + p)\sigma = c_\sigma^2(\delta p - c_t^2\delta\rho - 3\mathcal{H}(c_t^2 - c_a^2)(\rho + p)\theta/k^2), \quad (3.23)$$

where c_σ^2 and c_t^2 are new parameters. For $c_\sigma^2 = 1$ and $c_t^2 = 0$, the pressure perturbation source term in Eq. (3.22) is completely canceled, however we choose to leave them

as free parameters for completeness. The second and third terms in Eq. (3.23) are included to keep the stress equation of state gauge invariant. Plugging Eq. (3.4) into Eq. (3.23) we find

$$(\rho + p)\sigma = c_\sigma^2(c_\phi^2 - c_t^2)(\delta\rho + 3\mathcal{H}(\rho + p)\theta/k^2). \quad (3.24)$$

By setting $A_\sigma = c_\sigma^2(c_\phi^2 - c_t^2)$, we recover Eq. (3.9) which we use to define shear model I.

If we directly substitute shear model I into the equation of motion for the velocity perturbation we find

$$\theta' = -\mathcal{H} [1 - 3(c_\phi^2 - A_\sigma)] \theta + \frac{k^2}{1+w}(c_\phi^2 - A_\sigma)\delta, \quad (3.25)$$

where it becomes clear that for $c_\phi^2 = A_\sigma$, we get complete cancellation of the source term for the velocity perturbation making $\theta = 0$ at all times with adiabatic initial conditions.

3.A.2. Shear model II

Our second model of shear is derived directly from the density and velocity perturbations whose evolution equations are given by Eqs. (3.6) and (3.7). We start by differentiating Eq. (3.7) with respect to conformal time to get a second order equation giving

$$\begin{aligned} \theta'' = & -\mathcal{H}'(1 - 3c_\phi^2)\theta - \mathcal{H}(1 - 3c_\phi^2)\theta' + \frac{c_\phi^2}{1+w}k^2\delta' \\ & - 3\mathcal{H}(w - c_a^2)\frac{c_\phi^2}{1+w}k^2\delta - k^2\sigma' \end{aligned} \quad (3.26)$$

where we have assumed a time-varying equation of state and used Eq. (3.5) to simplify. Using Eqs. (3.6) and (3.7) we can write this second order equation as a function exclusively of θ and σ ,

$$\begin{aligned}\theta'' = & -k^2 c_\phi^2 \frac{h'}{2} [-\mathcal{H}(1 - 3c_\phi^2) - 3\mathcal{H}(c_\phi^2 - c_a^2)]\theta' \\ & - [k^2 c_\phi^2 + \mathcal{H}'(1 - 3c_\phi^2) + 3\mathcal{H}^2(c_\phi^2 - c_a^2)]\theta \\ & - k^2 [\sigma' + 3\mathcal{H}(c_\phi^2 - c_a^2)\sigma].\end{aligned}\quad (3.27)$$

At small scales, this simplifies to

$$\theta'' = -k^2 c_\phi^2 \left(\theta + \frac{h'}{2}\right) - k^2 [\sigma' + 3\mathcal{H}(c_\phi^2 - c_a^2)\sigma].\quad (3.28)$$

Now we suppose that

$$\sigma' + 3\mathcal{H}(c_\phi^2 - c_a^2)\sigma = B_\sigma(\theta + \alpha k^2)\quad (3.29)$$

where $\alpha = (h' + 6\eta')/2k^2$ with h and η being the synchronous gauge metric potentials. The right-hand side of this equation is directly taken from the shear terms in the second order differential we derived for the velocity perturbation. At small scales, this implies

$$\theta'' = -k^2 (c_\phi^2 + B_\sigma)\theta - k^2 [(c_\phi^2 + B_\sigma)\frac{h'}{2} + 3B_\sigma\eta'].\quad (3.30)$$

For a wave travelling in the \hat{z} direction, $\theta = \partial_z v^z$, which coupled with the above equation implies $c_\parallel^2 = c_\phi^2 + B_\sigma$. For cohesion between our shear models, we reparametrize and define $B_\sigma = -A_\sigma$ such that $c_\parallel^2 = c_\phi^2 - A_\sigma$, just like in shear model I, which gives us our definition of shear model II presented in Eq. (3.10).

3.B EXTENDED RESULTS

Parameter	$A_\sigma = 0.6$	$A_\sigma = -0.6$
$100\omega_b$	$2.047(2.050) \pm 0.011$	$2.129(2.123) \pm 0.012$
ω_c	$0.1209(0.1210) \pm 0.0012$	$0.1455(0.1457) \pm 0.0010$
$100\theta_s$	$1.03956(1.03951) \pm 0.00029$	$1.03775(1.03773) \pm 0.00030$
τ	$0.0424(0.0429)^{+0.0075}_{-0.0067}$	$< 0.0125(0.0102)$
$\ln(10^{10}A_s)$	$3.031(3.033) \pm 0.015$	$2.9958(2.9931)^{+0.0058}_{-0.0071}$
n_s	$0.9512(0.9507) \pm 0.0037$	$0.9548(0.9536) \pm 0.0038$
c_ϕ^2	0.7 (fixed)	0.3 (fixed)
A_σ	0.6 (fixed)	-0.6 (fixed)
H_0 [km/s/Mpc]	$68.73(68.67) \pm 0.58$	$60.02(59.91) \pm 0.40$
S_8	$0.813(0.816) \pm 0.013$	$1.056(1.057) \pm 0.012$
Total χ^2_{\min}	1472.76	1719.88
$\Delta\chi^2_{\min}$	+458.67	+705.79

Table 3.B.1: The mean (best-fit) $\pm 1\sigma$ error of the cosmological parameters for phenomenological fluid model with shear model I, $n = 6$, $\log(10^{10}\Omega_0) = -3.95$, $a_t = 3.1 \times 10^{-4}$, and different choices of c_ϕ^2 and A_σ , generated from the P18 dataset. The best-fit values were used to generate the orange and red curves in Fig. 3.3.8.

Section 3.B

Extended Results

In this Appendix we present extended MCMC results from our analysis of the phenomenological EDE fluid model with varied microphysics. In Table 3.B.1 we give the parameter constraints for the positive and negative A_σ cases run on the P18 dataset used to produce the residuals seen in Fig. 3.3.8 for shear model I. As explained in Sec. 3.3, the large scale impact of the anisotropic shear in this model causes the poor fits we see in Table 3.B.1, and constrains the amount of shear allowed to be negligible.

In Table 3.B.2, we show constraints on the cosmological parameters in the baseline PFM, the PFM w/ shear model I and the PFM w/ shear model II run using the P18+BAO+R19+SN datasets. Posterior distributions for the relevant parameters in these models are shown in Figs. 3.B.1 and 3.B.2, with Λ CDM shown for comparison. Comparing to Tables 3.3.4 and 3.3.5, we can see that the inclusion of additional

datasets does allow for slightly more anisotropic shear with a higher H_0 , but does not significantly change the results for either model of shear.

Parameter	PFM - baseline	PFM w/ shear I	PFM w/ shear II
$100\omega_b$	$2.278(2.280) \pm 0.013$	$2.268(2.273) \pm 0.016$	$2.267(2.272) \pm 0.015$
ω_c	$0.12466(0.12464) \pm 0.00083$	$0.12449(0.12462) \pm 0.00087$	$0.12418(0.12435) \pm 0.00088$
$100\theta_s$	$1.04079(1.04076) \pm 0.00028$	$1.04083(1.04082)^{+0.00027}_{-0.00030}$	$1.04081(1.04101) \pm 0.00030$
τ	$0.0584(0.0582) \pm 0.0071$	$0.0578(0.0598) \pm 0.0076$	$0.0583(0.05711)^{+0.0068}_{-0.0077}$
$\ln(10^{10}A_s)$	$3.064(3.065) \pm 0.014$	$3.063(3.067) \pm 0.015$	$3.064(3.062)^{+0.014}_{-0.015}$
n_s	$0.9786(0.9775) \pm 0.0036$	$0.9782(0.9783) \pm 0.0037$	$0.9768(0.9786)^{+0.0046}_{-0.0042}$
c_ϕ^2	-	$0.799(0.787)^{+0.140}_{-0.085}$	$0.748(0.812)^{+0.180}_{-0.096}$
A_σ	-	$-0.036(-0.058) \pm 0.058$	$-0.11(-0.06)^{+0.15}_{-0.11}$
H_0 [km/s/Mpc]	$69.80(69.81) \pm 0.42$	$69.79(69.78) \pm 0.43$	$69.89(69.95) \pm 0.43$
S_8	$0.8344(0.8342) \pm 0.0098$	$0.833(0.836) \pm 0.010$	$0.830(0.830) \pm 0.011$
Total χ^2_{\min}	2063.81	2063.59	2064.02
$\Delta\chi^2_{\min}$	-9.56	-9.78	-9.35

Table 3.B.2: The mean (best-fit) $\pm 1\sigma$ error of the cosmological parameters in the baseline model, the PFM with shear I, and the PFM with shear II, generated from the P18+BAO+R19+SN datasets.

3.B EXTENDED RESULTS

Parameter	PFM w/ shear II - $A_\sigma = -0.2$
$100\omega_b$	$2.259(2.256) \pm 0.014$
ω_c	$0.12362(0.12379) \pm 0.00087$
$100\theta_s$	$1.04079(1.04080) \pm 0.00029$
τ	$0.0579(0.0540)^{+0.0069}_{-0.0078}$
$\ln(10^{10} A_s)$	$3.064(3.058)^{+0.014}_{-0.016}$
n_s	$0.9746(0.9751) \pm 0.0036$
c_ϕ^2	0.55 (fixed)
A_σ	-0.2 (fixed)
H_0 [km/s/Mpc]	$70.03(69.94) \pm 0.45$
S_8	$0.825(0.824) \pm 0.010$
Total χ^2_{\min}	2065.55
$\Delta\chi^2_{\min}$	-7.82

Table 3.B.3: The mean (best-fit) $\pm 1\sigma$ error of the cosmological parameters for phenomenological fluid model with shear model II, $n = 6$, $\log(10^{10}\Omega_0) = -3.95$, $a_t = 3.1 \times 10^{-4}$, $c_\phi^2 = 0.55$, and $A_\sigma = -0.2$, generated from the P18+BAO+R19+SN datasets.

Next, we give the results of an MCMC analysis, consisting of constraints on cosmological parameters in Table 3.B.3 and posterior distributions for those parameters in Fig. 3.B.3, for the phenomenological EDE fluid with shear model II. We show the case of $c_\phi^2 = 0.55$ and $A_\sigma = -0.2$, discussed in Sec. 3.3, run on the P18+BAO+R19+SN datasets. Similarly to the previous cases, the inclusion of more datasets does not drastically alter the results of the analysis. The main differences are slight upwards and downwards shifts in the posteriors for H_0 and S_8 , respectively when compared to the run with only *Planck* 2018 data. However, in comparison to the best-fit Λ CDM model run on the same extended dataset, the resolutions to the H_0 and S_8 tensions are less pronounced.

Finally, to see the broader impact of this negative shear model we re-run our analysis to include sampling over the background model parameters r_ϕ , a_t , and n . We hold the microphysics fixed with $c_\phi^2 = 0.55$ and $A_\sigma = -0.2$ and explore the effect of this microphysics scenario on the background EDE solution. Parameter constraints on this case are given in Table 3.B.4 with their posterior distributions shown in Fig. 3.B.4

for the P18 dataset, and Fig. 3.B.5 for the combined P18+BAO+R19+SN datasets.

As can be seen by comparing Tables 3.3.1 and 3.B.4, the constraints on the model parameters follow a similar trajectory for a standard EDE model and for this negative shear case. As with the standard EDE fluid model presented in Table 3.3.1, *Planck* data alone shows no preference for EDE with a best-fit EDE density fraction of $r_\phi = 0.005$. Hence, there is no solution to the Hubble tension with a best-fit $H_0 = 67.52$ km/s/Mpc, and the constraint on S_8 is unchanged from Λ CDM with $S_8 = 0.837(0.834) \pm 0.013$.

As discussed in Sec. 3.3.1, for a nonzero amount of EDE to be preferred, we must include a late-universe prior on H_0 . Any solution to the cosmological tensions would preferably exist in *Planck* data alone, without the need for external datasets to enforce parameter changes. This is why in our main analysis of these models we fix the background evolution and investigate the effect of EDE microphysics under the assumption of a non-negligible EDE density around matter-radiation equality, allowing us to exclusively use *Planck* data in our analysis.

Considering the full dataset in this extended parameter space we find $S_8 = 0.834(0.836) \pm 0.012$ for this negative shear model shown in Table 3.B.4. Compared to the standard EDE fluid model constraint of $S_8 = 0.840(8.41) \pm 0.013$ on this same dataset, we still see preference for a lower value of S_8 . Comparing these values to the cases with fixed background evolution (shear model II with $A_\sigma = -0.2$ and the baseline EDE case, respectively) discussed in the main text, we see good agreement between models in both cases. However, for the full dataset considered here, the Λ CDM constraint is lowered to $S_8 = 0.816(0.817) \pm 0.010$, making the softening of the S_8 tension weaker, but still statistically relevant as the standard EDE constraint lies outside the Λ CDM 1- σ error bars.

Parameter	P18 only	P18+BAO+R19+SN
$100\omega_b$	$2.237(2.239)^{+0.016}_{-0.018}$	$2.274(2.228) \pm 0.018$
ω_c	$0.1224(0.1206)^{+0.0014}_{-0.0026}$	$0.1278(0.1292) \pm 0.0036$
$100\theta_s$	$1.04073(1.04080) \pm 0.00033$	$1.04046(1.04044) \pm 0.00038$
τ	$0.0540(0.0569) \pm 0.0073$	$0.562(0.0547) \pm 0.0073$
$\ln(10^{10}A_s)$	$3.049(3.049)^{+0.014}_{-0.015}$	$3.067(3.070) \pm 0.015$
n_s	$0.9656(0.9657)^{+0.0046}_{-0.0054}$	$0.9768(0.9791) \pm 0.0054$
$1/n$	$< 0.600(0.331)$	$0.397(0.377)^{+0.098}_{-0.180}$
r_ϕ	$< 0.0196(0.0052)$	$0.072(0.083) \pm 0.026$
$a_t \times 10^4$	$< 4.35(2.59)$	$< 2.98(2.70)$
H_0 [km/s/Mpc]	$67.97(67.52)^{+0.61}_{-1.10}$	$71.0(71.50) \pm 1.1$
S_8	$0.837(0.834) \pm 0.013$	$0.834(0.836) \pm 0.012$
Total χ^2_{\min}	1013.77	2061.43
$\Delta\chi^2_{\min}$	-0.32	-11.94

Table 3.B.4: The mean(best-fit) $\pm 1\sigma$ error on the cosmological parameters for the PFM w/ shear model II for the case of $c_\phi^2 = 0.55$ and $A_\sigma = -0.2$, with sampling over the background PFM parameters.

3.B EXTENDED RESULTS

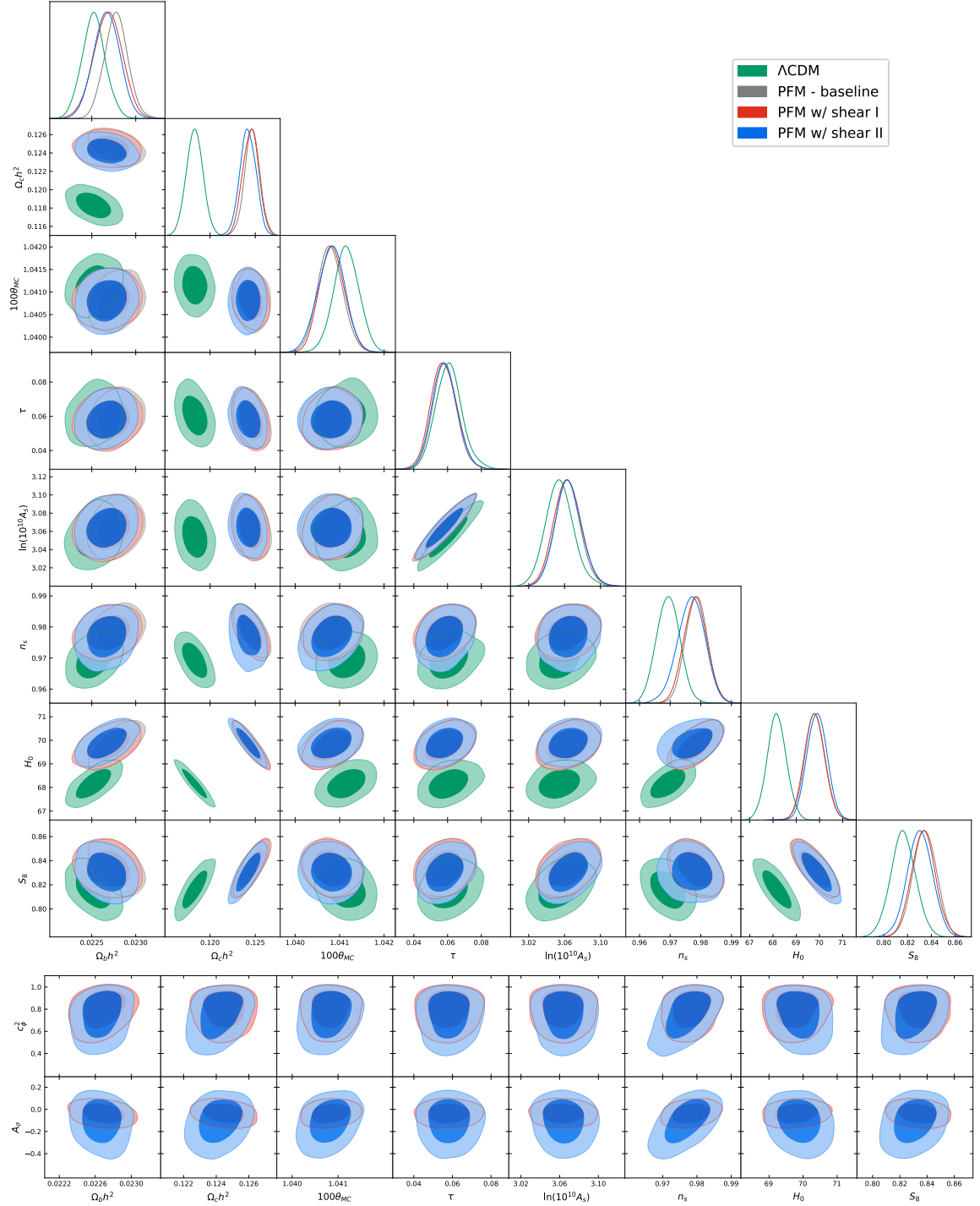


Figure 3.B.1: Same as Fig. 3.3.5 but for the P18+BAO+R19+SN datasets.

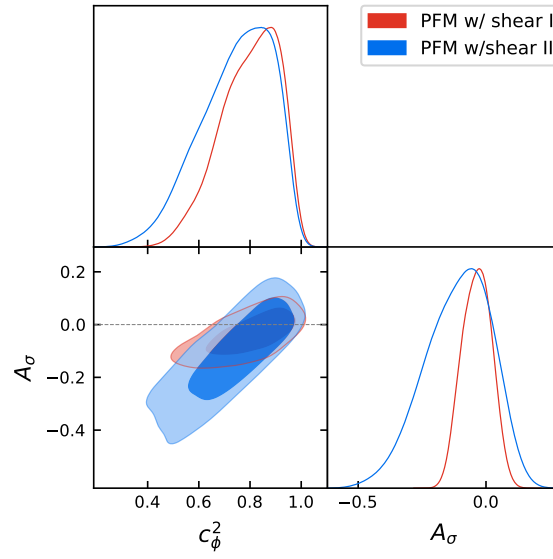


Figure 3.B.2: Same as Fig. 3.3.6 but for the P18+BAO+R19+SN datasets.

3.B EXTENDED RESULTS

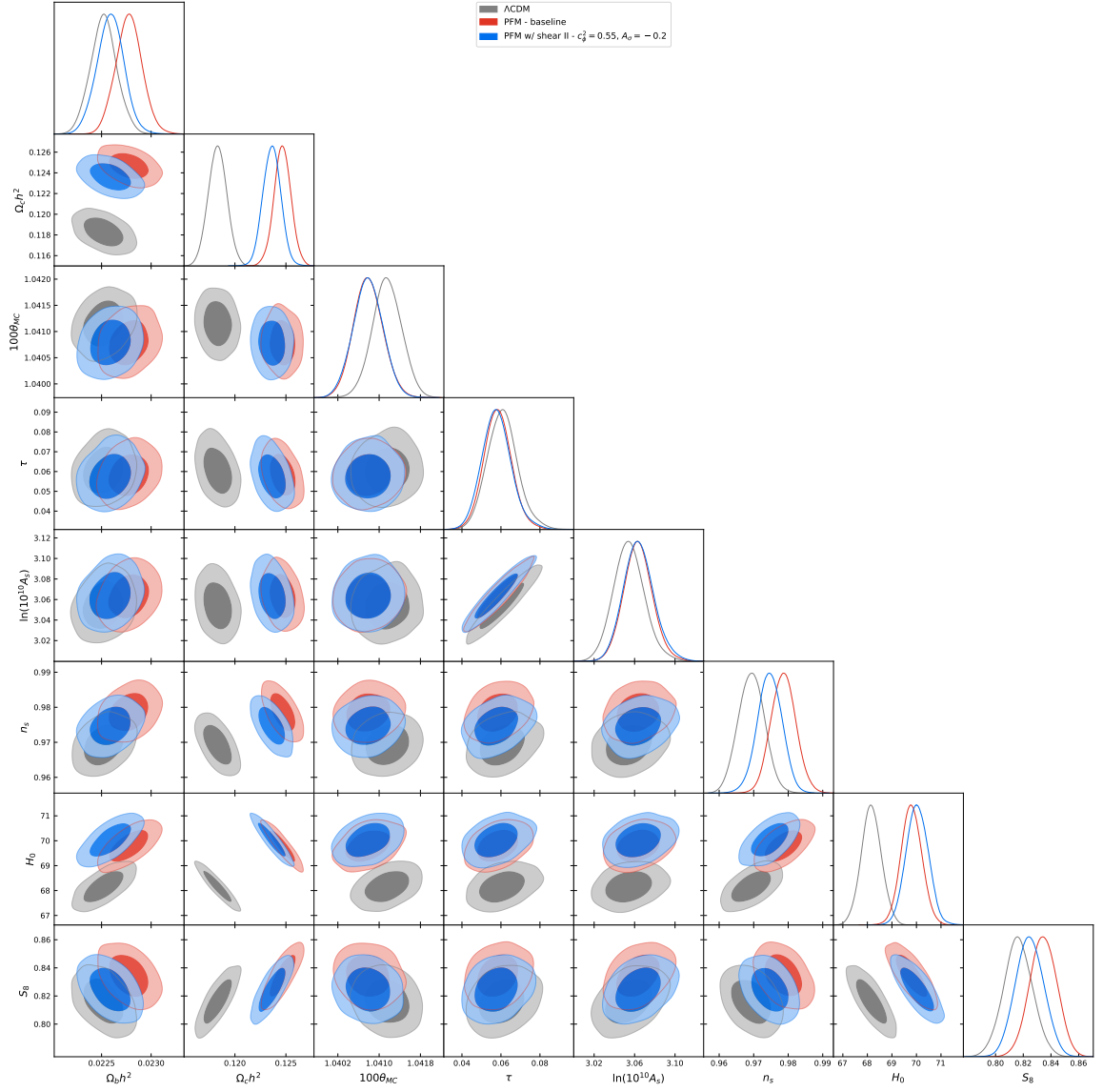


Figure 3.B.3: Same as Fig. 3.4.1 but for the P18+BAO+R19+SN datasets.

3.B EXTENDED RESULTS

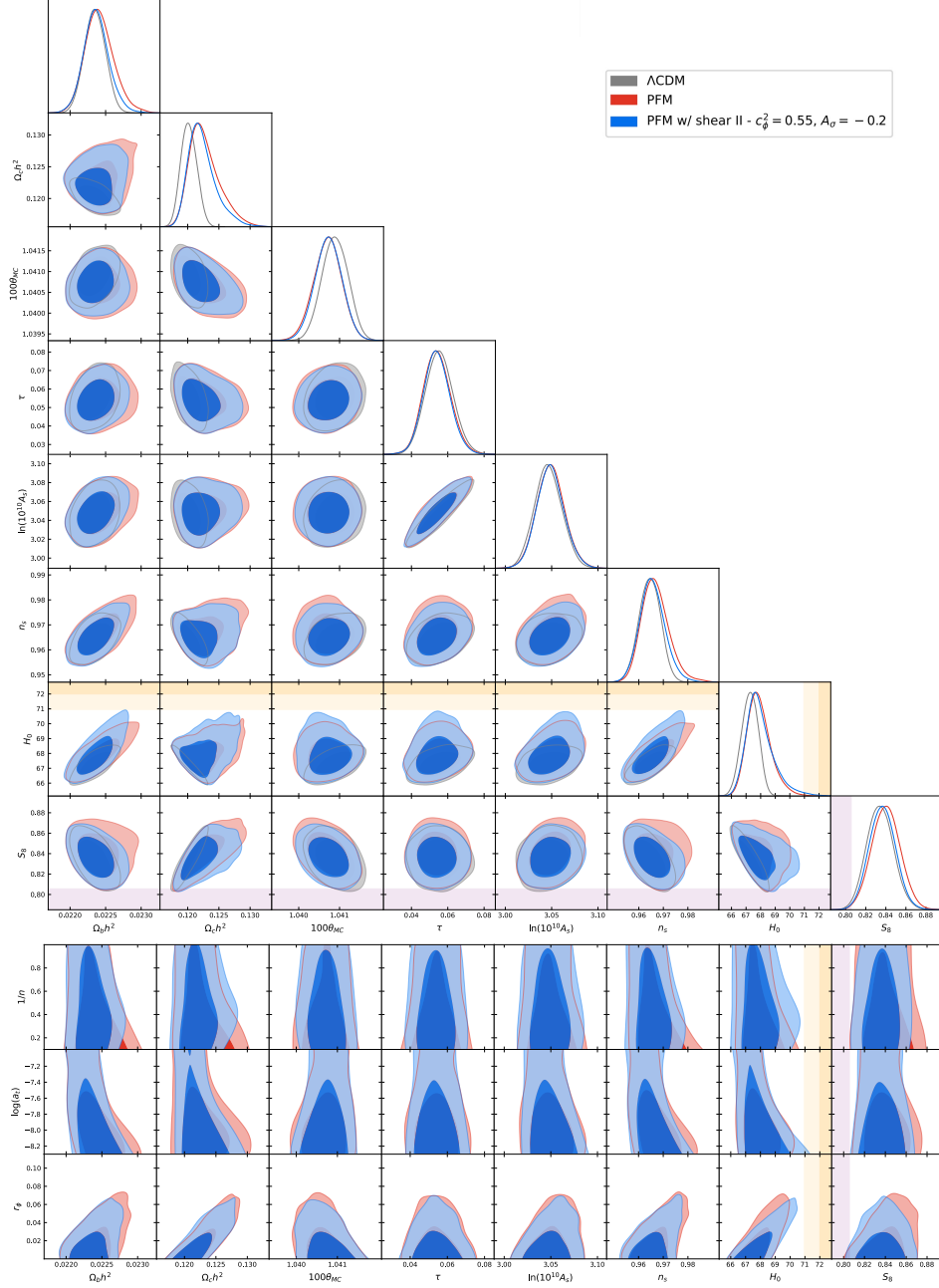


Figure 3.B.4: Top: Posterior distributions of the standard model parameters for the Λ CDM model (gray), the PFM with $c_\phi^2 = 1$ and $A_\sigma = 0$ (red), and shear model II with $c_\phi^2 = 0.55$ and $A_\sigma = -0.2$ (blue). Bottom: Posterior distributions of the standard model parameters vs the background PFM parameters. The darker inner (lighter outer) regions correspond to 1σ (2σ) confidence intervals. The SH0ES Collaboration measurement of $H_0 = 73.04 \pm 1.04$ km/s/Mpc and the KiDS-1000 weak lensing survey measurement of $S_8 = 0.759^{+0.024}_{-0.021}$ are shown in the orange and purple bands, respectively [8, 102]. Distributions are generated with the P18 dataset.

3.B EXTENDED RESULTS

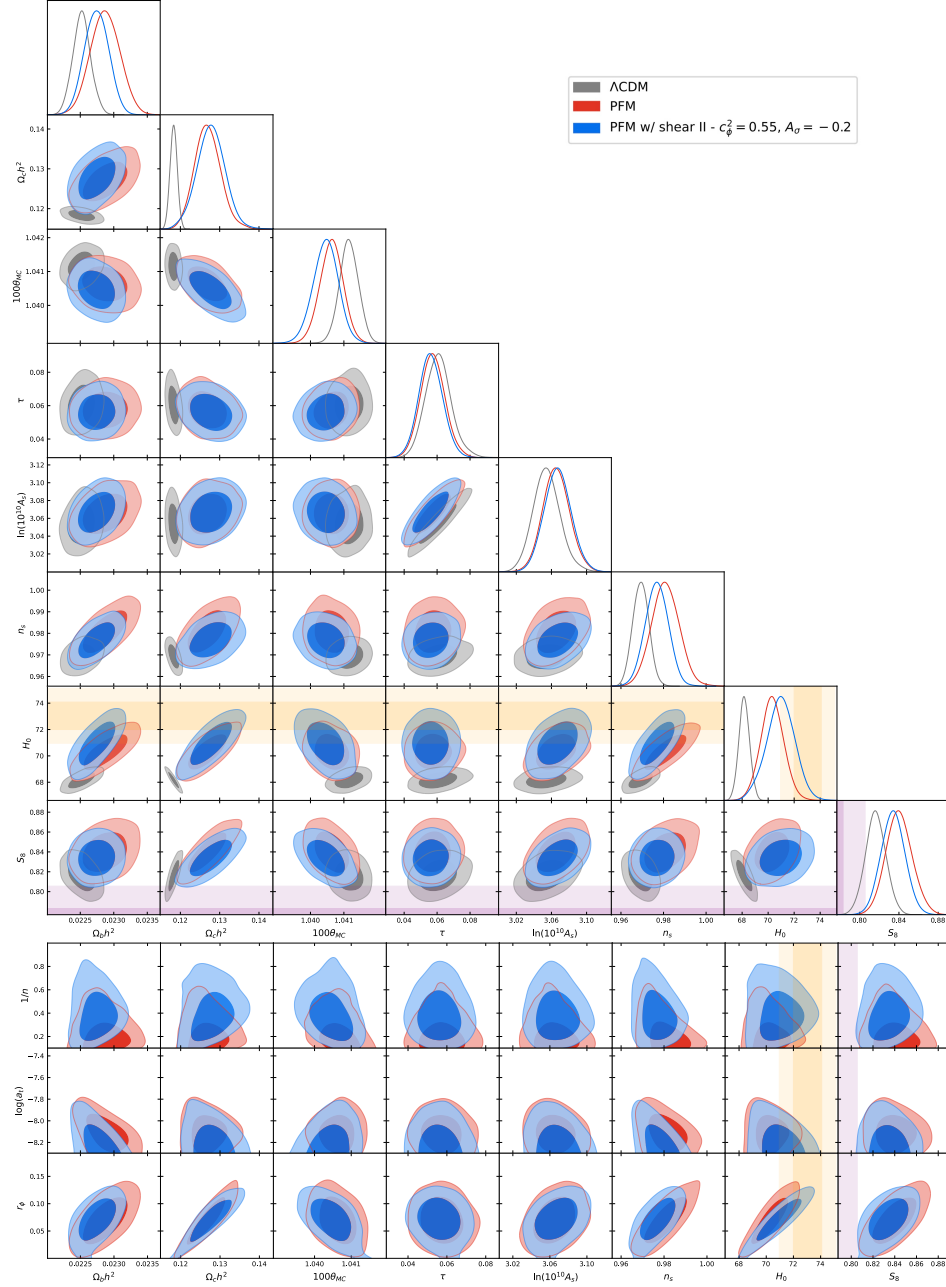


Figure 3.B.5: Top: Posterior distributions of the standard model parameters for the Λ CDM model (gray), the PFM with $c_\phi^2 = 1$ and $A_\sigma = 0$ (red), and shear model II with $c_\phi^2 = 0.55$ and $A_\sigma = -0.2$ (blue). Bottom: Posterior distributions of the standard model parameters vs the background PFM parameters. The darker inner (lighter outer) regions correspond to $1\sigma(2\sigma)$ confidence intervals. The SH0ES Collaboration measurement of $H_0 = 73.04 \pm 1.04$ km/s/Mpc and the KiDS-1000 weak lensing survey measurement of $S_8 = 0.759^{+0.024}_{-0.021}$ are shown in the orange and purple bands, respectively [8, 102]. Distributions are generated with the P18+BAO+R19+SN datasets.

Chapter 4

Joint LIM power spectrum and VID constraints on BSM cosmologies

With changes, this chapter is adapted from Sabla, V.I., Sato-Polito, G., Bernal, J.L., & Kamionkowski, M. “Joint LIM power spectrum and voxel intensity distribution constraints on beyond- Λ CDM cosmologies.” to be submitted to Phys. Rev. D (2023).

Line-intensity mapping (LIM) has recently emerged as a promising technique to bridge the gap between early- and late-universe cosmological observations, providing direct observations of cosmic dawn and reionization [105–107]. Conventional galaxy surveys measure the positions and redshifts of individual galaxies, whereas LIM measures the integrated emission along the line-of-sight from bright spectral lines originating from all galaxies, including individually unresolved sources, as well as from the diffuse intergalactic medium [108]. Both galaxy surveys and LIM serve as biased tracers of the underlying matter distribution, giving measurements of the large-scale structure

of the Universe. By probing vast cosmological volumes, with relatively low spatial resolution, at redshifts beyond the reach of galaxy surveys and other cosmological observations, intensity maps can efficiently track the makeup and growth of large-scale structure and the distribution of dark matter as well as astrophysical phenomena including the formation and evolution of galaxies and properties of the intergalactic medium. First developed as a technique to probe the 21-cm hyperfine transition in neutral hydrogen [109–111], LIM has blossomed in recent years, with many experiments currently underway [112–120], and under construction [121–127], each targeting atomic and molecular spectral lines sourced at redshifts ranging from the present day to cosmic dawn.

As the experimental landscape opens, accurate theoretical modelling of intensity-mapping signals, degeneracies, and contaminants is of the utmost importance in order to derive accurate astrophysical and cosmological constraints. The challenge for using LIM to constrain cosmology comes from the inherent dependence of the astrophysical and cosmological signals. Uncertainties in the astrophysics of line-emission serve as effective nuisance parameters in deriving constraints on cosmological parameters. A number of techniques have been proposed for extracting cosmological information from line-intensity maps. The primary statistic used is the LIM power-spectrum which to linear order depends only on the first two moments of the line luminosity function. Since line emission originates in halos, the intensity of the chosen spectral line traces the underlying matter distribution. However, line emission is inherently entangled with the astrophysical processes that take place in these halos during reionization and galaxy evolution, making the power spectrum limited due to degeneracies between the cosmology and the astrophysics of line-emission [108, 128, 129]. At both large and small scales, the power spectrum is also limited by foregrounds, survey-volumes, and resolution.

Complementary statistics, such as the voxel intensity distribution (VID), have been proposed to break these degeneracies with astrophysical parameters [130], and provide information on a wider range of scales. The VID estimates the one-point probability distribution function of the temperatures or intensities measured within a voxel [131], and depends directly on the luminosity function of the spectral line of interest, making it particularly useful for constraining the astrophysics of line-emission. A joint analysis using both the power-spectrum and VID, which requires a covariance matrix to account for the shared information content between the two observables, has been shown to break precision limiting degeneracies and significantly improve the inference of the line-luminosity function [132–134]. Previous joint analyses empirically estimate the covariance from simulations [132], however Ref. [130] derived an analytic expression for the covariance which depends on the integrated bispectrum of one power of the emitter overdensity and two of the intensity (or temperature) fluctuations.

In this work, we take advantage of the analytic covariance between the LIM power spectrum and VID, and explore how the combination of statistics influences LIM parameter constraints on beyond the standard model cosmologies. While the Λ CDM model, consisting of a cosmological constant Λ , and cold dark matter (CDM), provides extraordinarily good descriptions of many cosmological observations, its predictions at small (sub-galactic) scales are in tension with observations [15], particularly, too much dark matter is predicted in the inner-most regions of galaxies, giving rise to what is known as the “cusp-core” problem [16]. One possible solution is to go beyond the standard CDM description such that a suppression of gravitational clustering at small-scales is induced, with respect to Λ CDM. Many such “non-cold” dark matter (nCDM) candidates exist (see e.g. [135] for a review), each leading to different shapes in the suppression of the power spectrum. Previous work has shown that stage-3 IM

experiments can be used to constrain primordial power-suppression at small-scales via the VID [136]. In this work we consider a phenomenological model which encapsulates the small-scale suppression of power due to non-cold dark matter (nCDM), as well as a fully physical case of axion dark matter [137–145], where we can follow the full evolution of perturbations, giving tighter constraints. We focus on these non-cold dark matter models as they alter the halo-mass function at low-masses, where the inclusion of the VID in our analysis will boost sensitivity considerably.

While nCDM models we consider alter physics at small scales, we also show the capability of our analytic joint analysis at constraining large-scale deviations from the standard model. An early period of inflationary expansion is the most accepted paradigm for explaining the observed Universe, however the specific model which gives rise to such an epoch is weakly constrained by current cosmological data. The *Planck* satellite has confirmed that the field which sources the observed structure of the Universe must be very close to Gaussian [146]. However, small deviations from a primordially Gaussian field are allowed and, in fact, generically predicted in the standard perturbation generating mechanisms provided by many inflationary models, each providing different degrees of non-Gaussianity. As such, in this work we also consider the effect of local non-Gaussianity on both the halo bias and halo-mass function at large scales and masses, and investigate the change in constraining power at large scales that comes in our joint analysis.

Although the methods we present in this study can be generically applied to any spectral line, we focus on the $H\alpha$ line of neutral hydrogen, which will be measured in the upcoming SPHEREx deep survey at redshifts $0.1 < z < 5$ [125], as an example of near-term observational capabilities. $H\alpha$ is one of the brightest lines emitted in young star-forming galaxies, making it a fairly direct probe of star-forming galaxy’s number density, star formation rate, and large scale structure at high redshifts [147–149].

This chapter is organized as follows. In Sec. 4.1, we review the formalism needed to compute the LIM power spectrum and VID, including survey limitations and instrumental noise, as well as the covariance between the two observables. We present the model of H α emission we consider in Sec. 4.2. Next, we describe the beyond- Λ CDM cosmological scenarios considered, and discuss their impact on the LIM observables in Sec. 4.3. In Sec. 4.4, we present the survey specifications we use to derive constraints, give details on our Fisher forecasting method and present our constraints on each cosmological model considered. We end in Sec. 4.5 with a discussion of our results.

Section 4.1

LIM Observables

In this section we review the modelling of the power spectrum and voxel intensity distribution, as well as their variance and the covariance between the two signals. We include an explanation of our modelling of noise and survey specifications that limit the intrinsic signals.

The specific intensity of a given radiation source at a redshift z with a rest-frame frequency ν is related to the local luminosity density $\rho_L(z)$ via

$$I(z) = \frac{c}{4\pi\nu H(z)} \rho_L(z) \equiv X_{LI} \rho_L(z), \quad (4.1)$$

where c is the speed of light, $H(z)$ is the Hubble parameter at the target redshift, and we define X_{LI} in our second equality to simplify the expression. The average luminosity density can be computed using the halo mass function dn/dM , assuming a relationship between the luminosity of the spectral line and the mass M of the host

halo:

$$\langle \rho_L \rangle(z) = \int dM L(M, z). \quad (4.2)$$

Using these expressions, we can derive the one- and two-point summary statistics, described below, which we use to extract astrophysical and cosmological information from line-intensity maps.

4.1.1. Power Spectrum

The primary statistic used in evaluating intensity maps is the power spectrum $P(k)$, given by the Fourier transform of the two-point correlation function of perturbations of the intensity $\delta I \equiv I - \langle I \rangle$. Since spectral lines are sourced in dark matter halos, δI can be used as a biased tracer of the underlying matter density perturbations, contributing a clustering component to the overall LIM power spectrum. Due to the discrete distribution of dark matter halos, there will be an additional scale-independent shot-noise contribution giving $P(k, \mu, z) = P_{\text{clust}}(k, \mu, z) + P_{\text{shot}}(z)$, where k is the magnitude of the Fourier mode, and μ is the cosine of the angle between the wave mode vector \mathbf{k} and the line-of-sight component k_{\parallel} .

To first order, the matter density and intensity perturbations are related by an effective linear bias given by

$$b(z) = \frac{1}{\langle \rho_L \rangle(z)} \int dM L b_h \frac{dn}{dM}, \quad (4.3)$$

where all quantities inside the integral depend on the halo-mass M and redshift, and b_h denotes the halo bias. Thus, the power spectrum can be written as

$$P(k, \mu, z) = \langle I(z) \rangle^2 \left(b(z) + f(z) \mu^2 \right)^2 P_m(k, z) + \langle I^2 \rangle, \quad (4.4)$$

where $f(z)$ is the linear growth rate, P_m is the linear power spectrum of cold dark

matter and baryons, and we have assumed a Poisson shot noise. The $f(z)\mu^2$ term is included to model the boost in the power spectrum due to the peculiar velocities of galaxies, known as the Kaiser effect [150].

4.1.2. Voxel Intensity Distribution

The VID is an estimator for the probability distribution function (PDF) of the line-intensity in an observed voxel $\mathcal{P}(I)$. The observed intensity in a given voxel is simply the sum of the intensities emitted by each source contained in a voxel. Thus we can write the PDF of astrophysical sources as

$$\mathcal{P}(I) = \sum_{N=0}^{\infty} \mathcal{P}_N(I) \mathcal{P}(N), \quad (4.5)$$

where we sum the conditional probabilities of having N emitters in a voxel $\mathcal{P}(N)$, and the PDF of their total intensity $\mathcal{P}_N(I)$, over all possible values of N .

A voxel containing no sources will contribute zero intensity such that $\mathcal{P}_0(I) = \delta_D(I)$, where δ_D is the Dirac delta function. A voxel containing a single source will have a PDF directly related to the luminosity function dn/dL of the target emission line:

$$\mathcal{P}_1(I) = \frac{V_{\text{vox}}}{\bar{n} X_{LI}} \frac{dn}{dL} \bigg|_{L=\rho_L(I) V_{\text{vox}}}, \quad (4.6)$$

where \bar{n} is the average comoving number density of sources and dn/dL is computed from the halo-mass function and the assumed $L(M)$ relation for the target line. Since intensity is additive, the intensity PDF for an arbitrary number of emitters in a voxel is simply \mathcal{P}_1 convoluted with itself N times $\mathcal{P}_N(I) = (\mathcal{P}_{N-1} * \mathcal{P}_1)(I)$ ¹.

The number of emitters in a voxel obeys a Poisson distribution with the mean

¹Ref. [134] improved the formalism of the VID during the development of this project. Since this is a proof-of-concept study that focuses on the differences in the signal due to physics beyond Λ CDM rather than in the signal itself, we consider our conclusions to be unaffected by this change in the formalism.

number of sources $\bar{N} = \bar{n}V_{\text{vox}}$, where \bar{n} is the average comoving number density of sources, and V_{vox} is the volume of a voxel. Following Ref. [131], we assume that the halo number count follows that of the underlying dark matter, which can be approximated using a lognormal distribution [151].

Finally, as there are no perfect experiments, there will be a thermal noise contribution to the total observed intensity per voxel which we model as a Gaussian distribution with standard deviation given by the effective instrumental noise per voxel, making the final total intensity PDF

$$\mathcal{P}_{\text{tot}}(I) = (\mathcal{P}_{\text{noise}} * \mathcal{P})(I). \quad (4.7)$$

In practice, \mathcal{P}_{tot} is not directly measurable from intensity maps. However it can be estimated via the computation of histograms of the number of voxels \mathcal{B}_i for which the measured intensity is within a given intensity bin with width ΔI_i . The relation between the observable \mathcal{B}_i and $\mathcal{P}_{\text{tot}}(I)$ is

$$\mathcal{B}_i = N_{\text{vox}} \int_{\Delta I_i} dI \mathcal{P}_{\text{tot}}(I), \quad (4.8)$$

where $N_{\text{vox}} = \Omega_{\text{field}} \Delta\nu / \theta_{\text{FWHM}}^2 \delta\nu$ is the total number of voxels in the observed volume.

4.1.3. Noise & Survey Specifications

Due to the limited resolution and finite observed volume of LIM experiments, the observed power spectrum will differ from the one predicted by Eqn. (4.4), mainly by limiting the minimum and maximum accessible scales, respectively. Following Ref. [130], we model these experimental limitations by applying window functions to

our predicted power spectrum:

$$\tilde{P}(k, \mu) = \int \frac{d^3 \mathbf{q}}{(2\pi)^3} W_{\text{res}}^2(\mathbf{k}) W_{\text{vol}}^2(\mathbf{q} - \mathbf{k}) P(\mathbf{q} - \mathbf{k}), \quad (4.9)$$

where W_{vol} and W_{res} model the limited survey volume and voxel resolution, respectively, and the tilde denotes an observed quantity. As W_{res} captures the loss of information on scales smaller than the size of the voxel, it is applied as a convolution in real space, and a product in Fourier space. Conversely, W_{vol} cuts off certain spatial positions, thus it is applied as a product in real space, and a convolution in Fourier space.

The spectral and angular resolutions of the telescope define the resolution limits in the radial and transverse directions, respectively,

$$\sigma_{\parallel} = \frac{c\delta\nu(1+z)}{H(z)\nu_{\text{obs}}}, \quad \sigma_{\perp} = D_M(z)\theta_{\text{FWHM}}, \quad (4.10)$$

where $\delta\nu$ is the spectral resolution, ν_{obs} is the observed frequency of a given line, $H(z)$ is the Hubble parameter, $D_M(z)$ is the co-moving angular diameter distance, and θ_{FWHM} is the full-width half maximum of the beam. As in Ref. [152], we assume a Gaussian function in Fourier space to model the resolution window as

$$W_{\text{res}}(k, \mu) = \exp \left\{ -k^2 [\sigma_{\parallel}^2 \mu^2 + \sigma_{\perp}^2 (1 - \mu^2)] \right\}. \quad (4.11)$$

We assume a cylindrical volume along the line of sight, with side length $L_{\parallel} = c\Delta\nu(1+z)/H(z)\nu_{\text{obs}}$ and radius $R_{\perp} = D_M(z)\sqrt{\Omega_{\text{field}}/\pi}$, where $\Delta\nu$ is the instrumental frequency bandwidth, and Ω_{field} is solid angle observed. Assuming that all spatial positions in the survey are observed with the same efficiency we model the volume window as a top hat in configuration space with values of 1 and 0 for points within

and outside this volume respectively. In cylindrical coordinates this becomes,

$$W_{\text{vol}}(k_{\parallel}, k_{\perp}) = \frac{1}{V_{\text{field}}} \frac{2\pi R_{\perp} L_{\parallel}}{k_{\perp}} J_1(k_{\perp} R_{\perp}) \text{sinc}\left(\frac{k_{\parallel} L_{\parallel}}{2}\right), \quad (4.12)$$

where $V_{\text{field}} = L_{\parallel} L_{\perp}^2$ is the comoving volume of the observed field, $k_{\parallel} = k\mu$, $k_{\perp} = k\sqrt{1 - \mu^2}$, and J_1 is the Bessel function of the first kind.

On top of the clustering and shot noise components, the total observed LIM power spectrum will also include a component due to instrumental noise giving a final expression

$$\tilde{P}_{\text{tot}}(k, \mu) = \tilde{P}_{\text{clust}}(k, \mu, z) + \tilde{P}_{\text{shot}}(k, \mu, z) + P_N(z), \quad (4.13)$$

where \tilde{P}_{clust} and \tilde{P}_{shot} represent the volume and resolution limited power spectrum computed from Eq. (4.4) and (4.9). Assuming a Gaussian instrumental noise, the noise power spectrum P_N is given by

$$P_N = V_{\text{vox}} \sigma_N^2, \quad (4.14)$$

where V_{vox} is the volume of the voxel, and σ_N is the standard deviation of the instrumental noise per voxel. Values for σ_N are presented in Sec. 4.4.1.

Lastly, in our analysis we consider only the monopole of the power spectrum, which can be simply computed from Eq. (4.13) as

$$\tilde{P}_0(k) = \frac{1}{2} \int d\mu \tilde{P}_{\text{tot}}(k, \mu). \quad (4.15)$$

The inclusion of higher-order multipoles would lead to a minimal increase in precision compared with the precision gained from the combination of the monopole and VID, hence for simplicity we consider only the monopole in this work.

4.1.4. Variance & Covariance

The variance of the power spectrum monopole can be written as

$$\sigma_0^2 = \frac{1}{2} \int d\mu \frac{\tilde{P}_{\text{tot}}(k, \mu)^2}{N_{\text{modes}}}, \quad (4.16)$$

where N_{modes} denotes the number of modes per bin in k and μ in the observed field:

$$N_{\text{modes}}(k, \mu) = \frac{k^2 \Delta k \Delta \mu}{8\pi^2} V_{\text{field}}, \quad (4.17)$$

with Δk and $\Delta \mu$ corresponding to the widths of the k and μ bins respectively.

The variance of the VID has contributions due to the temperature binning of the observed signal, and cosmic variance. Assuming the temperature bins are mutually exclusive, the expected value for each bin $\langle \mathcal{B}_i \rangle = \mathcal{B}_i$, and its variance is $\sigma_{\text{bin},i}^2 = \mathcal{B}_i(1 - \mathcal{B}_i/N_{\text{vox}})$. Due to the dependence of the VID on the cosmic density field, there is an additional contribution from cosmic variance which, following Ref. [130], takes the form $\sigma_{\text{cv},i}^2 = \Upsilon_i^2 \sigma_{\text{vol}}^2 / V_{\text{vox}}^2$, where σ_{vol}^2 is the variance of the halo density field on the survey volume defined by

$$\sigma_{\text{vol}}^2 = \int \frac{d^3k}{(2\pi)^3} W_{\text{vol}}^2(k) W_{\text{vox}}^2(-k) P_h(k), \quad (4.18)$$

and we have defined

$$\Upsilon_i = \int_{\Delta T_i} dT \mathcal{P}_{\text{noise}} * \left(\sum_{N=0}^{\infty} (N - \bar{N}_h) \mathcal{P}_N(T) \mathcal{P}_{\text{Pois}}(N, \bar{N}_h) \right). \quad (4.19)$$

As such, the total variance for the VID is just the sum of these components with

$$\sigma_i^2 = \sigma_{\text{bin},i}^2 + \sigma_{\text{cv},i}^2.$$

The covariance between the power spectrum monopole and the VID can be under-

stood as the response of the measured power spectrum to the mean density perturbation. Since the VID depends on the perturbation in the number density of emitters δ_h and the power spectrum depends on two powers of the intensity fluctuation δI , the resulting covariance is proportional to the integrated bispectrum $\langle \delta_h \delta I \delta I \rangle$. As derived in Ref. [130], it is given as

$$\sigma_{B_i, P_0} = \frac{N_{\text{vox}}}{V_{\text{field}}^2} \Upsilon_i \int \frac{d^2 \Omega_{\mathbf{k}}}{4\pi} \int \frac{d^3 \mathbf{q}_1}{(2\pi)^3} \int \frac{d^3 \mathbf{q}_2}{(2\pi)^3} \int \frac{d^3 \mathbf{q}_3}{(2\pi)^3} W_{\text{vol}}(\mathbf{q}_1) W_{\text{vol}}(\mathbf{q}_2) W_{\text{vol}}(\mathbf{q}_3) \times \\ W_{\text{vox}}(-\mathbf{q}_1) W_{\text{vox}}(\mathbf{k} - \mathbf{q}_2) W_{\text{vox}}(-\mathbf{k} - \mathbf{q}_3) \langle \delta_h(-\mathbf{q}_1) \delta_I(\mathbf{k} - \mathbf{q}_2) \delta_I(-\mathbf{k} - \mathbf{q}_3) \rangle. \quad (4.20)$$

We refer the reader to Ref. [130] for the full derivation and expression for the bispectrum used in the calculation of the covariance.

Section 4.2

Line Emission Model

The formalism for computing the LIM power spectrum and VID described in the previous section can be applied to a wide variety of different target lines and models. In order to show its effectiveness we apply it to a model of an $\text{H}\alpha$ intensity map [153]. The $\text{H}\alpha$ luminosity is related to the star formation rate (SFR) via

$$L(M) = K_{\text{H}\alpha} \cdot 10^{-A_{\text{ext}}/2.5 \text{ mag}} \cdot \text{SFR}(M), \quad (4.21)$$

where $A_{\text{ext}} = 1 \text{ mag}$ corrects for dust extinction [154], and $K_{\text{H}\alpha} = 10^{41} \text{ erg/s}$ is just a proportionality constant [147]. The SFR at different redshifts is given by the formula

$$\text{SFR}(M) = 10^\alpha \left(\frac{M}{M_1} \right)^\beta \left(1 + \frac{M}{M_2} \right)^\gamma, \quad (4.22)$$

4.2 LINE EMISSION MODEL

Parameter	$z = 0.55$	$z = 1.90$	$z = 3.20$	$z = 4.52$
$\log_{10}(L_0)$	8.39	8.41	8.83	9.08
$\log_{10}(M_a/M_\odot)$	11.74	11.51	11.57	11.53
$\log_{10}(M_b/M_\odot)$	12.66	10.76	10.41	8.53
a	-1.15	-1.12	-1.03	-1.02
c	-2.18	-2.21	-2.20	-2.20

Table 4.2.1: Parameters of the $L(M)$ function given in Eq. 4.23 used in this analysis. These parameters reproduce the $L(M, z)$ functions of Ref. [153] for H α emission.

where α , β , γ , M_1 , and M_2 are free parameters [153]. Combining Eqs. (4.21) and (4.22), and redefining constants for generality, we model the relationship between line luminosity and halo mass as a power law formula

$$\frac{L_{\text{H}\alpha}}{L_\odot}(M) = L_0 \left[\left(\frac{M}{M_a} \right)^a + \left(\frac{M}{M_b} \right)^{a+1} \right]^c, \quad (4.23)$$

where L_0 , a , c , M_a , and M_b are free parameters. We determined the fiducial values of these parameters at different redshifts by fitting this model to the $L(M, z)$ relations from Ref. [153]. The best-fit values we use in our analysis are presented in 4.2.1. We also introduce a high-mass flattening of $L(M, z)$ to mimic the flattening in the SFR found in Ref. [153] for H α . For $z \leq 4$ the SFR, and hence $L(M)$, become flat for $M > 10^{13} M_\odot$. For all other redshifts, this flattening occurs for $M > 10^{12} M_\odot$. We do this by simply imposing $L(M > 10^{13} M_\odot) = L(M = 10^{13} M_\odot)$ for $z \leq 4$, and $L(M > 10^{12} M_\odot) = L(M = 10^{12} M_\odot)$ for $z > 4$. By parameterizing the mass-luminosity relation in this way, we are able to account for uncertainties in the SFR in our Fisher analysis, and model degeneracies between the astrophysics of line-emission and the cosmological parameters we consider. Finally, we assume the Tinker form for the halo mass function and halo bias [155, 156]. We emphasize that our choice of H α model is only an example and this formalism can be easily applied to a variety of models, lines, or experiments.

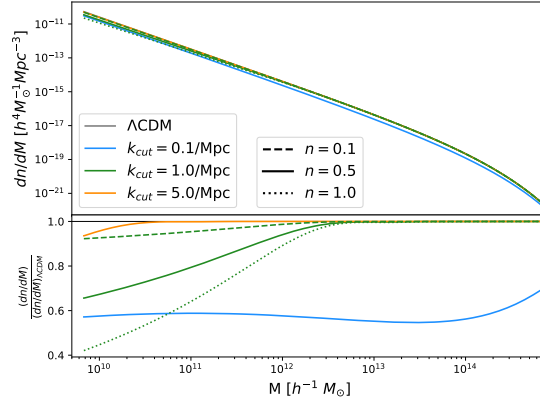


Figure 4.3.1: The Tinker halo-mass function (right) for different choices of cut-off scale k_{cut} and slope n for $\text{H}\alpha$ observed at $z = 0.55$ assuming a SPHEREx like experiment.

Section 4.3

Cosmological Models

In this section we describe the deviations from the standard ΛCDM model that we consider in this work. We choose models which alter either the large or small scale physics, where the power spectrum alone is limited, to show the capability of our joint analysis across cosmic scales. Throughout this work, we assume the standard cosmological parameters to be given by the *Planck* 2018 results with $\{\omega_b, \omega_c, n_s, \log(10^{10} A_s), h\} = \{0.02242, 0.11933, 0.9665, 0.6766\}$ [4].

4.3.1. Phenomenological non-cold dark matter

We model the small scale suppression of clustering by introducing a transfer function which cuts off the matter power spectrum at some specified scale k_{cut} . Our transfer function is given by

$$T^2(k) \equiv \frac{P_{\text{nCDM}}(k)}{P_{\text{CDM}}(k)} = \begin{cases} 1 & \text{if } k \leq k_{\text{cut}}, \\ \left(\frac{k}{k_{\text{cut}}}\right)^{-n} & \text{if } k > k_{\text{cut}}, \end{cases} \quad (4.24)$$

4.3 COSMOLOGICAL MODELS

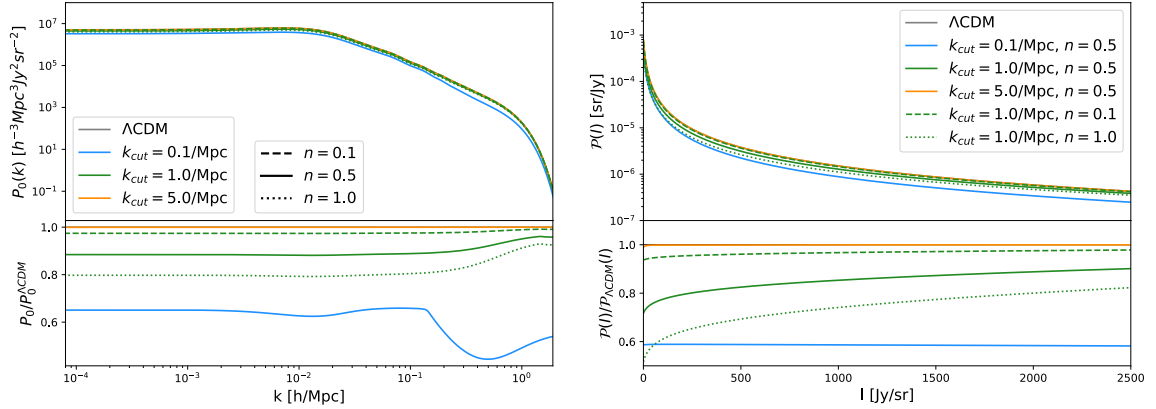


Figure 4.3.2: Monopole of the power spectrum (left), and the voxel intensity distribution (right) of the $\text{H}\alpha$ line observed at a redshift of $z = 0.55$ with an experiment like SPHEREx, as a function of cut-off scale k_{cut} and slope n . Instrumental noise is not included in either observable.

where n gives the slope or rate at which power is suppressed at small scales. We show the resulting halo-mass function in Fig. 4.3.1 and LIM observables in Fig. 4.3.2 as a function of cut-off scale and slope for an example $\text{H}\alpha$ spectral line observed at a redshift of $z = 0.55$.

From Fig. 4.3.1, we can see that the suppression in matter power at small scales decreases the number density of low-mass halos, but high-mass halo densities are unaffected (orange curve). As you begin the suppression of matter power at larger scales (green and blue curves), higher mass halos are similarly restricted. Increasing the slope of the $n\text{CDM}$ transfer function n , intuitively decreases the overall number of halos formed, with a larger effect at lower mass.

From the left hand side of Fig. 4.3.2, where we plot the IM power spectrum monopole, we can see that introducing a small-scale suppression of power has two main effects. First off, the total signal has an overall suppression relative to CDM, due to the overall suppression in the number density of halos. Secondly, at scales smaller than k_{cut} , power is sharply suppressed. This second effect is short lived, and on very small scales we see the power trend back upwards. This is because at very

4.3 COSMOLOGICAL MODELS

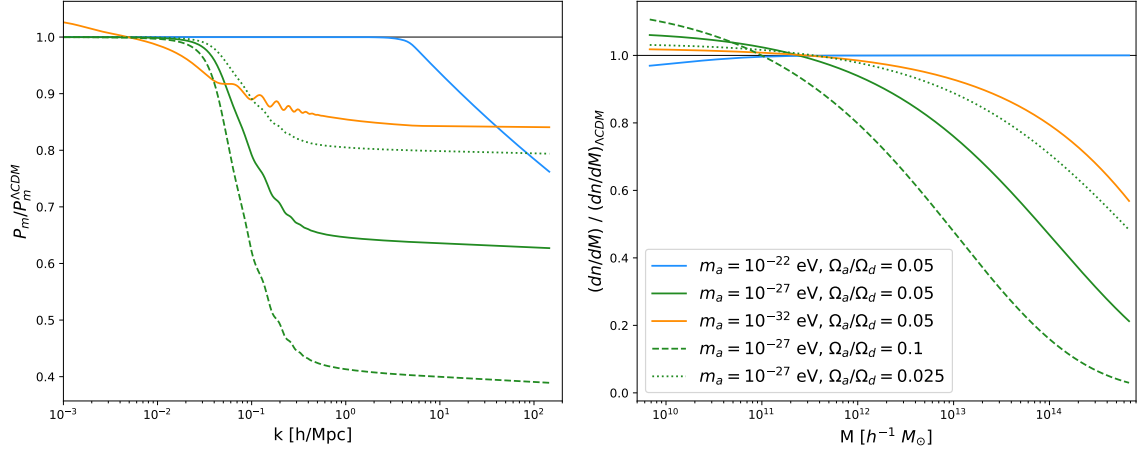


Figure 4.3.3: The ratio of the linear matter power spectrum at $z = 0$ (left) and the ratio of Tinker halo mass function (right) to those in a ΛCDM model [155] for different choices of axion mass and density fraction Ω_a/Ω_d with a fixed total dark matter density fraction Ω_d .

small scales the IM power spectrum monopole is dominated by scale-invariant shot noise, and the small-scale changes to power spectrum monopole are drowned out. Hence, for the cases with $k_{\text{cut}} = 1$ or 5 Mpc^{-1} , this effect is washed out. As the cutoff scale k_{cut} is pushed to higher scales (orange, green, to blue curves), i.e. suppression occurs for a larger range of k , the overall suppression in the signal is exacerbated. As the slope of the nCDM transfer function is increased (dashed, solid, to dotted curves), i.e. the matter power spectrum is suppressed more rapidly, the overall suppression of P_0 is similarly exacerbated. We show the probability distribution function (PDF) of the measured intensity on the right hand side of Fig. 4.3.2. Similarly to the power spectrum monopole, the main effect of introducing small scale suppression in the matter power spectrum is the introduce an overall suppression factor in the intensity PDF which roughly correlates with the suppression and enhancement seen in the HMF.

4.3 COSMOLOGICAL MODELS

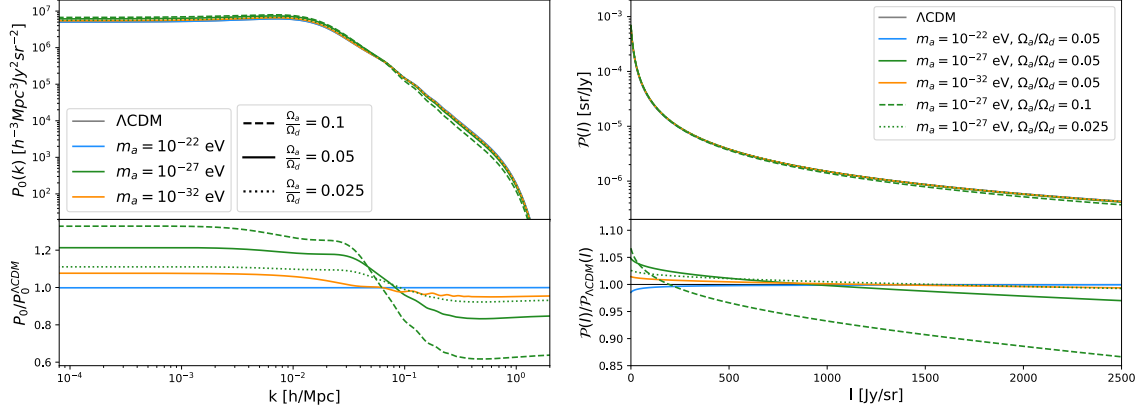


Figure 4.3.4: The power spectrum monopole $P_0(k)$ and the VID intensity PDF $\mathcal{P}(I)$ for varying axion mass and density fraction Ω_a/Ω_d for a fixed total dark matter density fraction Ω_d for an $\text{H}\alpha$ line at $z = 0.55$. The ΛCDM model is shown in gray for comparison. Instrumental noise is not considered for either observable.

4.3.2. Axionic Dark Matter

The phenomenological model described above is a good general approximation for a wide range of nCDM scenarios. However it only captures one aspect of a nCDM scenario. Physical models inherently alter the matter-power spectrum in more subtle ways. To show the ability of our method to constrain such physics, we consider the specific case of axionic dark matter.

Here we briefly review the relevant physics of axions included in `axionCAMB`², which we use to generate the matter power spectra used for our calculations of the LIM observables. For a full description of the theory behind ultralight axions see Ref. [157]. Ultralight axions (ULAs) are described by a pseudo-scalar field ϕ , which obeys the Klein-Gordon equation given in natural units by

$$\phi'' + 2\mathcal{H}\phi' + m_a^2 a^2 \phi = 0, \quad (4.25)$$

where m_a is the axion mass in units of energy, a is the cosmological scale factor,

²Publicly available at: <https://github.com/dgrin1/axionCAMB>

$\mathcal{H} = a'/a = aH$ is the conformal Hubble parameter, and primes denote derivatives with respect to conformal time. The background energy density and pressure are then given by

$$\rho_a = \frac{1}{2} \left(\frac{\phi'}{a} \right)^2 + \frac{1}{2} m_a^2 \phi^2, \quad (4.26)$$

$$p_a = \frac{1}{2} \left(\frac{\phi'}{a} \right)^2 - \frac{1}{2} m_a^2 \phi^2. \quad (4.27)$$

At early times when $m_a \ll H$, the axion field is overdamped and evolves like a cosmological constant with equation-of-state $w = -1$. As the universe cools, the axion field begins to oscillate about the minimum of its potential defining an oscillation scale factor a_{osc} when $m_a \approx 3H(a_{\text{osc}})$. From a_{osc} onwards, the number of axions is roughly conserved and the axion energy density redshifts like matter with $\rho_a \sim a^{-3}$. The relic axion density is thus $\Omega_a = \rho_a(a_{\text{osc}})a_{\text{osc}}^3/\rho_{\text{crit}}$ where ρ_{crit} is the present day critical density.

When the axion field is in its oscillatory phase one finds that the axion has a non-negligible sound speed arising from the large de Broglie wavelength of the axion:

$$c_s^2 = \frac{\frac{k^2}{4m_a^2 a^2}}{1 + \frac{k^2}{4m_a^2 a^2}}. \quad (4.28)$$

From this equation we see that at large scales $c_s^2 \rightarrow 0$, and the axions behave like pressureless CDM. However, at small scales there is an induced pressure leading to a suppression of structure in the ratio of the matter-power spectrum when compared with CDM as shown in Fig. 4.3.3 where we plot the matter power spectrum for different configurations of the axion mass and density fraction. We parameterize the axion abundance in relation to the total dark matter density with Ω_a/Ω_d and $\Omega_d = \Omega_c + \Omega_a$. Lighter mass axions ($m_a \lesssim 10^{-27}$ eV) thaw from the Hubble friction and begin oscillating during the matter or Λ -dominated eras at late times, and thus behave like

dark energy at matter-radiation equality. We call these low mass axions “DE-like”. Alternatively, heavier axions ($m_a \gtrsim 10^{-27}$ eV) begin their evolution during radiation-domination, behaving like DM much earlier on and suppress clustering below their Jeans scale. We call these axions “DM-like”. The effects of these axions are frozen into the matter-power spectrum at matter-radiation equality, leading to significantly different signatures in the LIM observables depending on the axion mass considered.

As can be expected, higher values of Ω_a/Ω_d cause more severe suppression in the matter power spectrum. For low mass axions with $m_a \sim 10^{-32}$ eV, the matter power spectrum is enhanced at very large scales, due to their dark energy like behavior (orange curve). Alternatively, high-mass axions (blue curve) behave similarly to our Λ CDM model with high k_{cut} , and only suppress power on very small scales. We show the resulting changes to the Tinker halo-mass function in the right plot of Fig. 4.3.3. Heavier axions with $m_a \sim 10^{-22}$ eV, suppress the formation of halos below their Jeans mass, thus only change the low-mass end of the HMF. Conversely, the lighter axions have a similar effect as neutrinos, providing an added radiation pressure that shifts the halo-mass function towards lighter halo masses, introducing an enhancement at low-mass, and suppression at high-mass compared to Λ CDM.

The effect of these changes to the LIM observables can be seen in Fig. 4.3.4 where we plot the LIM power spectrum monopole and VID statistic for the same variations in axion mass and density fraction. The heavier axion (blue curve), leaves the power spectrum monopole virtually unchanged as the axion DM behaves like CDM on the accessible scales. However, because of the intensity PDF’s dependence on the full luminosity function, very small scale information, which is inaccessible in the power spectrum, is made available. As such, we see percent level changes to the PDF of observed intensity at low intensities for the $m_a = 10^{-22}$ eV axion. As you shift the HMF towards lower masses, i.e. decrease the axion mass, more H α must reside in

4.3 COSMOLOGICAL MODELS

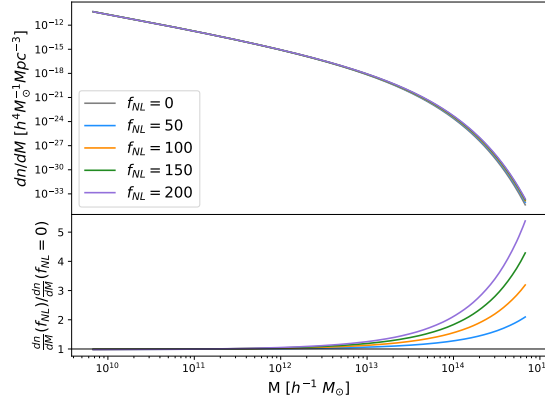


Figure 4.3.5: Tinker halo mass function dn/dM for different choices of positive f_{NL} .

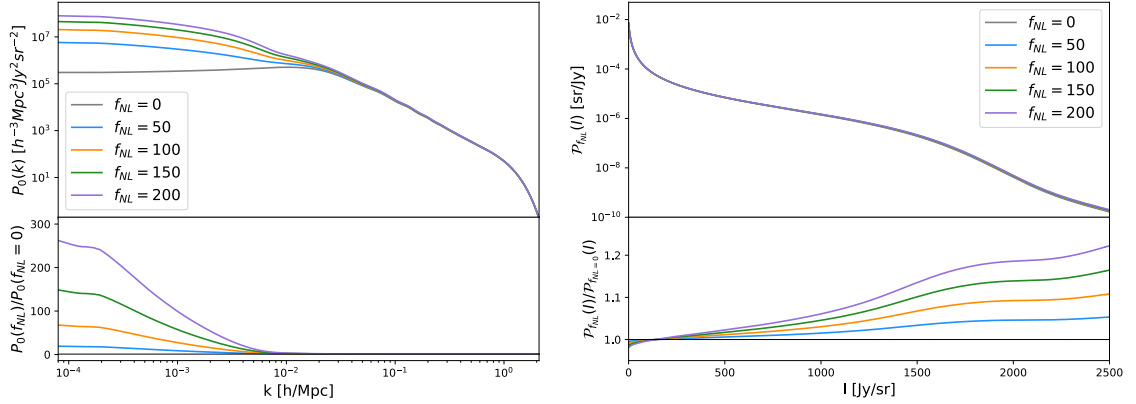


Figure 4.3.6: Power spectrum monopole (left) and the VID intensity PDF for the $H\alpha$ line observed at $z = 3.20$ as a function of f_{NL} . Instrumental noise is not considered for either observable.

each halo, increasing the average halo bias, leading to the scale-dependent imprints on both observables seen in Fig. 4.3.4. Intuitively, as you increase the axion fraction Ω_a/Ω_d , these effects become more pronounced.

4.3.3. Non-Gaussianity

In the local limit, primordial non-Gaussianity can be modelled in terms of the gauge-invariant Bardeen gravitational potential

$$\Phi = \phi + f_{NL}(\phi^2 - \langle \phi^2 \rangle) \quad (4.29)$$

where ϕ is our Gaussian random field, and f_{NL} quantifies the amount of non-Gaussianity. Note that in our notation $\Phi = -\Psi$ where Ψ is the usual Newtonian potential. With this convention, positive f_{NL} corresponds to a positive skewness of the density probability distribution $S_3(M) \equiv \langle \delta_M^3 \rangle$, and hence an increased number of massive objects. As such, any deviations from Gaussianity will modify both the halo bias and the halo mass function (HMF).

To model the effect of non-Gaussianity on the HMF, we follow Ref. [158] and use the Press-Schechter formalism [159], which we outline here. For full details of this derivation refer to Ref. [158]. In this framework, the non-Gaussian HMF in the local limit is simply the Gaussian HMF plus some non-Gaussian correction:

$$\left(\frac{dn}{dM} \right)_{NG} = \left(\frac{dn}{dM} \right)_G (1 + \Delta_{HMF}). \quad (4.30)$$

This non-Gaussian correction can be written as

$$\Delta_{HMF} = \frac{\kappa_3 H_3(\nu_c)}{6} - \frac{H_2(\nu_c)}{6} \frac{\kappa_3'}{\nu_c'}, \quad (4.31)$$

where primes denote derivatives with respect to halo mass M , $\nu_c = \sqrt{0.707} \delta_{ec} / \sigma_M = 1.42 / \sigma_M$ is a rescaling of the critical matter density for ellipsoidal collapse $\delta_{ec} = 1.686$,

and $H_n(\nu)$ are the Hermite polynomials given by

$$H_n(\nu) = (-1)^n \exp(\nu^2/2) \frac{d^n}{d\nu^n} \exp(-\nu^2/2), \quad (4.32)$$

with $\nu \equiv \delta_M/\sigma_M$. We define a normalized skewness $\kappa_3 \equiv \langle \delta_M^3 \rangle / \sigma_M^3$, where

$$\sigma_M^2 = \int \frac{d^3k}{(2\pi)^3} W_M(k) T^2(k, z) P_\Phi(k), \quad (4.33)$$

is the variance of the linear density field with $P_\Phi(k)$ being the primordial power spectrum of $\Phi(k)$. The density perturbation δ_M smoothed over a mass scale $M \equiv M_h$ is written as

$$\delta_M(z) = \int \frac{d^3k}{(2\pi)^3} W_M(k) T(k, z) \Phi(k), \quad (4.34)$$

where $T(k, z)$ is the linear matter transfer function and

$$W_M(k) = \frac{3 \sin(kR)}{(kR)^3} - \frac{3 \cos(kR)}{(kR)^2} \quad (4.35)$$

is a top-hat window function with comoving radius $R(M) = (3M/(4\pi\rho_m))^{1/3}$. In the local non-Gaussian limit, the skewness of the density probability distribution becomes

$$\begin{aligned} \langle \delta_M^3 \rangle = 6f_{NL} \int \frac{d^3k_1}{(2\pi)^3} \int \frac{d^3k_2}{(2\pi)^3} W_M(|k_1|) W_M(|k_2|) W_M(|k_1 + k_2|) \times \\ T(|k_1|) T(|k_2|) T(|k_1 + k_2|) P_\Phi(|k_1|) P_\Phi(|k_2|), \end{aligned} \quad (4.36)$$

which can be calculated numerically. We have only kept terms to first order in f_{NL} , making the correction to the HMF given in Eq. (4.31) also linear in f_{NL} . While higher-order terms exist, we neglect them following the arguments of Ref. [158]. We note that Ref. [158] introduces a cut-off scale in their calculation of the bispectrum, below which the bispectrum vanishes, in order to limit their analysis to the small-

scales which affect the formation of the low-mass galaxies they probe. To leave our work as general as possible, we do not introduce such a cut-off in our analysis.

The effects of this generalized non-Gaussian correction on the HMF can be seen in Fig. 4.3.5 where its clear that as you positively increase f_{NL} , i.e. increase the skewness, you increase the number of high mass halos. Conversely, a negative value of f_{NL} would have the opposite effect, suppressing the formation of high-mass halos.

Following Ref. [129], the total halo bias appearing in Eq. (4.3) can be written as $b_h = b_h^G + \Delta b_h$ where non-Gaussianity is introduced as a correction on the Gaussian halo bias b_h^G . In the local limit, the skewness introduced in the density probability distribution introduces a scale dependence on the halo bias giving a correction of the form

$$\Delta b_h = (b_h^G - 1)f_{NL}\delta_{ec}\frac{3\Omega_m H_0^2}{c^2 k^2 T_m(k)D(z)}, \quad (4.37)$$

where Ω_m is the matter density at $z = 0$, $T_m(k)$ is the matter transfer function, and $D(z)$ is the linear growth factor.

Introducing the corrections to the HMF given in Eq. (4.31), and the bias given in Eq. (4.37), we find that the non-Gaussian initial conditions lead to large scale enhancement in the $H\alpha$ power spectrum and high-temperature enhancement in the VID, as shown in Fig. 4.3.6. As you increase the number of high-mass halos, more $H\alpha$ is contained at larger scales, leading to the enhancement in power spectrum monopole. Similarly, more $H\alpha$ in higher mass halos leads to higher intensity $H\alpha$ distributions.

Section 4.4

IM Forecasting

In this section, we forecast the constraining power of the SPHEREx experiment for the BSM cosmologies presented in the previous section. We begin with a description

of the relevant specifications of the SPHEREx deep $H\alpha$ survey which we use to derive constraints. We then introduce the Fisher matrix formalism used in our joint forecasts, and present the results of these forecasts through constraints on all the beyond the standard model cosmological parameters we introduced in Sec. 4.3. To compute the LIM observables and all related quantities, we modify `lim`³ to account for the changes to the matter-power spectrum, halo bias, and halo mass function for each BSM cosmology we consider.

4.4.1. Experiment

To estimate the potential of a combined power spectrum and VID analysis, we forecast measurements assuming a SPHEREx mission which will measure the $H\alpha$ line with $\nu = 456805.72$ GHz [125]. The SPHEREx deep survey will cover 200 deg^2 of the sky with a single detector which has an angular resolution of $\theta_{\text{FWHM}} = 6.2 \text{ arcsec}$, and spectral resolution $\delta\nu = \nu_{\text{obs}}/41.4$. For $H\alpha$ we consider bandwidths of $\Delta\nu = \{20.95, 6.54, 3.19, 2.01\} \times 10^4 \text{ GHz}$ with noise given by $\sigma_N = \{78.9, 72.6, 57.2, 56.2\} \text{ Jy/sr}$ corresponding to emission lines with $\nu_{\text{obs}} = \{29.5, 15.7, 10.9, 8.3\} \times 10^4 \text{ GHz}$, respectively. Hence, our results are split into four redshift bins centered on redshifts of $z = \{0.55, 1.90, 3.20, 4.52\}$.

4.4.2. Fisher Matrix Forecasts

In order to study the constraining power of our $H\alpha$ emission model with the SPHEREx experiment we apply a Fisher matrix formalism. This assumes a Gaussian distribution for the parameter likelihoods centered on some chosen fiducial values. We compute the Fisher matrices for both the power spectrum monopole and voxel intensity distribution, and for a combination of these two statistics using the analytic form of their covariance described in Sec. 4.1.4.

³Available for a base Λ CDM model at: <https://github.com/jl-bernal/lim>

To obtain the joint forecast from the power spectrum and VID, we construct a vector of our observables $\Theta = [\tilde{P}_0(k), \mathcal{B}_i]$. Then, the total Fisher matrix element corresponding to parameters p_α and p_β is:

$$F_{\alpha\beta} = \frac{\partial\Theta^T}{\partial p_\alpha} \xi^{-1} \frac{\partial\Theta}{\partial p_\beta}, \quad (4.38)$$

where ξ is a block matrix diagonal elements corresponding to the variance of the power spectrum monopole and the VID, and off-diagonal elements corresponding to their covariance:

$$\xi = \begin{pmatrix} \sigma_0^2 & \sigma_{P_0, B_i} \\ \sigma_{B_i, P_0} & \sigma_i^2 \end{pmatrix} \quad (4.39)$$

where all elements have been defined in Sec. 4.1.4. Effectively, this results in a simple addition of the individual Fisher matrices for each observable, with an additional term for their covariance.

In our Fisher analyses we vary the parameters of our line emission model, $p = \{L_0, M_a, M_b, a, c\}$, along with the different BSM parameters for each case. We compute the Fisher matrix for the power spectrum monopole, VID, and their combination for all four redshift bins of the SPHEREx deep H α survey. For all forecasts we assume a k -range of $k_{\min} = 2\pi/L_{\parallel}$, representing the minimum k -accessible in the observed field, and $k_{\max} = 10 \text{ Mpc}^{-1}$, and an intensity range with $I_{\max} = 10^4 \text{ Jy/sr}$.

4.4.3. Phenomenological non-CDM

Here we present the results of our Fisher analysis on the phenomenological nCDM model presented in Sec. 4.3. We choose fiducial values of $k_{\text{cut}} = 0.1 \text{ Mpc}^{-1}$ and $n = 0.1$, giving a model which gives similar small-scale suppression to an axion-DM model with $m_a \sim 10^{-26} \text{ eV}$, and $\Omega_a/\Omega_d \sim 0.03$. As the cosmological parameters are the only common parameters across redshift, we marginalize over the parameters of our mass-

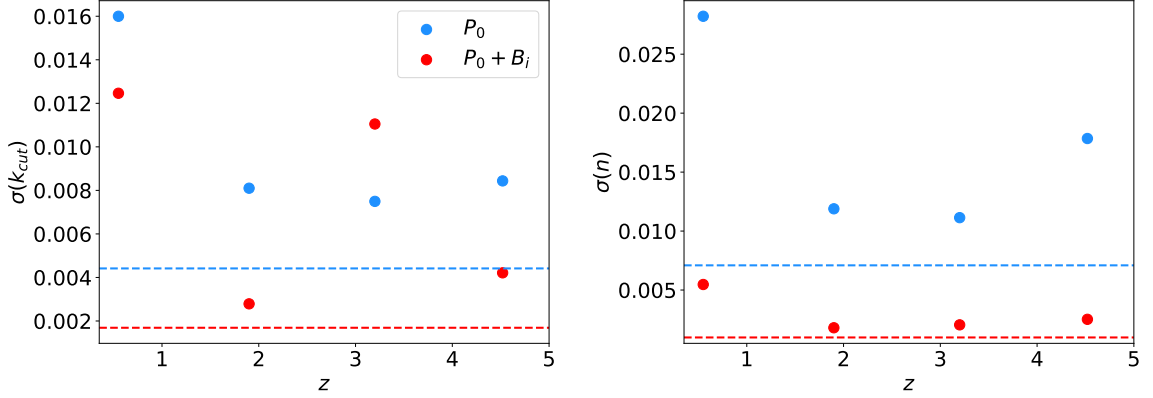


Figure 4.4.1: Marginal error on cut-off scale k_{cut} and the slope n obtained from the Fisher matrix for the power spectrum monopole P_0 and VID B_i , and their combination in the phenomenological Λ CDM model assuming fiducial values of $k_{\text{cut}} = 0.1 \text{ Mpc}^{-1}$ and $n = 0.1$.

luminosity relationship and present constraints on k_{cut} and n for each redshift bin, as well as their combination in Fig. 4.4.1. The blue points show constraints from only the power spectrum, and red points show constraints from the combination of the power spectrum and VID. The dashed lines give the combined redshift constraints, representing our final result. Including the VID in the analysis improves the constraint on k_{cut} by a factor of 2-3 with $\sigma_{P_0}(k_{\text{cut}}) = 0.0044 \text{ Mpc}^{-1}$ and $\sigma_{P_0+B_i}(k_{\text{cut}}) = 0.0017 \text{ Mpc}^{-1}$. The sensitivity to n is increased even more, improving the precision by a factor of 7, with $\sigma_{P_0}(n) = 0.007$ and $\sigma_{P_0+B_i}(n) = 0.001$.

The increase in sensitivity to these cosmological parameters is explained in Fig. 4.4.2, where we show the marginalized forecasted constraints to the $k_{\text{cut}}-n$ plane for the power spectrum monopole, VID statistic B_i , and their combination, for the $z = 0.55$ redshift bin. As we can see, the power spectrum alone is extremely sensitive to k_{cut} giving $\sigma_{P_0}(k_{\text{cut}}) = 0.016 \text{ Mpc}^{-1}$ for $z = 0.55$, a $\sim 16\%$ error on its fiducial value. Whereas, the VID finds a $\sim 74\%$ error of $\sigma_{B_i}(k_{\text{cut}}) = 0.074$ for the $z = 0.55$ redshift bin. On the other hand, the power spectrum and VID show similar sensitivity to n with $\sigma_{P_0}(n) = 0.028$ and $\sigma_{B_i}(n) = 0.025$, 28% and 25% error on their fiducial values,

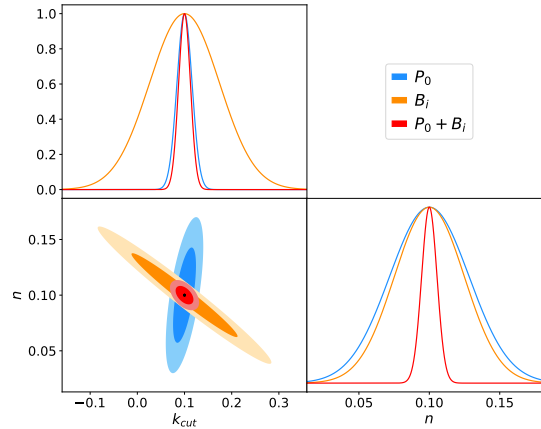


Figure 4.4.2: 68% and 95% confidence level marginalized constraints from the Fisher matrices for the power spectrum monopole P_0 and VID B_i , and their combination, on cut-off scale k_{cut} and the slope n in the phenomenological n CDM model assuming fiducial values of $k_{\text{cut}} = 0.1 \text{ Mpc}^{-1}$ and $n = 0.1$. These constraints are based on the SPHEREx deep $\text{H}\alpha$ survey at a redshift bin centered at $z = 0.55$ and marginalize over the $L(M)$ astrophysical parameters.

respectively. These differing degeneracy directions can be clearly seen in the contours in the $k_{\text{cut}}-n$ plane, where the power of a joint analysis becomes abundantly clear. Individually, the power spectrum and VID exhibit different sensitivities to the cosmological parameters, as such when they are combined, the degeneracies between k_{cut} and n in either case are broken leading to tighter constraints on both parameters.

4.4.4. Axion Dark Matter

For the axion DM model, we choose to include only the axion density fraction Ω_a/Ω_d alongside the astrophysical parameters in our Fisher analysis. We follow Refs. [145, 160–162] by forecasting constraints on the axion fraction for fixed values of $m_a \in [10^{-32}, 10^{-22}] \text{ eV}$, since a highly non-trivial degeneracy exists in the $m_a-\Omega_a$ plane. We choose three exemplary cases: first, we assume a very light axion with $m_a = 10^{-32} \text{ eV}$ as an example of “DE-like” axions; second, we choose a heavier axion with $m_a = 10^{-22} \text{ eV}$ as an example of “DM-like” axions; and finally, we choose an intermediate value

4.4 IM FORECASTING

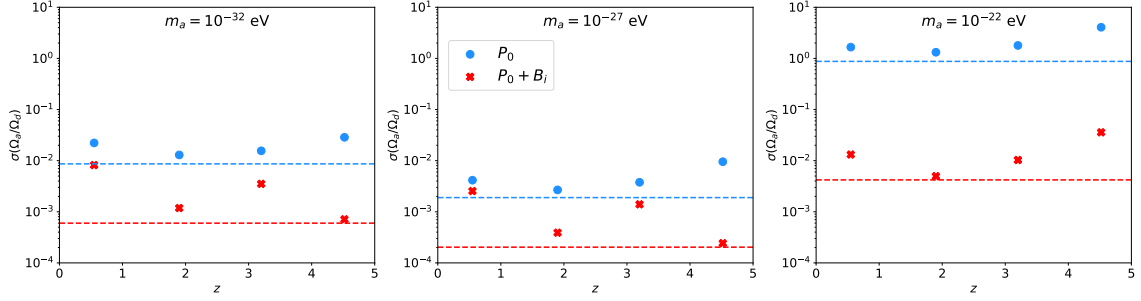


Figure 4.4.3: Marginal error on the axion fraction Ω_a/Ω_d obtained from the Fisher matrix for the power spectrum monopole P_0 and its combination with the VID B_i , for axion masses of $m_a = 10^{-32}$ eV (left), 10^{-27} eV (center), and 10^{-22} eV (right) assuming a fiducial value of $\Omega_a/\Omega_d = 0.04$.

of $m_a = 10^{-27}$ eV, to show the behavior in between these two extremes. We do not consider cases outside of this range as lighter axions are indistinguishable from a cosmological constant, and heavier axions are indistinguishable from cold dark matter on the scales we probe. We consider a fiducial value of $\Omega_a/\Omega_d = 0.04$, well within current bounds, and hold Ω_d fixed across all cases.

As we did in our phenomenological Λ CDM model, we calculate the Fisher matrices for the power spectrum monopole, VID, and their combination, and marginalize over the parameters of our mass-luminosity relationship, allowing us to combine constraints accross redshift. These marginalized constraints on Ω_a/Ω_d for the three different axion masses we consider are shown in Fig. 4.4.3 for each redshift bin, as well as their combination, which represents our final result. As expected, in each case the inclusion of the VID significantly boosts sensitivity to the axion fraction. For our “DE-like” axion with $m_a = 10^{-32}$ eV, the power spectrum alone gives $\sigma_{P_0}(\Omega_a/\Omega_d) = 0.0086$ as a combined constraint across redshift, an error of 21.6% of its fiducial value. The joint analysis including the VID brings this down to $\sigma_{P_0+B_i}(\Omega_a/\Omega_d) = 0.0006$, an improvement by a factor of over 14. Similarly for the intermediate mass axion with $m_a = 10^{-27}$ eV, the power spectrum alone gives $\sigma_{P_0}(\Omega_a/\Omega_d) = 0.0019$, whereas the joint analysis yields $\sigma_{P_0+B_i}(\Omega_a/\Omega_d) = 0.0002$, representing a 9-10 times improvement

in precision. The largest change is seen in the high-mass “DM-like” axion where $\sigma_{P_0}(\Omega_a/\Omega_d) = 0.8746$ and $\sigma_{P_0+B_i}(\Omega_a/\Omega_d) = 0.0042$, improving on the power spectrum constraint by a factor of 200.

Looking across our different axion mass examples, we see that both IM observables are most sensitive to the intermediate mass axion. This follows from the behavior we see in Fig. 4.3.4, where the intermediate mass axion has the largest effects on both the IM power spectrum monopole and intensity PDF. For the scales accessible by the power spectrum, the heavy axion behaves just like CDM, and as such the constraints on Ω_a/Ω_d are very weak and driven by the $< 5\%$ change to the $\mathcal{P}(I)$ at low intensities. Similarly to the case of the heavy axion, the lightest axion we consider changes the PDF of intensity by $< 5\%$ across the range of intensity considered. However, unlike the heavy axion, the IM power spectrum monopole shows some sensitivity to axions with $m_a = 10^{-32}$ eV. Hence, we get much better constraints than the case with $m_a = 10^{-22}$ eV. For our axion which behaves like something in between CDM and DE with $m_a = 10^{-27}$ eV, we see the most dramatic changes to the power spectrum and intensity PDF across scale and intensity, thus we obtain the tightest constraints.

4.4.5. Non-Gaussianity

Finally, we present the results of our Fisher analysis on f_{NL} , assuming a fiducial value of $f_{NL} = 0$. As before, the only common parameter across redshift is f_{NL} , so we compute the Fisher matrices for the power spectrum monopole, VID, and their combination, and then marginalize over the $L(M)$ parameters. We show our results for each redshift bin, and their combination in Fig. 4.4.4. After combining constraints at each redshift, the power spectrum alone gives $\sigma_{P_0}(f_{NL}) = 9.1$. The inclusion of the VID increases precision by a factor of 2.5, giving $\sigma_{P_0+B_i}(f_{NL}) = 3.7$. Looking at the constraints from individual redshift bins, we see that these tight constraints are mainly driven by the $z = 4.52$ redshift bin. The non-Gaussian correction to the HMF

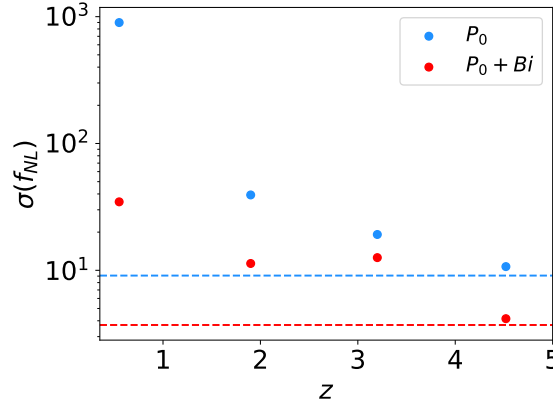


Figure 4.4.4: Marginal error on f_{NL} obtained from our joint Fisher forecast using the IM power spectrum monopole P_0 and the VID statistic B_i at each redshift bin of the SPHEREx deep H α survey. The blue points represent the constraints assuming only the power spectrum is available. The red points show the improvement when the VID is included in analysis. The dashed lines represent the total constraint when all redshift bins are combined.

we employ alters the abundance of galaxies more dramatically at high-redshifts. As such, our sensitivity to f_{NL} at low redshift is very weak with the power spectrum giving $\sigma_{P_0}(f_{NL}) = 898$ in the $z = 0.55$ bin. When the VID is included, the constraint at $z = 0.55$ is improved by a factor of over 25 with $\sigma_{P_0+B_i} = 34.7$. Looking at this individual redshift bin it becomes clear just how powerful a joint analysis including the VID can be for individual measurements.

Section 4.5

Discussion

Line-intensity mapping proposes a novel observational technique, capable of measuring large cosmological volumes at redshifts beyond the reach of conventional galaxy surveys. The fluctuations in an observed intensity map depend on the spatial distribution of galaxies and the luminosity function of the spectral line of interest. The spatial distribution of galaxies traces the underlying dark matter field, which is de-

pendent on the underlying cosmological scenario. Whereas, the luminosity function depends more heavily on the astrophysical conditions of the source. The IM power spectrum carries the bulk of cosmological information available in intensity maps, but only provides information on the shape of the line luminosity function, and is limited at large and small scales by foregrounds and survey volumes, and resolution, respectively. On the other hand, the VID which depends directly on the full luminosity function, carries non-Gaussian information, and supports a larger range of scale than the power spectrum. As such, analyses which combine these two summary statistics should significantly improve constraints on the line-luminosity function, thus breaking degeneracies between astrophysical uncertainties and cosmological features.

To combine these two summary statistics, the covariance between them is needed to properly account for their shared information content. Previous combined analyses rely on empirical estimations of the covariance from simulations, which means a joint analysis using these two statistics is only possible when simulations are available, or practical to obtain. Recent work has shown the covariance between the IM power spectrum and VID can be calculated analytically [130], opening up the possibility of combining these two statistics to evaluate the constraining power of IM experiments on a much wider range of astrophysical and cosmological models.

In this work, we use the analytic form of the covariance to forecast joint IM parameter constraints on a range of beyond the standard model cosmologies. We focus on models which alter the halo-mass function at light and heavy masses, where the inclusion of the VID has the largest impact in comparison to an analysis using only the power spectrum. Specifically, we consider local-type non-Gaussianity, which alters the HMF large scales and two cases of non-cold dark matter, which introduce a small-scale suppression of matter-power. Our DM models include a phenomenological model which generalizes the small-scale suppression of clustering with respect to CDM, and

a specific case of axion DM where we can follow its full evolution over cosmic history, giving access to tomographic information, which slightly increases our constraining power. We forecast constraints assuming a SPHEREx mission which will measure the $H\alpha$ line in its deep survey at redshifts $0.1 < z < 5$, as an example of near-term observational capabilities.

Our phenomenological non-CDM model, which models small-scale suppression of clustering through a transfer function applied to the matter-power spectrum, introduces two new cosmological parameters, the scale at which clustering begins to be suppressed k_{cut} , and the slope of the suppression n . We find that a joint Fisher analysis using the IM power spectrum monopole and VID can lead to an increase in precision on estimation of k_{cut} by a factor of 2-3, and an increase by a factor of 7 for n . The increased sensitivity is a direct result of the different $k_{\text{cut}}-n$ degeneracy directions in the power spectrum monopole and VID, making their combination break the degeneracy and yield much tighter constraints. As can be expected, we see a greater improvement in the estimation of n , as the power spectrum alone is weakly sensitive to it.

We consider three specific cases of axion dark matter with varying masses of the axion. First, we consider a “DE-like” axion with $m_a = 10^{-32}$ eV which thaws from the Hubble friction after matter-radiation equality, making its effect on the matter-power spectrum, similar to that of dark energy or massive neutrinos. In this case we find that a joint analysis increases precision on the estimation of the axion density fraction Ω_a/Ω_d by a factor of 14 with respect to an analysis using only the power spectrum. Secondly, we consider a heavy “DM-like” axion with $m_a = 10^{-22}$ eV, which becomes dynamical during the radiation era. As such, its effect on the matter power spectrum is similar to CDM, and we only see changes at very small scales which are out of reach of the IM power spectrum. For this reason, the inclusion of the VID, which is more

sensitive to these small scale changes, increases precision on Ω_a/Ω_d by a factor of 200, when compared with constraints from the power spectrum alone. The final axion we consider exists somewhere in between DE and DM with $m_a = 10^{-27}$ eV. This case is overall the most constrained of the three we consider as it has the greatest effect on both the power spectrum and VID affecting all accessible scales and intensities. Here the inclusion of the VID results in 9-10 times greater sensitivity to the the axion density.

Finally, we consider deviations to Gaussianity by introducing first order non-Gaussian corrections to the halo-mass function and halo bias. For positive (negative) f_{NL} the abundance of high-mass halos is increased (decreased) compared to a Gaussian universe. Hence, for positive (negative) f_{NL} , these corrections enhance (suppress) the power spectrum monopole and PDF of observed intensities at large scales and high intensities, respectively. These changes to the IM observables are more pronounced at high-redshift, leading to our derived constraints on f_{NL} being driven by the highest redshift bin of the SPHEREx survey. Combining redshift bins we find that our joint analysis increases sensitivity to f_{NL} by a factor of 2-3.

While we focus our forecast on a single experiment and spectral line, it can be easily generalized for others. With accurate models of the correlation between different emission lines, multiple lines could be added together to boost sensitivity to cosmological parameters even more. Furthermore, while we introduce new cosmological parameters, our analysis assumes the standard model parameters are given by the *Planck* best-fit Λ CDM cosmology. For accurate parameter estimation in BSM cosmologies, we would need to include these parameters in our Fisher forecast. The purpose of this work was to show the increased precision obtained in a joint analysis, not an accurate estimation of parameter values. Hence, we leave a full forecast with varied astrophysics and cosmology to future work.

In summary, we demonstrate how a the combination of the IM power spectrum monopole and voxel intensity distribution can increase sensitivity in IM experiments to beyond the standard model physics through the VID's control of the luminosity function of the chosen spectral line. Intensity mapping analyses using only the power spectrum of fluctuations are limited by foregrounds, survey-volumes, resolution and degeneracies between the cosmological parameters and the astrophysics of line-emission. Hence, constraints from these analyses on beyond the standard model physics are weak. The VID's sensitivity to a larger range of scale and the full-luminosity function, means that including it in analyses of BSM physics can boost the precision of parameter estimation by orders of magnitude in some cases, establishing intensity mapping as a powerful probe of new physics.

In the near future, many LIM experiments will come online, targeting a variety of emission lines sourced at redshifts reaching back to cosmic dawn. We hope this work provides a useful framework to exploit these experiments for probing beyond the standard model cosmologies.

Chapter 5

Cosmological Perturbation Theory with a Coupled Scalar-U(1) Model of Dark Energy

In this chapter, we derive all the necessary equations to describe the evolution of cosmological perturbations in a model of a cosmic acceleration consisting of a scalar field coupled to a trio of classical U(1) gauge fields. This model was first proposed in Ref. [163], where they found analytic solutions for the background evolution in this model.

Section 5.1

Background Model

Following Ref. [163], the proposed scenario consists of the standard cosmological model, with the cosmological constant replaced by a scalar field χ coupled to a classical trio of U(1) gauge fields A_μ^I via a Chern-Simons interaction, where $I = 1, 2, 3$ indexes the

different gauge fields. The Lagrangian density is given by

$$\mathcal{L} = \frac{1}{2}M_P^2 R - \frac{1}{2}(\delta\chi)^2 - V(\chi) - \frac{1}{4}F_{\mu\nu}^I F^{I\mu\nu} + \frac{\alpha}{8\pi} \frac{\chi}{f} F_{\mu\nu}^I \tilde{F}^{I\mu\nu} + \mathcal{L}_{rm} \quad (5.1)$$

where the index I is summed over, we define the Planck mass as $M_P = 1/\sqrt{8\pi G}$, and \mathcal{L}_{rm} represents the Lagrangian density for standard model radiation and matter. The field strength tensor and its dual for each gauge field is $F_{\mu\nu}^I = \partial_\mu A_\nu^I - \partial_\nu A_\mu^I$, and $\tilde{F}^{I\mu\nu} = \epsilon^{\mu\nu\alpha\beta} F_{\alpha\beta}^I / 2\sqrt{g}$, respectively. Here, $g = \det[g_{\mu\nu}]$ is the determinant of the spacetime metric, and $\epsilon^{\mu\nu\alpha\beta}$ is the anti-symmetric Levi-Civita symbol with the convention $\epsilon^{0123} = 1$, meaning all even permutations are $+1$, and all odd permutations are -1 . Another parity odd term which could be included in our Lagrangian density couples the scalar field to the gravitational Chern-Simons scalar [164]. However, this term has no effect on the background evolution or scalar perturbations so we leave its consideration to future work.

We consider a homogenous and isotropic FLRW background spacetime, with the metric $g_{\mu\nu} = a(\tau)^2 \text{diag}(-1, 1, 1, 1)$, where τ is conformal time, and the scale factor today is $a_0 = 1$. At the background level, the equations of motion for the scalar and U(1) fields are

$$-\square\chi + V_{,\chi} = \frac{1}{4M} F_{\mu\nu}^I \tilde{F}^{I\mu\nu}, \quad (5.2)$$

$$\nabla_\mu \left(F^{I\mu\nu} - \frac{\chi}{M} \tilde{F}^{I\mu\nu} \right) = 0, \quad (5.3)$$

where we have defined $M \equiv 2\pi f/\alpha$. In order to preserve homogeneity and isotropy at the background level, we assume $\chi = \chi(\tau)$, and require the U(1) fields to be set up in a flavor-space locked configuration with

$$F_{i0}^I = E(\tau)\delta_i^I, \quad F_{jk}^I = B(\tau)\epsilon_{jk}^I, \quad (5.4)$$

5.1 BACKGROUND MODEL

where $E(\tau)$ and $B(\tau)$ are vacuum-expectation-values (vevs) of the gauge fields, and latin indices i, j , and k , refer only to spatial coordinates. In this configuration, each gauge field is associated with a spatial direction such that $I = x, y, z$, and carry associated ‘electric’ and ‘magnetic’ field components that are parallel or anti-parallel to each other to avoid generating a Poynting flux which would break homogeneity. Similarly, to preserve isotropy, $E(\tau)$ and $B(\tau)$ must be equal in amplitude for each flavor.

Plugging in (5.4) into the equation of motion, and using the Bianchi identity $\nabla_{[\alpha} F_{\mu\nu]} = 0$, we find that

$$E' = \frac{B}{M}\chi', \quad B' = 0, \quad (5.5)$$

where primes denote derivatives with respect to conformal time $' = d/d\tau$. Similarly, the scalar field equation of motion becomes

$$\chi'' + 2\mathcal{H}\chi' + a^2(V_{,\chi} + 3EB/Ma^4) = 0, \quad (5.6)$$

where $\mathcal{H} = a'/a$ is the conformal Hubble parameter and we have used $F_{\mu\nu}^I \tilde{F}^{I\mu\nu} = -12EB/a^4$. The equations of motion for the electric and magnetic components tell us that

$$E = E_i + \frac{B}{M}(\chi - \chi_i), \quad B = B_i \quad (5.7)$$

where E_i , B_i and χ_i are integration constants corresponding to initial values of the fields at some time τ_i . For the rest of this work we assume $E_i = 0$ for simplicity, though the consequences of nonzero E_i are discussed in Ref. [163].

The energy density and pressure in the $U(1)$ fields in this scenario are thus

$$\rho_{U(1)} = \rho_E + \rho_B = \frac{3}{2a^4}(E^2 + B^2) = 3p_{U(1)}, \quad (5.8)$$

and the scalar field energy density has the standard form

$$\rho_\chi = \frac{1}{2} \left(\frac{\chi'}{a} \right)^2 + V(\chi). \quad (5.9)$$

Given that $B' = 0$, we can immediately see that the magnetic vev behaves just like an extra component of radiation $\rho_B = \rho_{B,0} a^{-4}$, with the present day density $\rho_{B,0} = 3B_i^2/2$.

For acceleration to occur, we need solutions for which the scalar field is potential dominated as a consequence of the gauge field interaction [163]. We define the critical solution to be the value of χ at which the potential and gauge terms cancel in the scalar field equation of motion. When χ rests at its critical solution $\chi = \chi_c$, it is trapped from its potential minimum, allowing for the potential dominated evolution which drives acceleration. Assuming a quadratic potential such that $V = \frac{1}{2}m^2\chi^2$, where m represents the mass of the scalar χ , the critical solution is defined by

$$\chi_c = \frac{\chi_i}{1+u}, \quad (5.10)$$

where we have defined

$$u = \frac{m^2 M^2}{3B_i^2} a^4 = u_0 a^4. \quad (5.11)$$

Under this critical solution, where the kinetic energy is subdominant, the energy densities in the χ field and electric vev can be combined and written as

$$\rho_{\chi E} \equiv \rho_\chi + \rho_E = \frac{m^2 \chi_i^2}{2} \frac{1}{1+u}, \quad (5.12)$$

with a joint equation of state

$$w_{\chi E} = -1 + \frac{4u}{3(1+u)}. \quad (5.13)$$

5.1 BACKGROUND MODEL

It is this combined $\rho_{\chi E}$ component that acts as dark energy in this scenario. We can see from the above equation that when $u \ll 1$, $w_{\chi E}$ will yield an equation of state very close to -1 , and behave like a cosmological constant. As $u \rightarrow 1$, $w_{\chi E} \rightarrow -\frac{1}{3}$, marking the end of acceleration. Note that $w_{\chi E}$ is not simply an addition of a radiation-like component with $w = 1/3$ and a scalar component with $w = -4/3(1 + u)$, but the equation of state for the coupled χ - E fluid, which together acts as dark energy.

We can enforce the kinetic energy of the scalar field to be subdominant when $R_\chi \ll 1$, where

$$R_\chi = \frac{\chi'_c/2a^2}{m^2\chi_c^2/2} = \left(-\frac{4\mathcal{H}}{am} \frac{u}{1+u} \right)^2 = R_{\chi,0} \left(\frac{1+u_0}{\mathcal{H}_0} \frac{\mathcal{H}a^3}{1+u} \right)^2 \quad (5.14)$$

is the ratio of the scalar field kinetic and potential energies, and where in the last equality we have defined this ratio at the present day $R_{\chi,0}$, which is a free parameter in this model. With reasonable assumptions about the background expansion history, Ref. [163] uses this to place a lower bound on $m \gg \sqrt{12}H_0$ when $u = 1$. This bound ensures that the kinetic contribution to both the energy density and equation of state are subdominant to those of the E vev. We can also use the kinetic to potential energy ratio to separate out the equation of state evolution of the χ - E fluid, where it is simple to show that

$$w_\chi = \frac{1 - R_\chi}{1 + R_\chi}, \quad (5.15)$$

and we know from (5.8) that $w_E = 1/3$.

To set the various parameters of this model, it is useful to redefine our parameters in terms of well understood phenomenological parameters. We begin by redefining the energy density in the B vev as a fraction of the density of standard model radiation

5.1 BACKGROUND MODEL

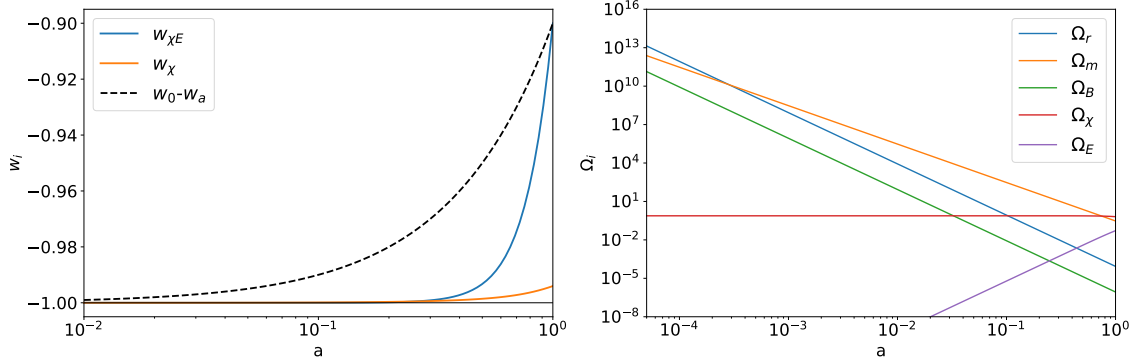


Figure 5.1.1: Left: the evolution of the equation of state of the scalar field (orange) and dark energy (blue). The dashed line shows a w_0 - w_a model with $w_0 = -0.9$ and $w_a = 0.1$ for comparison. Right: the evolution of energy densities for all components of the cosmic fluid. Both plots are generated with $\Omega_{\chi E,0} = 0.7$, $w_{\chi E,0} = -0.9$, $R_{B,0} = 0.01$, and $R_{\chi,0} = 0.003$.

such that $\rho_B = R_{B,0}\rho_r$. Next, using (5.11)-(5.14), we find

$$u_0 = \frac{3(1 + w_{\chi E,0})}{1 - 3w_{\chi E,0}}, \quad (5.16)$$

$$\frac{m}{H_0} = \frac{3(1 + w_{\chi E,0})}{\sqrt{R_{\chi,0}}}, \quad (5.17)$$

$$\left(\frac{\chi_i}{M_P}\right)^2 = \frac{8R_{\chi,0}\Omega_{\chi E,0}}{(1 - 3w_{\chi E,0})(1 + w_{\chi E,0})^2}, \quad (5.18)$$

$$\left(\frac{M}{M_P}\right)^2 = \frac{2R_{B,0}\Omega_{r,0}R_{\chi,0}}{(1 - 3w_{\chi E,0})(1 + w_{\chi E,0})}, \quad (5.19)$$

where $w_{\chi E,0}$, and $\Omega_{\chi E,0}$ are the present day dark-energy equation of state, and fractional density, respectively. In Figure 5.1.1 we show the background evolution of the dark energy, scalar field equation of state, and the energy densities of all components in this model for a sample case in which the χ - E fluid acts as dark energy.

Section 5.2

Scalar Perturbations

Dark energy described by a cosmological constant has no scalar perturbations to keep track of. However, for the multi-field model we consider, including the evolution of scalar perturbations will be key to accessing its viability against cosmological datasets. To derive the scalar perturbations in this model we begin by perturbing the spacetime in the flat-slicing gauge such that

$$g_{\mu\nu} = a^2 \begin{pmatrix} -1 + 2\Phi_F(\tau, z) & 0 & 0 & \partial_z b(\tau, z) \\ 0 & 1 & 0 & 0 \\ 0 & 0 & 1 & 0 \\ \partial_z b(\tau, z) & 0 & 0 & 1 \end{pmatrix}, \quad (5.20)$$

where we perform a coordinate rotation such that the Fourier vector points along the $+z$ axis, i.e. $\vec{k} = k\hat{z}$, so perturbations to the spacetime metric and gauge fields will be functions of τ and z only. Throughout this section, Φ_F and b represent the perturbations to the spacetime metric in the flat-slicing gauge. The scalar field is perturbed such that $\chi(\tau) \rightarrow \chi(\tau) + \delta\chi(\tau, z)$ and we write the most general gauge field perturbations constructed using only scalar degrees of freedom:

$$\delta A_0^I = \delta^{Ii} \partial_i Y', \quad \delta A_i^I = \delta_i^I Q + \delta^{Ij} \partial_i \partial_j \delta M + \epsilon^{Ij} \partial_j P, \quad (5.21)$$

where Y , Q , δM , and P are unknown scalars. Note that at the background level, $A_0^I = 0$, but there is still gauge freedom for a nonzero component at the perturbative level. Using these definitions the perturbations to the field strength tensor are

$$\delta F_{0i}^I = \delta_i^I Q' + \delta^{Ij} \partial_i \partial_j (\delta M' - Y') - \epsilon^{Ij} \partial_j P', \quad \delta F_{ij}^I = 2\delta_{[j}^I \partial_{i]} Q + 2\epsilon^{Ik}{}_{[i} \partial_{j]} \partial_k P. \quad (5.22)$$

Plugging these perturbed fields into the equations of motion defined in (5.3), we find:

$$P'' + k^2 P = B\Phi_F - Bb' - \frac{E}{M}\delta\chi - \frac{\chi'}{M}Q \quad (5.23)$$

$$Q'' + k^2 Q = E\Phi_F' + Ek^2 b + \frac{B}{M}\chi'\Phi_F - \frac{B}{M}\delta\chi' - k^2 \frac{\chi'}{M}P \quad (5.24)$$

$$k^2(\delta M' - Y') = Q' - E\Phi_F + \frac{B}{M}\delta\chi, \quad (5.25)$$

and similarly for the scalar field we find:

$$\begin{aligned} \delta\chi'' + 2\mathcal{H}\delta\chi' + k^2\delta\chi + a^2 V_{,\chi\chi}\delta\chi = & -\chi'\Phi_F' - k^2\chi'b + 2a^2 V_{,\chi}\Phi_F - 2\frac{E}{a^2 M}k^2 P \\ & + \frac{B}{a^2 M}(3Q' - k^2(\delta M' - Y')) + 3\frac{EB}{a^2 M}\Phi_F, \end{aligned} \quad (5.26)$$

where in both cases we have Fourier transformed such that $\nabla^2 \rightarrow k^2$.

To linear order in perturbations, the stress-energy tensor is given by

$$T^0_0 = -(\rho + \delta\rho), \quad (5.27)$$

$$ik^i T^0_i = -(\rho + p)\theta, \quad (5.28)$$

$$T^i_j = -(p + \delta p)\delta^i_j + \Sigma^i_j, \quad (5.29)$$

where $\delta\rho$ is the density perturbation, δp is the pressure perturbation, and $\theta = ik^j v_j$ is the divergence of the fluid velocity. In the final equation, $\Sigma^i_j \equiv T^i_j - \delta^i_j T^k_k/3$ denotes the traceless component of T^i_j and is related to the anisotropic shear perturbation via $(\rho + p)\sigma \equiv -(\hat{k}_i \hat{k}_j - \frac{1}{3}\delta_{ij})\Sigma^i_j$ [91]. Using these definitions, and calculating the stress-energy tensor for our added field components allows us to recast (5.23)-(5.26) in terms of fluid variables for the electric and magnetic vevs and our scalar field. The total fluid perturbations are divided up among the three components giv-

ing:

$$\begin{aligned}
 \delta\rho &= \frac{1}{a^4}(2E^2\Phi_F - 2EQ' + 2k^2BP + \frac{EB}{M}\delta\chi) + V_{,\chi}\delta\chi + \frac{1}{a^2}(\chi'\delta\chi' + \chi'^2\Phi_F) \\
 \delta\rho_E &= \frac{1}{a^4}(2E^2\Phi_F - 2EQ') + \frac{EB}{a^4M}\delta\chi \\
 \delta\rho_B &= \frac{1}{a^4}2k^2BP \\
 \delta\rho_\chi &= V_{,\chi}\delta\chi + \frac{1}{a^2}(\chi'\delta\chi' + \chi'^2\Phi_F),
 \end{aligned} \tag{5.30}$$

for the total density perturbation $\delta\rho$, and

$$\begin{aligned}
 \delta p &= \frac{1}{3a^4}(2E^2\Phi_F - 2EQ' + 2k^2BP + \frac{EB}{M}\delta\chi) - V_{,\chi}\delta\chi + \frac{1}{a^2}(\chi'\delta\chi' + \chi'^2\Phi_F) \\
 \delta p_E &= \frac{1}{3}\delta\rho_E \\
 \delta p_B &= \frac{1}{3}\delta\rho_B \\
 \delta p_\chi &= -V_{,\chi}\delta\chi + \frac{1}{a^2}(\chi'\delta\chi' + \chi'^2\Phi_F),
 \end{aligned} \tag{5.31}$$

for the total pressure perturbation δp . Similarly, the velocity divergence or momentum density perturbation is

$$\begin{aligned}
 (\rho + p)\theta &= -2\frac{k^2}{a^4}(EQ + BP' + B^2b) + \frac{k^2}{a^2}\chi'\delta\chi \\
 (\rho + p)\theta_E &= -2\frac{k^2}{a^4}EQ \\
 (\rho + p)\theta_B &= -2\frac{k^2}{a^4}(BP' + B^2b) \\
 (\rho + p)\theta_\chi &= \frac{k^2}{a^2}\chi'\delta\chi.
 \end{aligned} \tag{5.32}$$

And finally, the anisotropic shear is

$$\begin{aligned}
 (\rho + p)\sigma &= -\frac{2}{3a^4}(2E^2\Phi_F - 2EQ' + 2k^2BP) + \frac{4}{3}\frac{EB}{a^4M}\delta\chi \\
 (\rho + p)\sigma_E &= -\frac{2}{3}\delta\rho_E + \frac{2EB}{k^2a^2M\chi'}(\rho + p)\theta_\chi \\
 (\rho + p)\sigma_B &= -\frac{2}{3}\delta\rho_B \\
 (\rho + p)\sigma_\chi &= 0.
 \end{aligned} \tag{5.33}$$

Using these equalities we can now recast the equations of motion in terms of these phenomenological fluid variables. It will be useful to define

$$\Gamma_E \equiv \frac{E'}{E} = \frac{4\mathcal{H}}{1+u} \tag{5.34}$$

as an inverse time scale that characterizes the flow of energy between the E and χ fluids. First off, we find that the shear components obey the following equations of state:

$$\sigma_B = -\frac{1}{2}\delta_B, \quad \sigma_E = -\frac{1}{2}\delta_E + \frac{\Gamma_E}{k^2}\theta_\chi, \tag{5.35}$$

where $\delta_i = \delta\rho_i/\rho_i$ is the density contrast in each fluid. The scalar field pressure perturbation obeys a gauge-invariant equation of state given by

$$\delta p_\chi = \delta\rho_\chi + \frac{p'_\chi - \rho'_\chi}{k^2}\theta_\chi \tag{5.36}$$

where

$$\rho'_\chi + 3\mathcal{H}(\rho_\chi + p_\chi) + 2\Gamma_E\rho_E = 0, \quad \frac{p'_\chi - \rho'_\chi}{\rho_\chi} = w'_\chi + (1 - w_\chi) \left(3\mathcal{H}(1 + w_\chi) + 2\Gamma_E\frac{\rho_E}{\rho_\chi} \right). \tag{5.37}$$

The B equations of motion are

$$\delta'_B + \frac{4}{3}(\theta_B + k^2 b) = 0, \quad \theta'_B = k^2 \left(\frac{1}{4} \delta_B - \Phi_F - \sigma_B \right) + \Gamma_E \frac{\rho_E}{\rho_B} (\theta_\chi - \theta_E). \quad (5.38)$$

The E equations are

$$\delta'_E + \frac{4}{3}(\theta_E + k^2 b) + \Gamma_E (\delta_E - \delta_B - \delta R_\chi + 2\Phi_F) = 0, \quad \theta'_E = k^2 \left(\frac{1}{4} \delta_E - \Phi_F - \sigma_E \right) - \Gamma_E \left(\theta_E - \frac{1}{2} \theta_\chi \right), \quad (5.39)$$

where $\delta R_\chi = (\delta \rho_\chi + \delta p_\chi) / (\rho_\chi + p_\chi)$. Finally, the equations of motion for the scalar field become,

$$\theta'_\chi = 2\mathcal{H}\theta_\chi + \frac{k^2}{1 + w_\chi} \delta_\chi - k^2 \Phi_F + 2\Gamma_E \frac{\rho_E}{\rho_\chi} \frac{1}{1 + w_\chi} \theta_\chi \quad (5.40)$$

and

$$\begin{aligned} \delta'_\chi + (1 + w_\chi)(\theta_\chi + k^2 b) + 3\mathcal{H} \left(\frac{\delta p_\chi}{\delta \rho_\chi} - w_\chi \right) \delta_\chi \\ + \Gamma_E \frac{\rho_E}{\rho_\chi} \left\{ \left[\frac{1}{1 + w_\chi} \left(\frac{\delta p_\chi}{\delta \rho_\chi} - w_\chi \right) - 1 \right] \delta_\chi + \delta_E + \delta_B - 2\Phi_F \right\} = 0. \end{aligned} \quad (5.41)$$

The equations of motion outlined in (5.34)-(5.41) constitute a full description of the perturbative sector dynamics in the flat-slicing gauge in this dark energy model built from a scalar field coupled to a trio of classical U(1) gauge fields.

5.2.1. Gauge Transformations

In order to access the viability of this proposed model against cosmological datasets, the background and perturbative evolution of all new fluid components must be evolved alongside the standard model components. We choose to do this evolution in the Boltzmann solver **CAMB**¹ [95], which evolves the linearized perturbations in the

¹Publicly available at: <https://camb.info>

synchronous gauge. As such, we must transform all the equations of motion derived in the previous section to the synchronous gauge to be compatible with the rest of the code. We do this in a two step process. First, we transform from the flat-slicing gauge with metric perturbations Φ_F and b , to the conformal-Newtonian gauge with metric perturbations ϕ and ψ . Second, we transform from the conformal-Newtonian to the synchronous gauge with metric perturbations h and η , as laid out in Ref. [91].

Linear Perturbations in the Conformal Newtonian Gauge. The line-element in the conformal-Newtonian gauge is

$$ds^2 = a^2(t) \left[-(1 + 2\psi)dt^2 + (1 - 2\phi)d\vec{x}^2 \right]. \quad (5.42)$$

The flat-slicing and conformal-Newtonian gauge metric potentials are related as follows:

$$\phi = -\mathcal{H}b, \quad \psi = b' + \mathcal{H}b - \Phi_F, \quad (5.43)$$

which make the fluid variables transform as

$$\delta_F = \delta_{CN} - \frac{\rho'}{\rho}b, \quad \theta_F = \theta_{CN} - k^2b, \quad \delta p_F = \delta p_{CN} - p'b, \quad \sigma_F = \sigma_{CN}, \quad (5.44)$$

where we use the subscripts F and CN to refer to quantities in the flat-slicing and conformal-Newtonian gauges, respectively.

Completing these transformations, the scalar field fluid equations of motion in the conformal-Newtonian gauge can be written as

$$\begin{aligned} \delta'_\chi = & -(1 + w_\chi)\theta_\chi - 3\mathcal{H} \left(\frac{\delta p_\chi}{\delta \rho_\chi} - w_\chi \right) \delta_\chi + 3(1 + w_\chi)\phi' \\ & - \Gamma_E \frac{\rho_E}{\rho_\chi} \left\{ \left[\frac{1}{1 + w_\chi} \left(\frac{\delta p_\chi}{\delta \rho_\chi} - w_\chi \right) - 1 \right] \delta_\chi + \delta_E + \delta_B + 2\psi \right\} \end{aligned} \quad (5.45)$$

$$\theta'_\chi = 2\mathcal{H}\theta_\chi + \frac{k^2}{1+w_\chi}\delta_\chi + 2\Gamma_E \frac{\rho_E}{\rho_\chi} \frac{1}{1+w_\chi}\theta_\chi + k^2\psi, \quad (5.46)$$

$$\sigma_\chi = 0. \quad (5.47)$$

The scalar field pressure perturbation is gauge-invariant and thus unchanged during the transformation. The fluid equations for the E -component become

$$\delta'_E = -\frac{4}{3}\theta_E - \Gamma_E (\delta_E - \delta_B - \delta R_\chi - 2\psi) + 4\phi', \quad (5.48)$$

$$\theta'_E = k^2 \left(\frac{1}{4}\delta_E + \psi - \sigma_E \right) - \Gamma_E \left(\theta_E - \frac{1}{2}\theta_\chi \right), \quad (5.49)$$

$$\sigma_E = -\frac{1}{2}\delta_E + \frac{\Gamma_E}{k^2}\theta_\chi + 2\phi. \quad (5.50)$$

And finally, the fluid equations for the B -component in the conformal-Newtonian gauge are

$$\delta'_B = -\frac{4}{3}\theta_B + 4\phi', \quad (5.51)$$

$$\theta'_B = k^2 \left(\frac{1}{4}\delta_B + \psi - \sigma_B \right) + \Gamma_E \frac{\rho_E}{\rho_B} (\theta_\chi - \theta_E), \quad (5.52)$$

$$\sigma_B = -\frac{1}{2}\delta_B + 2\phi \quad (5.53)$$

Linear Perturbations in the Synchronous Gauge. Following Ref. [91], the synchronous gauge is defined via the spacetime metric

$$g_{\mu\nu} = \text{diag}[-a^2, a^2(1-2\eta), a^2(1-2\eta), a^2(1+h+4\eta)], \quad (5.54)$$

and the conformal-Newtonian and synchronous gauge metric potentials are related as follows:

$$\phi_{CN} = \eta - \alpha\mathcal{H}, \quad \psi_{CN} = \alpha' + \alpha\mathcal{H}, \quad (5.55)$$

where $\alpha = (h' + 6\eta')/2k^2$. The fluid variables transform as

$$\delta_{CN} = \delta_S + \alpha \frac{\rho'}{\rho}, \quad \theta_{CN} = \theta_S + \alpha k^2, \quad \delta p_{CN} = \delta p_S + \alpha p', \quad \text{and} \quad \sigma_{CN} = \sigma_S, \quad (5.56)$$

where the subscript S denotes quantities in the synchronous gauge.

Completing the transformation from the conformal-Newtonian to synchronous gauge result in the scalar field equations of motion becoming

$$\begin{aligned} \delta'_\chi = & -(1 + w_\chi) \left(\theta_\chi + \frac{h'}{2} \right) - 3\mathcal{H} \left(\frac{\delta p_\chi}{\delta \rho_\chi} - w_\chi \right) \delta_\chi \\ & - \Gamma_E \frac{\rho_E}{\rho_\chi} \left\{ \left[\frac{1}{1 + w_\chi} \left(\frac{\delta p_\chi}{\delta \rho_\chi} - w_\chi \right) - 1 \right] \delta_\chi + \delta_E + \delta_B \right\}, \end{aligned} \quad (5.57)$$

$$\theta'_\chi = 2\mathcal{H}\theta_\chi + \frac{k^2}{1 + w_\chi} \delta_\chi + 2\Gamma_E \frac{\rho_E}{\rho_\chi} \frac{1}{1 + w_\chi} \theta_\chi, \quad (5.58)$$

$$\sigma_\chi = 0. \quad (5.59)$$

As before, the scalar field pressure perturbation is gauge-invariant and unchanged.

The E -component equations in the synchronous gauge are:

$$\delta'_E = -\frac{4}{3} \left(\theta_E + \frac{h'}{2} \right) - \Gamma_E (\delta_E - \delta_B - \delta R_\chi), \quad (5.60)$$

$$\theta'_E = k^2 \left(\frac{1}{4} \delta_E - \sigma_E \right) - \Gamma_E \left(\theta_E - \frac{1}{2} \theta_\chi \right), \quad (5.61)$$

$$\sigma_E = -\frac{1}{2} \delta_E + \frac{\Gamma_E}{k^2} \theta_\chi + 2\eta. \quad (5.62)$$

And finally, the B -component equations of motion transform into:

$$\delta'_B = -\frac{4}{3} \left(\theta_B + \frac{h'}{2} \right), \quad (5.63)$$

$$\theta'_B = k^2 \left(\frac{1}{4} \delta_B - \sigma_B \right) + \Gamma_E \frac{\rho_E}{\rho_B} (\theta_\chi - \theta_E), \quad (5.64)$$

$$\sigma_B = -\frac{1}{2} \delta_B + 2\eta. \quad (5.65)$$

To determine the impact of this model of dark energy on cosmological observables, like the cosmic microwave background, one must numerically solve this coupled system of linear perturbations alongside the standard model components.

Section 5.3

Initial Conditions

Solving the coupled set of first-order differential equations derived in the previous section requires specifying initial conditions for the metric potentials and fluid components. Following the derivation of initial conditions in Ref. [91], we begin evolution deep in the radiation era and consider only the behavior in the synchronous gauge, though we note that the behavior of fluctuations on scales larger than the horizon is gauge-dependent. During radiation domination, massive neutrinos are relativistic and behave as radiation, alongside the new B -component coming from our three $U(1)$ fields, and of course photons. The cold dark matter (CDM), baryons, scalar field χ , and E -component make a negligible contribution to the total energy density of the Universe such that $\rho_{tot} = \rho_\gamma + \rho_\nu + \rho_B$. Note that throughout this section we will use the subscript B to refer to our added B -field component, and the subscript b to refer to baryons. The expansion rate during radiation domination is $\mathcal{H} = a'/a = \tau^{-1}$. Furthermore, large Thompson damping drives $\ell \geq 2$ moments of the Boltzmann hierarchy for photons, and $\ell \geq 3$ moments for neutrinos to zero. Under these assumptions

5.3 INITIAL CONDITIONS

Einstein's equations² give us

$$k^2\eta - \frac{1}{2}\mathcal{H}h' = \frac{3}{2}\mathcal{H}^2\frac{\delta\rho_{tot}}{\rho_{tot}}, \quad (5.66)$$

$$k^2\eta' = \frac{3}{2}\mathcal{H}^2\frac{[(\rho+p)\theta]_{tot}}{\rho_{tot}}, \quad (5.67)$$

$$h'' + 2\mathcal{H}h' - 2k^2\eta = -3\mathcal{H}^2\frac{\delta\rho_{tot}}{\rho_{tot}}, \quad (5.68)$$

$$h'' + 6\eta'' + 2\mathcal{H}(h' + 6\eta') - 2k^2\eta = -9\mathcal{H}^2\frac{[(\rho+p)\sigma]_{tot}}{\rho_{tot}} \quad (5.69)$$

where $\delta\rho_{tot} = \delta\rho_\gamma + \delta\rho_\nu + \delta\rho_B$. Combining the first and third of these equations and simplifying gives a second-order differential equation for the metric perturbation h :

$$\tau^2 h'' + \tau h' + 6[(1 - R_\nu - R_B)\delta_\gamma + R_\nu\delta_\nu + R_B\delta_B] = 0, \quad (5.70)$$

where we have defined $R_i = \rho_i/\rho_{tot}$. The equations of motion for the fluid perturbations relevant in the radiation era simplify to

$$\delta'_\gamma + \frac{4}{3}\theta_\gamma + \frac{2}{3}h' = 0, \quad \theta'_\gamma - \frac{1}{4}k^2\delta_\gamma = 0, \quad (5.71)$$

$$\delta'_\nu + \frac{4}{3}\theta_\nu + \frac{2}{3}h' = 0, \quad \theta'_\nu - \frac{1}{4}k^2(\delta_\nu - 4\sigma_\nu) = 0, \quad \sigma'_\nu = \frac{2}{15}(2\theta_\nu + h' + 6\eta'), \quad (5.72)$$

$$\delta'_B + \frac{4}{3}\theta_B + \frac{2}{3}h' = 0, \quad \theta'_B - \frac{1}{4}k^2(\delta_B - 4\sigma_B) = 0, \quad \sigma'_B = \frac{1}{3}(2\theta_B + h' + 6\eta'), \quad (5.73)$$

where we have used the fact that $\rho_B \gg \rho_E$ early on. To lowest order in $k\tau$, all k^2 terms in these equations can be dropped. Under those assumptions, taking two derivatives with respect to conformal time of (5.70)-(5.73), gives

$$\tau^2 h'''' + 5\tau h''' = 0, \quad (5.74)$$

²In Ref. [91], these are equations (21a)-(21d) adjusted for radiation domination.

5.3 INITIAL CONDITIONS

This equation has power law solutions with powers $n = 0, 1, 2, -2$, giving

$$h = A + B(k\tau)^{-2} + C(k\tau)^2 + D(k\tau). \quad (5.75)$$

Plugging this solution into (5.70) tells us that

$$\delta \equiv (1 - R_\nu - R_B)\delta_\gamma + R_\nu\delta_\nu + R_B\delta_B = -\frac{2}{3}B(k\tau)^{-2} - \frac{2}{3}C(k\tau)^2 - \frac{1}{6}D(k\tau). \quad (5.76)$$

We now choose initial conditions where only the fastest growing mode is present giving us:

$$h = C(k\tau)^2, \quad \delta = -\frac{2}{3}C(k\tau)^2. \quad (5.77)$$

Using our solutions for δ and h to simplify (5.66), gives a solution for our other metric perturbation η :

$$\eta = 2C + D(k\tau)^{-1}. \quad (5.78)$$

Assuming adiabatic initial conditions, $\delta_\gamma/(1 + w_\gamma) = \delta_i/(1 + w_i)$ meaning that

$$\delta_\gamma = \delta_\nu = \delta_B = \delta_E = -\frac{2}{3}C(k\tau)^2, \quad (5.79)$$

$$\delta_b = \delta_c = \frac{3}{4}\delta_\gamma, \quad (5.80)$$

$$\delta_\chi = \frac{3}{4}(1 + w_\chi)\delta_\gamma. \quad (5.81)$$

The equation of motion for θ_γ tells us that

$$\theta_\gamma = -\frac{1}{18}Ck^4\tau^3. \quad (5.82)$$

From (5.67), we see that η' must scale as θ_γ/τ^2 , so we need to take up to second order

5.3 INITIAL CONDITIONS

in $k\tau$ in our definition of η , i.e. $D \rightarrow H(k\tau)^3$, giving

$$\eta = 2C + H(k\tau)^2. \quad (5.83)$$

Let us now assume that all θ perturbations scale in the same way such that $\theta_\nu = R_1\theta_\gamma$ and $\theta_B = R_2\theta_\gamma$. Plugging these into (5.67) then gives

$$H = -\frac{1}{18}C(1 - R_\nu - R_B + R_\nu R_1 + R_B R_2). \quad (5.84)$$

The equations of motion for the neutrinos, E -, and B -components anisotropic shear tell us that $\sigma_\nu \propto \sigma_B \propto \sigma_E \propto (k\tau)^2$. So let us define $\sigma_\nu = S_1(k\tau)^2$, and $\sigma_B = S_2(k\tau)^2$. Using these definitions and the shear equations of motion we find that

$$S_1 = \frac{2}{15}(C + 6H), \quad S_2 = \frac{1}{3}(C + 6H). \quad (5.85)$$

The equations of motion for θ_ν and θ_B similarly give us

$$-\frac{3}{18}R_1C = \frac{1}{4}\left(-\frac{2}{3}C - 4S_1\right), \quad -\frac{3}{18}R_2C = \frac{1}{4}\left(-\frac{2}{3}C - 4S_2\right). \quad (5.86)$$

We now have a system of five equations with five unknowns H , R_1 , R_2 , S_1 , and S_2 .

Solving this system gives

$$\eta = 2C - \frac{5 + 4R_\nu + 10R_B}{6(15 + 4R_\nu + 10R_B)} C(k\tau)^2 \quad (5.87)$$

$$\theta_\nu = \frac{23 + 4R_\nu + 10R_B}{15 + 4R_\nu + 10R_B} \theta_\gamma \quad (5.88)$$

$$\theta_B = \frac{35 + 4R_\nu + 10R_B}{15 + 4R_\nu + 10R_B} \theta_\gamma \quad (5.89)$$

$$\sigma_\nu = \frac{4}{3(15 + 4R_\nu + 10R_B)} C(k\tau)^2 \quad (5.90)$$

$$\sigma_B = \frac{10}{3(15 + 4R_\nu + 10R_B)} C(k\tau)^2 = \frac{5}{2} \sigma_\nu. \quad (5.91)$$

Next, we need to find the initial conditions for θ_E , θ_χ , and σ_E . Let us assume as we did for the other components that $\theta_E = R_3 k^4 \tau^3$, $\theta_\chi = R_4 k^4 \tau^3$, and $\sigma_E = S_3 (k\tau)^2$. Early on, $\Gamma_E = 4\mathcal{H} = 4/\tau$, and $\rho_E \ll \rho_\chi$, so the equations of motion for θ_E , θ_χ , and σ_E form a system of three differential equations with three unknowns R_3 , R_4 , and S_3 . Solving as we did for the radiative components we find:

$$\theta_E = -\frac{3(35 + 4R_\nu + 10R_B)}{7(15 + 4R_\nu + 10R_B)} \theta_\gamma = -\frac{3}{7} \theta_B \quad (5.92)$$

$$\theta_\chi = 9\theta_\gamma \quad (5.93)$$

$$\sigma_E = -\left(\frac{4}{3} + \frac{10}{3(15 + 4R_\nu + 10R_B)}\right) C(k\tau^2) = -\left(\frac{5}{2} + 15 + 4R_\nu + 10R_B\right) \sigma_\nu \quad (5.94)$$

Lastly, we need to determine the value of the only unknown constant left, C . To derive this, we transform our equations for the metric perturbations into the conformal-Newtonian gauge where the CNG metric potentials are written as

$$\psi = 2C \left(1 - 6 \frac{5 + 4R_\nu + 10R_B}{6(15 + 4R_\nu + 10R_B)}\right), \quad (5.95)$$

$$\phi = C \left(1 + 6 \frac{5 + 4R_\nu + 10R_B}{6(15 + 4R_\nu + 10R_B)} \right). \quad (5.96)$$

We choose the initial conditions to be set by the amplitude of X , the comoving curvature perturbation which is conserved on super-Hubble scales for adiabatic modes, and is given by

$$X = \phi + \frac{2}{3} \frac{\mathcal{H}^{-1} \phi' + \psi}{1 + w}. \quad (5.97)$$

We set $X = 1$ as is done for **CAMB**. Plugging in our metric potentials into our definition of X gives us $C = \frac{1}{2}$.

5.3.1. Initial Conditions in Pure Radiation Domination

Here we compile the initial conditions derived in the previous section. In these equations, the subscript b refers to baryons, and the subscript B refers to the B-field like component.

$$h = C(k\tau)^2 \quad (5.98)$$

$$\eta = 2C - \frac{5 + 4R_\nu + 10R_B}{6(15 + 4R_\nu + 10R_B)} C(k\tau)^2 \quad (5.99)$$

$$\delta_\gamma = \delta_\nu = \delta_E = \delta_B = -\frac{2}{3} C(k\tau)^2 \quad (5.100)$$

$$\delta_b = \delta_c = \frac{3}{4} \delta_\gamma \quad (5.101)$$

$$\delta_\chi = \frac{3}{4} (1 + w_\chi) \delta_\gamma \quad (5.102)$$

$$\theta_\gamma = \theta_b = -\frac{1}{18} C k^4 \tau^3 = \frac{1}{12} k^2 \tau \delta_\gamma \quad (5.103)$$

$$\theta_c = 0 \quad (5.104)$$

$$\theta_\nu = \frac{23 + 4R_\nu + 10R_B}{15 + 4R_\nu + 10R_B} \theta_\gamma \quad (5.105)$$

$$\theta_B = \frac{35 + 4R_\nu + 10R_B}{15 + 4R_\nu + 10R_B} \theta_\gamma \quad (5.106)$$

$$\theta_E = -\frac{3(35 + 4R_\nu + 10R_B)}{7(15 + 4R_\nu + 10R_B)} \theta_\gamma = -\frac{3}{7} \theta_B \quad (5.107)$$

$$\theta_\chi = 9\theta_\gamma \quad (5.108)$$

$$\sigma_\gamma = 0 \quad (5.109)$$

$$\sigma_\nu = \frac{4}{3(15 + 4R_\nu + 10R_B)} C(k\tau)^2 \quad (5.110)$$

$$\sigma_B = \frac{10}{3(15 + 4R_\nu + 10R_B)} C(k\tau)^2 = \frac{5}{2} \sigma_\nu \quad (5.111)$$

$$\sigma_E = -\left(\frac{4}{3} + \frac{10}{3(15 + 4R_\nu + 10R_B)}\right) C(k\tau)^2 \quad (5.112)$$

$$= -\left(\frac{5}{2} + 15 + 4R_\nu + 10R_B\right) \sigma_\nu, \quad (5.113)$$

where $C = \frac{1}{2}$, and we have defined

$$R_\nu = \frac{\rho_\nu}{\rho_\gamma + \rho_\nu + \rho_B}, \quad \text{and} \quad R_B = \frac{\rho_B}{\rho_\gamma + \rho_\nu + \rho_B}. \quad (5.114)$$

The synchronous gauge is defined as being co-moving with the CDM giving us $\theta_c = 0$, and the tight-coupling between photons and baryons gives us $\theta_b = \theta_\gamma$.

Note that these equations differ from the initial conditions derived for the Λ CDM model in Ref. [91] since our proposed scenario includes a non-negligible component of radiation, the B -field, to the cosmic fluid. In the limit that $R_B \rightarrow 0$, these equations match those in Ref. [91].

5.3.2. Correcting for the Presence of Matter

In solving for the initial conditions in the previous section, we assumed complete radiation domination. However, **CAMB** accounts for corrections to these conditions assuming a non-negligible presence of matter. These corrections will all be one higher order in τ . In this section, we amend our previous derivation to include these $\mathcal{O}(\tau)^3$ matter-corrections. The corrected perturbations in this scenario can now be written as

$$h = C(k\tau)^2[1 + A\tau], \quad (5.115)$$

$$\eta = 2C - R_1 C(k\tau)^2[1 + B\tau], \quad R_1 = \frac{5 + 4R_\nu + 10R_B}{6(15 + 4R_\nu + 10R_B)} \quad (5.116)$$

$$\delta_\gamma = -\frac{2}{3}C(k\tau)^2[1 + D\tau], \quad (5.117)$$

$$\theta_\gamma = -\frac{1}{18}Ck^4\tau^3, \quad (5.118)$$

$$\theta_\nu = R_2\theta_\gamma, \quad R_2 = \frac{23 + 4R_\nu + 10R_B}{15 + 4R_\nu + 10R_B} \quad (5.119)$$

$$\sigma_\nu = R_3 C(k\tau)^2[1 + F\tau], \quad R_3 = \frac{4}{3(15 + 4R_\nu + 10R_B)} \quad (5.120)$$

$$\theta_B = R_4\theta_\gamma, \quad R_4 = \frac{35 + 4R_\nu + 10R_B}{15 + 4R_\nu + 10R_B} \quad (5.121)$$

$$\sigma_B = R_5 C(k\tau)^2[1 + H\tau], \quad R_5 = \frac{10}{3(15 + 4R_\nu + 10R_B)}, \quad (5.122)$$

5.3 INITIAL CONDITIONS

where $\delta_\nu = \delta_\gamma$, $\delta_b = \delta_c = \frac{3}{4}\delta_\gamma$, as before, and the θ equations are not corrected as they are already $\mathcal{O}(\tau)^3$, leaving $\theta_c = 0$ and $\theta_b = \theta_\gamma$. Our goal is to solve for these correction coefficients A , B , D , F , and H .

Expanding the Friedmann equation to higher order and assuming $\rho_m \ll \rho_r$ in the radiation era we find

$$\mathcal{H} = \frac{1}{\tau} + \frac{1}{4}\omega, \quad (5.123)$$

and

$$\frac{\rho_m}{\rho_r} = \omega\tau + \frac{1}{4}\omega^2\tau^2, \quad (5.124)$$

where $\omega = \Omega_{m,0}H_0/\sqrt{\Omega_{r,0}}$, and $\Omega_{m,0}$ and $\Omega_{r,0}$ are the fractional densities of matter and radiation in the present day. Assuming non-negligible amounts of matter,

$$\delta \equiv \frac{\delta\rho_{tot}}{\rho_{tot}} = \left(1 - \frac{1}{4}\frac{\rho_m}{\rho_r}\right) \delta_\gamma, \quad (5.125)$$

where $\delta\rho_{tot}$ and ρ_{tot} , now sum up the contributions from both radiation and matter. Similarly, we define a new variable $\Theta \equiv \frac{[(\rho+p)\theta]_{tot}}{\rho_{tot}}$, which sums up all contributions to the velocity dispersion, and find

$$\Theta = \frac{4}{3} \left(1 - \frac{\rho_m}{\rho_r}\right) \left(1 - R_\nu - R_B + R_2R_\nu + R_4R_B + \frac{3}{4}R_b\frac{\rho_m}{\rho_r}\right) \theta_\gamma, \quad (5.126)$$

where $R_b = \rho_b/\rho_m$.

We now see that we have five unknown variables for which we need to solve: A , B , D , F , and H . We thus need five equations to determine their values. We choose the δ_γ equation of motion, the neutrino and B -component shear equations of motion, and the first and fourth Einstein's equations given in the previous section by (5.66),

and (5.69). Solving this system of equations we find that

$$A = D = -\frac{1}{5}\omega, \quad (5.127)$$

$$F = \frac{1}{4} \frac{10R_B + 4R_\nu - 5}{15 + 2R_\nu + 5R_B} \omega, \quad (5.128)$$

$$B = -\frac{1}{10} \frac{65 + 4R_\nu + 10R_B}{15 + 2R_\nu + 5R_B} \omega, \quad (5.129)$$

$$H = \frac{1}{4} \frac{10R_B + 4R_\nu - 5}{15 + 2R_\nu + 5R_B} \omega. \quad (5.130)$$

We note that **CAMB** does not include a correction term on η in the code. However, in the limit that $R_B \rightarrow 0$, these equations match those implemented in **CAMB**³, and deriving these equations without adding a correction on η gives results inconsistent with the code.

Section 5.4

Future Work

With the linear perturbation equations and initial conditions determined, this dark energy model can now be implemented in **CAMB**. At the time of submission of this thesis, implementation is underway and bugs are being worked out. Once our modified version of **CAMB** is fully functioning, we will investigate its phenomenology through its effects on the CMB angular power, and matter-power spectra, and through the evolution of perturbations. We plan to interface our modified Boltzmann code with an MCMC code such as **CosmoMC** in order to constrain the parameters of this model using cosmological datasets, as has been done with the models discussed in previous chapters.

³The **CAMB** initial conditions are derived in <https://cosmologist.info/notes/CAMB.pdf>

Chapter 6

Summary and Future Directions

Over many years, the Λ CDM model of cosmology became the concordance model due to its remarkable success in explaining a wide range of cosmological observations, from the cosmic microwave background to large-scale structure. Λ CDM fits cosmological data with high accuracy and precision, but despite its success, there are still outstanding questions and challenges, such as the nature of the dark sector, the details of cosmic inflation, and the newfound H_0 and S_8 parameter tensions. The problems facing the concordance model may be solved by applying new physics to current datasets, but new observational methods and techniques may also be needed to distinguish between different underlying cosmological scenarios. In this thesis, we address both the theoretical and observational sides of this argument. On the theoretical side, we explore multiple alternatives or extensions to Λ CDM that aim to explain these ambiguities and tensions. From the observational side we establish a general technique which allows line-intensity mapping to be used as a powerful probe of new physics.

In Chapter 2, we develop an assisted quintessence (AQ) model of early dark energy (EDE), linking the early and late epochs of cosmic acceleration. In the AQ framework, a spectrum of scalar fields is introduced, each with an exponential scaling potential.

As each field thaws from the Hubble friction, they evolve as a constant fraction of the background energy density until the effective potential is sufficiently flat and the fields inflate, dominate, and drive accelerated expansion. In this scenario, early and late dark energy are inevitable and generated through a single mechanism: EDE is just the thaw and activation of a scaling field; dark energy is the cumulative effect of the series of EDE fields. We tested this AQ-EDE model as a potential solution to both the Hubble tension, and the well-known coincidence problems of both early- and late-time dark energy. Using the most recent CMB, baryon-acoustic oscillation (BAO), galaxy survey, and supernovae data, we found that while the AQ-EDE model serves as a solid solution to the Hubble tension and coincidence problems at the background level, the full evolution of cosmological perturbations for any EDE model with a scaling potential alters the gravitational potential profiles too much to be viable with those implied by CMB temperature fluctuations. Put more succinctly, the evolution of cosmological perturbations can make or break a potential resolution to the Hubble tension, despite the background behavior of the dark-sector component.

Building off these results, in Chapter 3 we propose an improved parameterization for the perturbative dynamics of a new cosmic fluid component, where it becomes clear that anisotropic shear is just the result of an anisotropic sound speed in the fluid. Using this parameterization and a phenomenological fluid EDE model, we show that if you relax the assumption that EDE is fully isotropic, a requirement of EDE built from a single scalar field, the CMB fit to S_8 in a generic EDE model can be improved, indicating a potentially better fit to LSS data. EDE with an anisotropic shear is a clear indication of EDE built from more complicated physics than a scalar field, and can provide the same resolution to the H_0 tension as standard EDE, with a comparable fit to current CMB data, but without exacerbating the S_8 tension. Current CMB data cannot distinguish between standard EDE and anisotropic EDE,

suggesting that other datasets should be used to determine the underlying structure of EDE.

We have begun preliminary analysis of this model using CMB data from the *WMAP* satellite [165] and ground-based Atacama Cosmology Telescope (ACT) [166], which when combined act as an independent CMB dataset comparable to *Planck*. Similarly to a standard EDE model [20–22], we find significant preference for non-zero amounts of EDE, but unexpectedly we also find a stronger preference for a larger amount of shear. In this model with strongly anisotropic EDE, the resolution to the Hubble tension goes away, though the S_8 tension is still relaxed. I look forward to exploring these results in more detail, as well as incorporating other datasets in this analysis. In particular, the different clustering behavior in this anisotropic EDE model suggests looking at it with the next generation of LSS experiments which will dramatically increase the volume of LSS data across a range of redshifts and scales.

Chapter 4, explores the ability of line-intensity mapping (LIM) experiments to constrain beyond the standard model cosmologies by performing a joint analysis of the two LIM observables: the power spectrum and voxel intensity distribution (VID). The information contained in these two statistics is highly complementary, and their combination allows for a major increase in precision. Until recently, such an analysis required the use of simulations to empirically estimate the covariance between these two statistics. We show how to do such an analysis analytically, and we apply this technique to forecast constraints on a range of non-cold dark matter models, as well as non-Gaussianity. We find that the combination of these statistics breaks precision-limiting degeneracies between astrophysical and cosmological parameters, allowing for first-generation LIM experiments, such as the SPHEREx satellite [125], to be able to provide competitive constraints on a range of physical and phenomenological extensions to the standard cosmological model. Over the next decade, more than

a dozen experiments are expected to produce line-intensity maps spanning from the present day to the end of reionization [106, 107]. I look forward to continuing work in building new techniques and improving the data analysis pipeline necessary to extract useful cosmological information from these experiments.

Finally, in Chapter 5 we derive the cosmological linear perturbations and initial conditions needed to fully describe a dark energy model built from a triplet of classical $U(1)$ gauge fields coupled to a scalar field via a Chern-Simons coupling. Such a model has a few interesting features for the Hubble tension: the gauge fields act as an extra component of dark radiation, which would aid in raising the CMB-inferred value of the Hubble constant, while not facing the same restrictions as purely scalar-field EDE; the coupling between the scalar and gauge fields introduce an anisotropic shear reminiscent of the shear investigated in Chapter 3. With all the necessary perturbative evolution laid out in this chapter, I look forward to exploring the phenomenology of this model and its viability with cosmological datasets in the near future.

In summary, the results presented in this thesis offer valuable insight into the search for new physics beyond the standard model in the era of precision cosmology. In the near future, data from experiments targeting all epochs of the Universe will become available, providing new ways to build and test beyond the standard model cosmologies. I am excited to continue to contribute to both the theory and analysis preparation needed to accurately and efficiently test cosmological models with this data.

Bibliography

1. Freedman, W. L. Measurements of the Hubble Constant: Tensions in Perspective. *Astrophys. J.* **919**, 16. arXiv: 2106.15656 [astro-ph.CO] (2021).
2. Riess, A. G. *et al.* Observational evidence from supernovae for an accelerating universe and a cosmological constant. *Astron. J.* **116**, 1009–1038. arXiv: astro-ph/9805201 (1998).
3. Perlmutter, S. *et al.* Measurements of Ω and Λ from 42 high redshift supernovae. *Astrophys. J.* **517**, 565–586. arXiv: astro-ph/9812133 (1999).
4. Aghanim, N. *et al.* Planck 2018 results. VI. Cosmological parameters. *Astron. Astrophys.* **641**. [Erratum: *Astron. Astrophys.* 652, C4 (2021)], A6. arXiv: 1807.06209 [astro-ph.CO] (2020).
5. Alam, S. *et al.* The clustering of galaxies in the completed SDSS-III Baryon Oscillation Spectroscopic Survey: cosmological analysis of the DR12 galaxy sample. *Mon. Not. Roy. Astron. Soc.* **470**, 2617–2652. arXiv: 1607.03155 [astro-ph.CO] (2017).
6. Abbott, T. M. C. *et al.* Dark Energy Survey Year 3 results: Cosmological constraints from galaxy clustering and weak lensing. *Phys. Rev. D* **105**, 023520. arXiv: 2105.13549 [astro-ph.CO] (2022).

7. Riess, A. G. *et al.* Cosmic Distances Calibrated to 1% Precision with Gaia EDR3 Parallaxes and Hubble Space Telescope Photometry of 75 Milky Way Cepheids Confirm Tension with Λ CDM. *Astrophys. J. Lett.* **908**, L6. arXiv: 2012.08534 [astro-ph.CO] (2021).
8. Riess, A. G. *et al.* *A Comprehensive Measurement of the Local Value of the Hubble Constant with 1 km/s/Mpc Uncertainty from the Hubble Space Telescope and the SH0ES Team* arXiv: 2112.04510 [astro-ph.CO].
9. Amon, A. *et al.* Consistent lensing and clustering in a low- S_8 Universe with BOSS, DES Year 3, HSC Year 1 and KiDS-1000. arXiv: 2202.07440 [astro-ph.CO] (Feb. 2022).
10. Amon, A. & Efstathiou, G. A non-linear solution to the S_8 tension? arXiv: 2206.11794 [astro-ph.CO] (June 2022).
11. Efstathiou, G. H_0 Revisited. *Mon. Not. Roy. Astron. Soc.* **440**, 1138–1152. arXiv: 1311.3461 [astro-ph.CO] (2014).
12. Addison, G. E. *et al.* Quantifying discordance in the 2015 Planck CMB spectrum. *Astrophys. J.* **818**, 132. arXiv: 1511.00055 [astro-ph.CO] (2016).
13. Aghanim, N. *et al.* Planck intermediate results. LI. Features in the cosmic microwave background temperature power spectrum and shifts in cosmological parameters. *Astron. Astrophys.* **607**, A95. arXiv: 1608.02487 [astro-ph.CO] (2017).
14. Aylor, K. *et al.* Sounds Discordant: Classical Distance Ladder & Λ CDM - based Determinations of the Cosmological Sound Horizon. *Astrophys. J.* **874**, 4. arXiv: 1811.00537 [astro-ph.CO] (2019).

-
15. Weinberg, D. H., Bullock, J. S., Governato, F., Kuzio de Naray, R. & Peter, A. H. G. Cold dark matter: controversies on small scales. *Proc. Nat. Acad. Sci.* **112**, 12249–12255. arXiv: 1306.0913 [astro-ph.CO] (2015).
 16. De Blok, W. J. G. The Core-Cusp Problem. *Adv. Astron.* **2010**, 789293. arXiv: 0910.3538 [astro-ph.CO] (2010).
 17. Di Valentino, E. *et al.* In the realm of the Hubble tension—a review of solutions. *Class. Quant. Grav.* **38**, 153001. arXiv: 2103.01183 [astro-ph.CO] (2021).
 18. Schöneberg, N. *et al.* *The H_0 Olympics: A fair ranking of proposed models* arXiv: 2107.10291 [astro-ph.CO].
 19. Poulin, V., Smith, T. L. & Karwal, T. The Ups and Downs of Early Dark Energy solutions to the Hubble tension: a review of models, hints and constraints circa 2023. arXiv: 2302.09032 [astro-ph.CO] (Feb. 2023).
 20. Poulin, V., Smith, T. L. & Bartlett, A. Dark energy at early times and ACT data: A larger Hubble constant without late-time priors. *Phys. Rev. D* **104**, 123550. arXiv: 2109.06229 [astro-ph.CO] (2021).
 21. Hill, J. C. *et al.* *The Atacama Cosmology Telescope: Constraints on Pre-Recombination Early Dark Energy* arXiv: 2109.04451 [astro-ph.CO].
 22. Smith, T. L. *et al.* *Hints of Early Dark Energy in Planck, SPT, and ACT data: new physics or systematics?* arXiv: 2202.09379 [astro-ph.CO].
 23. Hill, J. C., McDonough, E., Toomey, M. W. & Alexander, S. Early dark energy does not restore cosmological concordance. *Phys. Rev. D* **102**, 043507. arXiv: 2003.07355 [astro-ph.CO] (2020).
 24. Ivanov, M. M. *et al.* Constraining Early Dark Energy with Large-Scale Structure. *Phys. Rev. D* **102**, 103502. arXiv: 2006.11235 [astro-ph.CO] (2020).

25. D’Amico, G., Senatore, L., Zhang, P. & Zheng, H. The Hubble Tension in Light of the Full-Shape Analysis of Large-Scale Structure Data. *JCAP* **05**, 072. arXiv: 2006.12420 [astro-ph.CO] (2021).
26. Clark, S. J., Vattis, K., Fan, J. & Koushiappas, S. M. *The H_0 and S_8 tensions necessitate early and late time changes to Λ CDM* arXiv: 2110.09562 [astro-ph.CO].
27. Cai, R.-G., Guo, Z.-K., Wang, S.-J., Yu, W.-W. & Zhou, Y. No-go guide for the Hubble tension: Late-time solutions. *Phys. Rev. D* **105**, L021301. arXiv: 2107.13286 [astro-ph.CO] (2022).
28. Vagnozzi, S. Consistency tests of Λ CDM from the early integrated Sachs-Wolfe effect: Implications for early-time new physics and the Hubble tension. *Phys. Rev. D* **104**, 063524. arXiv: 2105.10425 [astro-ph.CO] (2021).
29. Kim, S. A., Liddle, A. R. & Tsujikawa, S. Dynamics of assisted quintessence. *Phys. Rev. D* **72**, 043506. arXiv: astro-ph/0506076 (2005).
30. Riess, A. G., Casertano, S., Yuan, W., Macri, L. M. & Scolnic, D. Large Magellanic Cloud Cepheid Standards Provide a 1% Foundation for the Determination of the Hubble Constant and Stronger Evidence for Physics beyond Λ CDM. *Astrophys. J.* **876**, 85. arXiv: 1903.07603 [astro-ph.CO] (2019).
31. Steinhardt, P. J., Wang, L.-M. & Zlatev, I. Cosmological tracking solutions. *Phys. Rev. D* **59**, 123504. arXiv: astro-ph/9812313 (1999).
32. Ferreira, P. G. & Joyce, M. Cosmology with a primordial scaling field. *Phys. Rev. D* **58**, 023503. arXiv: astro-ph/9711102 (1998).
33. Lucchin, F. & Matarrese, S. Power Law Inflation. *Phys. Rev. D* **32**, 1316 (1985).
34. Halliwell, J. Scalar Fields in Cosmology with an Exponential Potential. *Phys. Lett. B* **185**, 341 (1987).

- 35. Shafi, Q. & Wetterich, C. Inflation From Higher Dimensions. *Nucl. Phys. B* **289**, 787–809 (1987).
- 36. Ratra, B. & Peebles, P. Cosmological Consequences of a Rolling Homogeneous Scalar Field. *Phys. Rev. D* **37**, 3406 (1988).
- 37. Burd, A. & Barrow, J. D. Inflationary Models with Exponential Potentials. *Nucl. Phys. B* **308**. [Erratum: Nucl.Phys.B 324, 276–276 (1989)], 929–945 (1988).
- 38. Wetterich, C. An asymptotically vanishing time dependent cosmological ‘constant’. *Astron. Astrophys.* **301**, 321–328. arXiv: hep-th/9408025 (1995).
- 39. Copeland, E. J., Liddle, A. R. & Wands, D. Exponential potentials and cosmological scaling solutions. *Phys. Rev. D* **57**, 4686–4690. arXiv: gr-qc/9711068 (1998).
- 40. Chang, H.-Y. & Scherrer, R. J. *Reviving Quintessence with an Exponential Potential* arXiv: 1608.03291 [astro-ph.CO].
- 41. Poulin, V., Smith, T. L., Karwal, T. & Kamionkowski, M. Early Dark Energy Can Resolve The Hubble Tension. *Phys. Rev. Lett.* **122**, 221301. arXiv: 1811.04083 [astro-ph.CO] (2019).
- 42. Knox, L. & Millea, M. Hubble constant hunter’s guide. *Phys. Rev. D* **101**, 043533. arXiv: 1908.03663 [astro-ph.CO] (2020).
- 43. Smith, T. L., Poulin, V. & Amin, M. A. Oscillating scalar fields and the Hubble tension: a resolution with novel signatures. *Phys. Rev. D* **101**, 063523. arXiv: 1908.06995 [astro-ph.CO] (2020).
- 44. Karwal, T. & Kamionkowski, M. Dark energy at early times, the Hubble parameter, and the string axiverse. *Phys. Rev. D* **94**, 103523. arXiv: 1608.01309 [astro-ph.CO] (2016).

-
45. Poulin, V., Smith, T. L., Grin, D., Karwal, T. & Kamionkowski, M. Cosmological implications of ultralight axionlike fields. *Phys. Rev. D* **98**, 083525. arXiv: 1806.10608 [astro-ph.CO] (2018).
46. D’Eramo, F., Ferreira, R. Z., Notari, A. & Bernal, J. L. Hot Axions and the H_0 tension. *JCAP* **11**, 014. arXiv: 1808.07430 [hep-ph] (2018).
47. Lin, M.-X., Benevento, G., Hu, W. & Raveri, M. Acoustic Dark Energy: Potential Conversion of the Hubble Tension. *Phys. Rev. D* **100**, 063542. arXiv: 1905.12618 [astro-ph.CO] (2019).
48. Agrawal, P., Cyr-Racine, F.-Y., Pinner, D. & Randall, L. *Rock ’n’ Roll Solutions to the Hubble Tension* arXiv: 1904.01016 [astro-ph.CO].
49. Ma, C.-P. & Bertschinger, E. Cosmological perturbation theory in the synchronous and conformal Newtonian gauges. *Astrophys. J.* **455**, 7–25. arXiv: astro-ph/9506072 (1995).
50. Dave, R., Caldwell, R. R. & Steinhardt, P. J. Sensitivity of the cosmic microwave background anisotropy to initial conditions in quintessence cosmology. *Phys. Rev. D* **66**, 023516. arXiv: astro-ph/0206372 (2002).
51. Malquarti, M. & Liddle, A. R. Initial conditions for quintessence after inflation. *Phys. Rev. D* **66**, 023524. arXiv: astro-ph/0203232 (2002).
52. Lewis, A. & Bridle, S. Cosmological parameters from CMB and other data: A Monte Carlo approach. *Phys. Rev. D* **66**, 103511. arXiv: astro-ph/0205436 (2002).
53. Lewis, A., Challinor, A. & Lasenby, A. Efficient computation of CMB anisotropies in closed FRW models. *Astrophys. J.* **538**, 473–476. arXiv: astro-ph/9911177 (2000).

-
54. Aghanim, N. *et al.* Planck 2018 results. V. CMB power spectra and likelihoods. *Astron. Astrophys.* **641**, A5. arXiv: 1907.12875 [astro-ph.CO] (2020).
55. Gelman, A. & Rubin, D. B. Inference from Iterative Simulation Using Multiple Sequences. *Statist. Sci.* **7**, 457–472 (1992).
56. Caldwell, R. R. An introduction to quintessence. *Braz. J. Phys.* **30** (ed Cline, D. B.) 215–229 (2000).
57. Hildebrandt, H. *et al.* KiDS-450: Cosmological parameter constraints from tomographic weak gravitational lensing. *Mon. Not. Roy. Astron. Soc.* **465**, 1454. arXiv: 1606.05338 [astro-ph.CO] (2017).
58. Aghanim, N. *et al.* Planck 2018 results. VI. Cosmological parameters. *Astron. Astrophys.* **641**, A6. arXiv: 1807.06209 [astro-ph.CO] (2020).
59. Motloch, P. & Hu, W. Lensinglike tensions in the *Planck* legacy release. *Phys. Rev. D* **101**, 083515. arXiv: 1912.06601 [astro-ph.CO] (2020).
60. Braglia, M., Emond, W. T., Finelli, F., Gumrukcuoglu, A. E. & Koyama, K. Unified framework for early dark energy from α -attractors. *Phys. Rev. D* **102**, 083513. arXiv: 2005.14053 [astro-ph.CO] (2020).
61. Di Valentino, E., Melchiorri, A. & Mena, O. Can interacting dark energy solve the H_0 tension? *Phys. Rev. D* **96**, 043503. arXiv: 1704.08342 [astro-ph.CO] (2017).
62. Alam, S. *et al.* The clustering of galaxies in the completed SDSS-III Baryon Oscillation Spectroscopic Survey: cosmological analysis of the DR12 galaxy sample. *Mon. Not. Roy. Astron. Soc.* **470**, 2617–2652. arXiv: 1607.03155 [astro-ph.CO] (2017).

-
63. Beutler, F. *et al.* The 6dF Galaxy Survey: Baryon Acoustic Oscillations and the Local Hubble Constant. *Mon. Not. Roy. Astron. Soc.* **416**, 3017–3032. arXiv: 1106.3366 [astro-ph.CO] (2011).
64. Ross, A. J. *et al.* The clustering of the SDSS DR7 main Galaxy sample – I. A 4 per cent distance measure at $z = 0.15$. *Mon. Not. Roy. Astron. Soc.* **449**, 835–847. arXiv: 1409.3242 [astro-ph.CO] (2015).
65. Poulin, V., Smith, T. L., Grin, D., Karwal, T. & Kamionkowski, M. Cosmological implications of ultralight axionlike fields. *Phys. Rev. D* **98**, 083525. arXiv: 1806.10608 [astro-ph.CO] (2018).
66. Sakstein, J. & Trodden, M. Early Dark Energy from Massive Neutrinos as a Natural Resolution of the Hubble Tension. *Phys. Rev. Lett.* **124**, 161301. arXiv: 1911.11760 [astro-ph.CO] (2020).
67. Carrillo González, M., Liang, Q., Sakstein, J. & Trodden, M. Neutrino-Assisted Early Dark Energy: Theory and Cosmology. *JCAP* **04**, 063. arXiv: 2011.09895 [astro-ph.CO] (2021).
68. Agrawal, P., Cyr-Racine, F.-Y., Pinner, D. & Randall, L. *Rock 'n' Roll Solutions to the Hubble Tension* arXiv: 1904.01016 [astro-ph.CO].
69. Lin, M.-X., Benevento, G., Hu, W. & Raveri, M. Acoustic Dark Energy: Potential Conversion of the Hubble Tension. *Phys. Rev. D* **100**, 063542. arXiv: 1905.12618 [astro-ph.CO] (2019).
70. Karwal, T., Raveri, M., Jain, B., Khoury, J. & Trodden, M. *Chameleon Early Dark Energy and the Hubble Tension* arXiv: 2106.13290 [astro-ph.CO].
71. Ye, G., Zhang, J. & Piao, Y.-S. *Resolving both H_0 and S_8 tensions with AdS early dark energy and ultralight axion* arXiv: 2107.13391 [astro-ph.CO].

- 72. Poulin, V., Smith, T. L., Karwal, T. & Kamionkowski, M. Early Dark Energy Can Resolve The Hubble Tension. *Phys. Rev. Lett.* **122**, 221301. arXiv: 1811.04083 [astro-ph.CO] (2019).
- 73. Smith, T. L., Poulin, V. & Amin, M. A. Oscillating scalar fields and the Hubble tension: a resolution with novel signatures. *Phys. Rev. D* **101**, 063523. arXiv: 1908.06995 [astro-ph.CO] (2020).
- 74. Murgia, R., Abellán, G. F. & Poulin, V. Early dark energy resolution to the Hubble tension in light of weak lensing surveys and lensing anomalies. *Phys. Rev. D* **103**, 063502. arXiv: 2009.10733 [astro-ph.CO] (2021).
- 75. Smith, T. L. *et al.* Early dark energy is not excluded by current large-scale structure data. *Phys. Rev. D* **103**, 123542. arXiv: 2009.10740 [astro-ph.CO] (2021).
- 76. Niedermann, F. & Sloth, M. S. New early dark energy. *Phys. Rev. D* **103**, L041303. arXiv: 1910.10739 [astro-ph.CO] (2021).
- 77. Niedermann, F. & Sloth, M. S. Resolving the Hubble tension with new early dark energy. *Phys. Rev. D* **102**, 063527. arXiv: 2006.06686 [astro-ph.CO] (2020).
- 78. Niedermann, F. & Sloth, M. S. New Early Dark Energy is compatible with current LSS data. *Phys. Rev. D* **103**, 103537. arXiv: 2009.00006 [astro-ph.CO] (2021).
- 79. Freese, K. & Winkler, M. W. Chain early dark energy: A Proposal for solving the Hubble tension and explaining today's dark energy. *Phys. Rev. D* **104**, 083533. arXiv: 2102.13655 [astro-ph.CO] (2021).
- 80. Battye, R. A. & Moss, A. Cosmological Perturbations in Elastic Dark Energy Models. *Phys. Rev. D* **76**, 023005. arXiv: astro-ph/0703744 (2007).

- 81. Battye, R. A. & Pearson, J. A. Parametrizing dark sector perturbations via equations of state. *Phys. Rev. D* **88**, 061301. arXiv: 1306.1175 [astro-ph.CO] (2013).
- 82. Hu, W. Structure formation with generalized dark matter. *Astrophys. J.* **506**, 485–494. arXiv: astro-ph/9801234 (1998).
- 83. Weinberg, S. Damping of tensor modes in cosmology. *Phys. Rev. D* **69**, 023503. arXiv: astro-ph/0306304 (2004).
- 84. Bucher, M. & Spergel, D. N. Is the dark matter a solid? *Phys. Rev. D* **60**, 043505. arXiv: astro-ph/9812022 (1999).
- 85. Battye, R. A., Bucher, M. & Spergel, D. *Domain wall dominated universes* arXiv: astro-ph/9908047.
- 86. Battye, R. A., Carter, B., Chachoua, E. & Moss, A. Rigidity and stability of cold dark solid universe model. *Phys. Rev. D* **72**, 023503. arXiv: hep-th/0501244 (2005).
- 87. Battye, R. A. & Moss, A. Constraints on the solid dark Universe model. *JCAP* **06**, 001. arXiv: astro-ph/0503033 (2005).
- 88. Battye, R. A., Moss, A. & Pearson, J. A. Constraining dark sector perturbations I: cosmic shear and CMB lensing. *JCAP* **04**, 048. arXiv: 1409.4650 [astro-ph.CO] (2015).
- 89. Soergel, B., Giannantonio, T., Weller, J. & Battye, R. A. Constraining dark sector perturbations II: ISW and CMB lensing tomography. *JCAP* **02**, 037. arXiv: 1409.4540 [astro-ph.CO] (2015).
- 90. Bielefeld, J. & Caldwell, R. R. Cosmological consequences of classical flavor-space locked gauge field radiation. *Phys. Rev. D* **91**, 124004. arXiv: 1503.05222 [gr-qc] (2015).

-
91. Ma, C.-P. & Bertschinger, E. Cosmological perturbation theory in the synchronous and conformal Newtonian gauges. *Astrophys. J.* **455**, 7–25. arXiv: [astro-ph/9506072](#) (1995).
92. Turner, M. S. Coherent Scalar Field Oscillations in an Expanding Universe. *Phys. Rev. D* **28**, 1243 (1983).
93. Cembranos, J. A. R., Maroto, A. L. & Núñez Jareño, S. J. Cosmological perturbations in coherent oscillating scalar field models. *JHEP* **03**, 013. arXiv: [1509.08819 \[astro-ph.CO\]](#) (2016).
94. Lewis, A. & Bridle, S. Cosmological parameters from CMB and other data: A Monte Carlo approach. *Phys. Rev. D* **66**, 103511. arXiv: [astro-ph/0205436](#) (2002).
95. Lewis, A., Challinor, A. & Lasenby, A. Efficient computation of CMB anisotropies in closed FRW models. *Astrophys. J.* **538**, 473–476. arXiv: [astro-ph/9911177](#) (2000).
96. Aghanim, N. *et al.* Planck 2018 results. V. CMB power spectra and likelihoods. *Astron. Astrophys.* **641**, A5. arXiv: [1907.12875 \[astro-ph.CO\]](#) (2020).
97. Beutler, F. *et al.* The 6dF Galaxy Survey: Baryon Acoustic Oscillations and the Local Hubble Constant. *Mon. Not. Roy. Astron. Soc.* **416**, 3017–3032. arXiv: [1106.3366 \[astro-ph.CO\]](#) (2011).
98. Ross, A. J. *et al.* The clustering of the SDSS DR7 main Galaxy sample – I. A 4 per cent distance measure at $z = 0.15$. *Mon. Not. Roy. Astron. Soc.* **449**, 835–847. arXiv: [1409.3242 \[astro-ph.CO\]](#) (2015).
99. Scolnic, D. M. *et al.* The Complete Light-curve Sample of Spectroscopically Confirmed SNe Ia from Pan-STARRS1 and Cosmological Constraints from

- the Combined Pantheon Sample. *Astrophys. J.* **859**, 101. arXiv: 1710.00845 [astro-ph.CO] (2018).
100. Gelman, A. & Rubin, D. B. Inference from Iterative Simulation Using Multiple Sequences. *Statist. Sci.* **7**, 457–472 (1992).
 101. Abazajian, K. N. *et al.* *CMB-S4 Science Book, First Edition* arXiv: 1610.02743 [astro-ph.CO].
 102. Asgari, M. *et al.* KiDS-1000 Cosmology: Cosmic shear constraints and comparison between two point statistics. *Astron. Astrophys.* **645**, A104. arXiv: 2007.15633 [astro-ph.CO] (2021).
 103. Ade, P. A. R. *et al.* Planck 2015 results. XIII. Cosmological parameters. *Astron. Astrophys.* **594**, A13. arXiv: 1502.01589 [astro-ph.CO] (2016).
 104. Turok, N., Pen, U.-L. & Seljak, U. The Scalar, vector and tensor contributions to CMB anisotropies from cosmic defects. *Phys. Rev. D* **58**, 023506. arXiv: astro-ph/9706250 (1998).
 105. Kovetz, E. D. *et al.* Line-Intensity Mapping: 2017 Status Report. arXiv: 1709.09066 [astro-ph.CO] (Sept. 2017).
 106. Kovetz, E. D. *et al.* Astrophysics and Cosmology with Line-Intensity Mapping. *Bull. Am. Astron. Soc.* **51**, 101. arXiv: 1903.04496 [astro-ph.CO] (2020).
 107. Bernal, J. L. & Kovetz, E. D. Line-intensity mapping: theory review with a focus on star-formation lines. *Astron. Astrophys. Rev.* **30**, 5. arXiv: 2206.15377 [astro-ph.CO] (2022).
 108. Schaan, E. & White, M. Astrophysics & Cosmology from Line Intensity Mapping vs Galaxy Surveys. *JCAP* **05**, 067. arXiv: 2103.01971 [astro-ph.CO] (2021).

109. Chang, T.-C., Pen, U.-L., Peterson, J. B. & McDonald, P. Baryon Acoustic Oscillation Intensity Mapping as a Test of Dark Energy. *Phys. Rev. Lett.* **100**, 091303. arXiv: 0709.3672 [astro-ph] (2008).
110. Loeb, A. & Wyithe, S. Precise Measurement of the Cosmological Power Spectrum With a Dedicated 21cm Survey After Reionization. *Phys. Rev. Lett.* **100**, 161301. arXiv: 0801.1677 [astro-ph] (2008).
111. Visbal, E., Loeb, A. & Wyithe, J. S. B. Cosmological Constraints from 21cm Surveys After Reionization. *JCAP* **10**, 030. arXiv: 0812.0419 [astro-ph] (2009).
112. Van Haarlem, M. P. *et al.* LOFAR: The LOw-Frequency ARray. *Astron. Astrophys.* **556**, A2. arXiv: 1305.3550 [astro-ph.IM] (2013).
113. Bandura, K. *et al.* Canadian Hydrogen Intensity Mapping Experiment (CHIME) Pathfinder. *Proc. SPIE Int. Soc. Opt. Eng.* **9145**, 22. arXiv: 1406.2288 [astro-ph.IM] (2014).
114. DeBoer, D. R. *et al.* Hydrogen Epoch of Reionization Array (HERA). *Publ. Astron. Soc. Pac.* **129**, 045001. arXiv: 1606.07473 [astro-ph.IM] (2017).
115. Santos, M. G. *et al.* MeerKLASS: MeerKAT Large Area Synoptic Survey in MeerKAT Science: On the Pathway to the SKA (Sept. 2017). arXiv: 1709.06099 [astro-ph.CO].
116. Keating, G. K., Marrone, D. P., Bower, G. C. & Keenan, R. P. An Intensity Mapping Detection of Aggregate CO Line Emission at 3 mm. *Astrophys. J.* **901**, 141. arXiv: 2008.08087 [astro-ph.GA] (2020).
117. Keating, G. K. *et al.* COPSS II: The molecular gas content of ten million cubic megaparsecs at redshift $z \sim 3$. *Astrophys. J.* **830**, 34. arXiv: 1605.03971 [astro-ph.GA] (2016).

-
118. Cleary, K. A. *et al.* COMAP Early Science: I. Overview. arXiv: 2111.05927 [astro-ph.CO] (Nov. 2021).
119. Ade, P. *et al.* A wide field-of-view low-resolution spectrometer at APEX: Instrument design and scientific forecast. *Astron. Astrophys.* **642**, A60. arXiv: 2007.14246 [astro-ph.IM] (2020).
120. Gebhardt, K. *et al.* The Hobby–Eberly Telescope Dark Energy Experiment (HETDEX) Survey Design, Reductions, and Detections*. *Astrophys. J.* **923**, 217. arXiv: 2110.04298 [astro-ph.IM] (2021).
121. Aravena, M. *et al.* CCAT-prime Collaboration: Science Goals and Forecasts with Prime-Cam on the Fred Young Submillimeter Telescope. *Astrophys. J. Suppl.* **264**, 7. arXiv: 2107.10364 [astro-ph.CO] (2023).
122. Sun, G. *et al.* Probing Cosmic Reionization and Molecular Gas Growth with TIME. *Astrophys. J.* **915**, 33. arXiv: 2012.09160 [astro-ph.GA] (2021).
123. Switzer, E. R. *et al.* Experiment for cryogenic large-aperture intensity mapping: instrument design. *J. Astron. Telesc. Instrum. Syst.* **7**, 044004 (2021).
124. Vieira, J. *et al.* The Terahertz Intensity Mapper (TIM): a Next-Generation Experiment for Galaxy Evolution Studies. *arXiv e-prints*, arXiv:2009.14340. arXiv: 2009.14340 [astro-ph.IM] (Sept. 2020).
125. Doré, O. *et al.* Cosmology with the SPHEREX All-Sky Spectral Survey. arXiv: 1412.4872 [astro-ph.CO] (Dec. 2014).
126. Koopmans, L. V. E. *et al.* The Cosmic Dawn and Epoch of Reionization with the Square Kilometre Array. *PoS AASKA14* (eds Bourke, T. L. *et al.*) 001. arXiv: 1505.07568 [astro-ph.CO] (2015).

-
127. Newburgh, L. B. *et al.* HIRAX: A Probe of Dark Energy and Radio Transients. *Proc. SPIE Int. Soc. Opt. Eng.* **9906** (eds Hall, H. J., Gilmozzi, R. & Marshall, H. K.) 99065X. arXiv: 1607.02059 [astro-ph.IM] (2016).
128. Padmanabhan, H., Refregier, A. & Amara, A. Impact of astrophysics on cosmology forecasts for 21 cm surveys. *Mon. Not. Roy. Astron. Soc.* **485**, 4060–4070. arXiv: 1804.10627 [astro-ph.CO] (2019).
129. Bernal, J. L., Breysse, P. C., Gil-Marín, H. & Kovetz, E. D. User’s guide to extracting cosmological information from line-intensity maps. *Phys. Rev. D* **100**, 123522. arXiv: 1907.10067 [astro-ph.CO] (2019).
130. Sato-Polito, G. & Bernal, J. L. Analytical covariance between voxel intensity distributions and line-intensity mapping power spectra. arXiv: 2202.02330 [astro-ph.CO] (Feb. 2022).
131. Breysse, P. C., Kovetz, E. D., Behroozi, P. S., Dai, L. & Kamionkowski, M. Insights from probability distribution functions of intensity maps. *Mon. Not. Roy. Astron. Soc.* **467**, 2996–3010. arXiv: 1609.01728 [astro-ph.CO] (2017).
132. Ihle, H. T. *et al.* Joint power spectrum and voxel intensity distribution forecast on the CO luminosity function with COMAP. *Astrophys. J.* **871**, 75. arXiv: 1808.07487 [astro-ph.CO] (2019).
133. Chung, D. T. *et al.* COMAP Early Science. V. Constraints and Forecasts at $z \sim 3$. *Astrophys. J.* **933**, 186. arXiv: 2111.05931 [astro-ph.CO] (2022).
134. Breysse, P. C. Breaking the intensity-bias degeneracy in line intensity mapping. arXiv: 2209.01223 [astro-ph.CO] (Sept. 2022).
135. Del Popolo, A. & Le Delliou, M. Review of Solutions to the Cusp-Core Problem of the Λ CDM Model. *Galaxies* **9**, 123. arXiv: 2209.14151 [astro-ph.CO] (2021).

-
136. Libanore, S., Unal, C., Sarkar, D. & Kovetz, E. D. Unveiling cosmological information on small scales with line intensity mapping. *Phys. Rev. D* **106**, 123512. arXiv: 2208.01658 [astro-ph.CO] (2022).
137. Marsh, D. J. E. Axion Cosmology. *Phys. Rept.* **643**, 1–79. arXiv: 1510.07633 [astro-ph.CO] (2016).
138. Kim, J. E. & Marsh, D. J. E. An ultralight pseudoscalar boson. *Phys. Rev. D* **93**, 025027. arXiv: 1510.01701 [hep-ph] (2016).
139. Chun, E. J. Axion Dark Matter with High-Scale Inflation. *Phys. Lett. B* **735**, 164–167. arXiv: 1404.4284 [hep-ph] (2014).
140. Kawasaki, M., Saikawa, K. & Sekiguchi, T. Axion dark matter from topological defects. *Phys. Rev. D* **91**, 065014. arXiv: 1412.0789 [hep-ph] (2015).
141. Hwang, J.-c. & Noh, H. Axion as a Cold Dark Matter candidate. *Phys. Lett. B* **680**, 1–3. arXiv: 0902.4738 [astro-ph.CO] (2009).
142. Visinelli, L. & Gondolo, P. Axion cold dark matter in non-standard cosmologies. *Phys. Rev. D* **81**, 063508. arXiv: 0912.0015 [astro-ph.CO] (2010).
143. Kamionkowski, M. *WIMP and axion dark matter* in *ICTP Summer School in High-Energy Physics and Cosmology* (June 1997), 394–411. arXiv: hep-ph/9710467.
144. Preskill, J., Wise, M. B. & Wilczek, F. Cosmology of the Invisible Axion. *Phys. Lett. B* **120** (ed Srednicki, M. A.) 127–132 (1983).
145. Bauer, J. B., Marsh, D. J. E., Hložek, R., Padmanabhan, H. & Laguë, A. Intensity Mapping as a Probe of Axion Dark Matter. *Mon. Not. Roy. Astron. Soc.* **500**, 3162–3177. arXiv: 2003.09655 [astro-ph.CO] (2020).

146. Akrami, Y. *et al.* Planck 2018 results. IX. Constraints on primordial non-Gaussianity. *Astron. Astrophys.* **641**, A9. arXiv: 1905.05697 [astro-ph.CO] (2020).
147. Kennicutt Jr., R. C. Star formation in galaxies along the Hubble sequence. *Ann. Rev. Astron. Astrophys.* **36**, 189–231. arXiv: astro-ph/9807187 (1998).
148. Ly, C. *et al.* The Luminosity Function and Star Formation Rate between Redshifts of 0.07 and 1.47 for Narrow-band Emitters in the Subaru Deep Field. *Astrophys. J.* **657**, 738–759. arXiv: astro-ph/0610846 (2007).
149. Saito, S. *et al.* The Synthetic Emission Line COSMOS catalog: H α and [OII] galaxy luminosity functions and counts at $0.3 < z < 2.5$. *Mon. Not. Roy. Astron. Soc.* **494**, 199–217. arXiv: 2003.06394 [astro-ph.CO] (2020).
150. Kaiser, N. Clustering in real space and in redshift space. *Mon. Not. Roy. Astron. Soc.* **227**, 1–27 (1987).
151. Coles, P. & Jones, B. A Lognormal model for the cosmological mass distribution. *Mon. Not. Roy. Astron. Soc.* **248**, 1–13 (1991).
152. Li, T. Y., Wechsler, R. H., Devaraj, K. & Church, S. E. Connecting CO Intensity Mapping to Molecular Gas and Star Formation in the Epoch of Galaxy Assembly. *Astrophys. J.* **817**, 169. arXiv: 1503.08833 [astro-ph.CO] (2016).
153. Gong, Y. *et al.* Intensity Mapping of H I, H I, $[\rm{O}]\backslash, [\rm{II}]\backslash, and[\rm{O}]\backslash, [\rm{III}]\backslash Lines at z \leq 5$. *The Astrophysical Journal* **835**, 273. <https://doi.org/10.3847/1538-4357/20170835/2/273> (Feb. 2017).
154. Sobral, D. *et al.* CF-HIZELS, an ~ 10 deg² emission-line survey with spectroscopic follow-up: H α , [O III] + H β and [O II] luminosity functions at $z = 0.8$, 1.4 and 2.2. *Mon. Not. Roy. Astron. Soc.* **451**, 2303–2323. arXiv: 1502.06602 [astro-ph.GA] (2015).

-
155. Tinker, J. L. *et al.* Toward a halo mass function for precision cosmology: The Limits of universality. *Astrophys. J.* **688**, 709–728. arXiv: 0803.2706 [astro-ph] (2008).
156. Tinker, J. L. *et al.* The Large Scale Bias of Dark Matter Halos: Numerical Calibration and Model Tests. *Astrophys. J.* **724**, 878–886. arXiv: 1001.3162 [astro-ph.CO] (2010).
157. Hlozek, R., Grin, D., Marsh, D. J. E. & Ferreira, P. G. A search for ultralight axions using precision cosmological data. *Phys. Rev. D* **91**, 103512. arXiv: 1410.2896 [astro-ph.CO] (2015).
158. Sabti, N., Muñoz, J. B. & Blas, D. First Constraints on Small-Scale Non-Gaussianity from UV Galaxy Luminosity Functions. *JCAP* **01**, 010. arXiv: 2009.01245 [astro-ph.CO] (2021).
159. LoVerde, M., Miller, A., Shandera, S. & Verde, L. Effects of Scale-Dependent Non-Gaussianity on Cosmological Structures. *JCAP* **04**, 014. arXiv: 0711.4126 [astro-ph] (2008).
160. Hlozek, R., Marsh, D. J. E. & Grin, D. Using the Full Power of the Cosmic Microwave Background to Probe Axion Dark Matter. *Mon. Not. Roy. Astron. Soc.* **476**, 3063–3085. arXiv: 1708.05681 [astro-ph.CO] (2018).
161. Laguë, A. *et al.* Constraining ultralight axions with galaxy surveys. *JCAP* **01**, 049. arXiv: 2104.07802 [astro-ph.CO] (2022).
162. Rogers, K. K. *et al.* Ultra-light axions and the S_8 tension: joint constraints from the cosmic microwave background and galaxy clustering. arXiv: 2301.08361 [astro-ph.CO] (Jan. 2023).
163. Tishue, A. J. & Caldwell, R. R. Dark Energy with a Triplet of Classical U(1) Fields. arXiv: 2208.11129 [astro-ph.CO] (Aug. 2022).

- 164. Alexander, S. & Yunes, N. Chern-Simons Modified General Relativity. *Phys. Rept.* **480**, 1–55. arXiv: 0907.2562 [hep-th] (2009).
- 165. Bennett, C. L. *et al.* Nine-Year Wilkinson Microwave Anisotropy Probe (WMAP) Observations: Final Maps and Results. *Astrophys. J. Suppl.* **208**, 20. arXiv: 1212.5225 [astro-ph.CO] (2013).
- 166. Aiola, S. *et al.* The Atacama Cosmology Telescope: DR4 Maps and Cosmological Parameters. *JCAP* **12**, 047. arXiv: 2007.07288 [astro-ph.CO] (2020).